

AD-784 805

INVESTIGATIONS OF TECTONIC STRESS

Charles B. Archambeau, et al

**Cooperative Institute for Research
in Environmental Science**

Prepared for:

**Advanced Research Projects Agency
Air Force Cambridge Research Laboratories
Colorado University
National Oceanic and Atmospheric
Administration**

30 April 1974

DISTRIBUTED BY:



**National Technical Information Service
U. S. DEPARTMENT OF COMMERCE
5285 Port Royal Road, Springfield Va. 22151**

Form Approved
Budget Bureau No. 22-R0293

AD 784805
ARPA Order 1795
Program Code 4F1000
Name of Contractor: University of Colorado
Effective Date of Contract: 29 October 1973
Contract Expiration Date: 28 October 1974
Amount of Contract: \$49,362
Contract Number: F19628-74-0087
Principal Investigators: Charles B. Archambeau
(303) 492-8028

Carl Kisslinger
(303) 492-7943

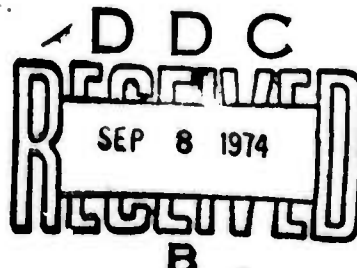
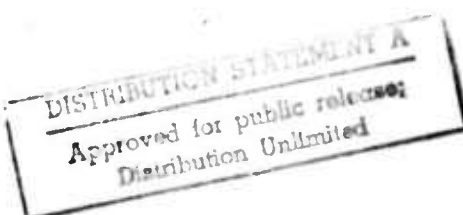
Project Monitor: Dr. Ker C. Thomson (LWW)

AFCRL
(617) 861-3665

Title of Work: Investigations of Tectonic Stress

Semi Annual Technical Report
1 November 1973 - 30 April 1974

Sponsored by
Advanced Research Projects Agency
ARPA Order No. 1795
Monitored by
Air Force Cambridge Research Laboratories



Reproduced by
NATIONAL TECHNICAL
INFORMATION SERVICE
U S Department of Commerce
Springfield VA 22151

TABLE OF CONTENTS

	<u>Page</u>
Abstract	iv
I. Introduction	1
II. Radiation Field Properties of Earthquakes	7
(a) Source description and basic spectral characteristics	8
(b) Time domain signal properties	53
(c) m_b - M_s predictions and observations	70
III. Conclusions	93
IV. Acknowledgements	95
Appendix 1	96
References	98

(a)

Index of Figures

- Fig. (1)** Effects of R_s and v_R on the global shape of the displacement amplitude spectrum. Unilateral growth. P-wave spectra. Page (15a)
- Fig. (2)** Same as Figure 1, SV-wave spectra. Page (17a)
- Fig. (3)** Same as Figure 2, SH-wave spectra. Page (17b)
- Fig. (4)** Effect of R_s on the long period displacement amplitude spectrum. Case of equilateral growth. Page (18a)
- Fig. (5)** Effect of rupture velocity on the displacement spectrum. Case of a stationary rupture with equilateral growth. Page (22a)
- Fig. (6)** Scaling of the displacement spectra with rupture length. Page (24a)
- Fig. (7)** Dependence of the near-field on hypocentral distance. Page (27a)
- Fig. (8)** Azimuthal dependence of displacement spectra. Page (29a)
- Fig. (9)** Plot of S spectral amplitude at 20 seconds versus P spectral amplitude at 2 second period. Page (32a)
- Fig. (10)** P-wave radiation patterns at four periods, and for two rupture velocities. Page (39a)
- Fig. (11)** Same as Figure 10, SV-wave. Page (39b)
- Fig. (12)** Same as Figure 11, SH-wave. Page (39c)
- Fig. (13)** Far-field phase spectra corrected back to equivalent point source. Effects of rupture velocity. Page (42a)
- Fig. (14)** Comparison of spherical rupture model with results from a two-dimensional numerical finite difference code. Page (45a)
- Fig. (15)** Comparison of observed spectrum from the Harris Ranch earthquake of 27 October 1969 with the theoretical spectrum from the propagating spherical rupture model Page (50a)

Fig. (16) Instrument response of the LRSM short period seismograph.	Page (53a)
Fig. (17) Instrument response of the LRSM long period seismograph.	Page (53b)
Fig. (18) P and S wave velocity versus depth for three models of the crust and upper mantle.	Page (54a)
Fig. (19) CIT 109 compressional wave velocity versus depth profile for the upper mantle, Basin and Range Province (layered version).	Page (55a)
Fig. (20) Depth profiles of the dissipation function Q_p .	Page (55b)
Fig. (21) Travel time versus distance curve for the CIT 109P structure.	Page (56a)
Fig. (22) Transfer function versus distance for earth model CIT 109P/.75Q (for an event at a depth of 700 meters).	Page (58a)
Fig. (23) Synthesis of a compressional wave seismogram for an earthquake of fault length $L = 2.5$ km.	Page (60a)
Fig. (24) Theoretical earthquake ($L = 2.5$ km.) wave train, showing a distinct and large sP phase and effects of later arriving mantle phases.	Page (63a)
Fig. (25) Theoretical earthquake ($L = 10$ km.) compressional wave train with same event parameters as in Figure 24.	Page (64a)
Fig. (26) Theoretical earthquake ($L = 20$ km.) compressional wave train with same event parameters as in Figure 24 and 25.	Page (65a)
Fig. (27) Theoretical P-wave signals from vertical "dip slip" earthquakes of various fault lengths.	Page (66a)
Fig. (28) Theoretical Rayleigh wave signals. The events are the same as those of Figure 27 and at the same distance and azimuth.	Page (67a)
Fig. (29) Theoretical Love wave signals. The events and distance and azimuth variables are the same as those of Figures 27 and 28.	Page (67b)

- Fig. (30) Rayleigh surface wave magnitude (M_s^R) as a function of body wave (m_b) for high stress drop, "dip slip" earthquakes. Page (74a)
- Fig. (31) Rayleigh surface wave magnitude as a function of body wave magnitude for intermediate level stress drop "dip slip" earthquakes. Page (82a)
- Fig. (32) Rayleigh surface wave magnitude as a function of body wave magnitude for low stress drop "dip slip" earthquakes. Page (83a)

ABSTRACT

The estimation of the non-hydrostatic stress field of the earth can be achieved through the use of existing m_b - M_s data for earthquakes. In this report the basis for this approach is discussed in terms of prediction of m_b and M_s from theoretical relaxation source models for earthquakes inbedded in contemporary earth models. Comparisons of these predictions with observed data indicates that if the observed m_b - M_s data is grouped with respect to source type and spatial tectonic zone, that basic source parameters and tectonic characteristics of the zone, particularly stress field characteristics, can be obtained. In addition, a basis of understanding of m_b - M_s variations for earthquakes is established and this then provides a basis for predicting and understanding m_b - M_s type discriminants for explosions and earthquakes.

I. Introduction

In order to obtain stress estimates within regions where we know that the tectonic stress levels are high, we are essentially forced to use a seismic method. The most obvious approach is to make direct use of the seismic radiation from earthquakes in order to obtain stress estimates, since such information is encoded in the radiation field and clearly these energy sources are a consequence of the tectonic stress and delineate the zones within the earth where the stress is probably highest.

The problem with this approach is that it is complicated. It involves the construction of an adequate general theory and model of the source and, in addition, requires knowledge of the structure of the earth and the ability to calculate many, if not most, of the details of the wave propagation in this medium in order to predict and fit radiation fields. Further it involves an inversion procedure wherein we wish to deduce source related parameters, including prestress, from a rather complicated observed signal.

In spite of these complications however, this approach appears to be within our capabilities and it is clear that we can obtain reasonably confident estimates of stress drops for earthquakes as well as estimates of other parameters of considerable interest. Further, under the reasonable assumption that there will be a few earthquakes among those occurring in a tectonic region of small dimension for which the

stress drop is total (the "end members" of the population of events within the restricted region), then we can use event population distributions to determine the ambient stress, by fitting the extreme events of the group.

In addition to the use of earthquakes, we can use explosions (which are to some degree controlled sources) to estimate stress levels. This entails, in part, fitting the anomalous shear wave radiation from explosions, wherein we use the concept that the explosion produced shatter zone results in stress relaxation and associated tectonically derived energy radiation.

Naturally the most uncertain aspect of using this purely seismic approach, involving theoretical modeling and "inversion" is contained in the theory and model of the earthquake or explosion source. In particular, the theory and specific model derived from the general theory must accurately reflect the important physics involved in the phenomenon, in terms of "source parameters", as well as geometric and temporal parameters giving the orientation, position and initiation of the event. In fact, viewed in any detail, there is a bewildering array of parameters and variables affecting the observed radiated seismic field from both explosions and earthquakes. To mention only the most important ones, we note that for explosions, the equation of state of the solid material at very high pressures determines, in part, the nature of the shock wave and how it decays to an elastic wave, but in addition,

the yield strength, the plastic yield level, the porosity and ratio of void porosity to fluid filled porosity, the equation of state of the fluid in the pores, the initial jointing and fracturing within the rock mass, dilatant behavior of the rock prior to yielding, the latent heats of the composite material and the initial prestress that may be existent, are all important in the determination of the elastic waves eventually emerging from the source region. In addition, of course, the energy yield of the explosion and the structure of the earth itself, expressed in terms of both the elastic and anelastic properties of the material, are directly relevant to the determination of the character of the seismic waves observed both locally to the source and teleseismically. For earthquakes, the emphasis of importance shifts somewhat to parameters and variables related to the yield strength and plastic yield behavior of rocks, which may be either compact or of a consistency to be expected in a pre-existing fault zone, subjected to both short and long term stresses. Further, the porosity and water content of the rock both within the failure zone itself and outside this zone, dilatant behavior properties such as the stress levels required to initiate dilatancy prior to failure, the magnitude, orientation and spatial variation of the pre-existing stress field, the properties of the material after failure as well as before and the yield properties of rocks as functions of strain rate and the usual thermodynamic variables (pressure and temperature) are all important parameters and variables. These

variables and the processes with which they are associated, determine the initiation of failure in a stressed region and the nature of the growth (i.e., rate, geometry, energy dissipation) of the failure zone. The changes in physical properties of the material undergoing failure and the geometry and rates of growth of the failure zone together, for a given initial stress within the medium, determine the seismic radiation from the source origin. The radiation of seismic energy actually corresponds to the release of energy from the medium surrounding the failure zone due, roughly speaking, to the reduction in strength of the failed material and an attendant relaxation of the overall stress in the essentially elastic medium around the failure zone. Thus we are concerned, in the case of an earthquake, with a volume source wherein not only are the properties of the material in the failure zone itself important, but also the properties of the medium in an extended region around the failure zone and especially the stress levels in that region. The energy radiated away as seismic waves from the source region does, of course, interact strongly with the medium and so a rather good knowledge of the structure of the earth is also necessary in order to understand the observed field and to predict it.

Clearly then, if we hope to understand the radiation fields from these kinds of seismic events in sufficient detail to enable us to determine source properties with reasonable confidence and particularly to obtain meaningful stress field estimates, we must systematically

examine the predicted range of earthquake and explosion seismic fields for a wide range of source parameters and compare the theoretical results to observations. To some degree this systematic study has been initiated in a series of separate studies (e.g., Cherry et al., 1972, 1974; Archambeau, 1972; Archambeau and Minster, 1974; Minster and Archambeau, 1974; and Minster, 1973). In the present report we will summarize those aspects of the earlier studies that provide a basis for stress estimates using earthquake radiation fields. Essentially this will involve a descriptive summary of the theoretical model for an earthquake and the results of parameter studies indicating the nature of the variation of the radiation field under parameter variations.

On the basis of these early results and with due consideration of the accessible world-wide seismic data, we have focused our attention on magnitude predictions (m_b and M_s), as especially important observation parameters to be investigated. This stems from the fact that a large collection of this data exists, which is more comprehensive than any other observational data set, and further from the fact that it has significance for earthquake-explosion discrimination. Therefore it was felt that in view of the extent of the data set available, measured from events of every type and from every location, it would be most fruitful to first consider whether it would be possible to obtain stress estimates using this data alone.

We have found, after developing the capability of synthesizing theoretical signals in the time domain and measuring magnitudes as functions of parameter changes from the time series generated, that observed m_b and M_s data can be understood (including the scatter in the observed data) and that source parameters can be obtained from this collection of data. In particular, we find that the tectonic stress prevailing in a particular zone can be deduced from this data.

In this report we discuss the earthquake source description employed, the spectral and time domain characteristics of the signals from such a source and the m_b versus M_s predictions which follow. Comparisons to observed $m_b - M_s$ data are discussed in the context of these predictions and we then summarize this comparative study in terms of the implications for a world-wide application of the approach to stress estimation. On the basis of the results of this work it appears that this approach provides a systematic means of mapping the earth's non-hydrostatic stress field with currently available data. This kind of study will then be the focus of our attention in the remainder of the contract period.

We observe, in addition, that the $m_b - M_s$ data for earthquakes and explosions provides a basis for the discrimination of these two kinds of events, and in view of the success of the theoretical predictions, we conclude that we have established a theoretical basis of understanding of this discrimination criteria.

II. Radiation-Field Properties of Earthquakes

In this section, we will give a brief description of an earthquake in terms of the basic physical concepts which are used in the formal mathematical modeling of the phenomenon and in the course of this description, introduce the parameters and variables that are required for the theoretical description of the physical processes involved. Then the essential features of the radiation field from this energy source will be illustrated in terms of the amplitude and phase spectrum of the source field, as functions of the variables and physical parameters required. Since the direct observations, and most measurements, are of the teleseismic displacements of the earth's surface expressed as functions of time, we generate synthetic displacement field seismograms from earthquakes at teleseismic distances so that we can make direct comparisons to observations. The principal observations of interest here are event magnitudes, and by measuring these from the theoretical seismograms in exactly the manner prescribed for field observations, we can make a direct comparison to observed m_b - M_s data for earthquakes. Since m_b - M_s data are discriminatory between earthquakes and explosions, at least for a considerable range of magnitude, we consider the theoretical explanation of the observed m_b - M_s data in some detail. We also are therefore able to predict m_b and M_s values for earthquakes for which we do not have a large observed data set. Furthermore, we are able to correlate m_b and M_s fluctuations

with particular parameter changes and so understand and delineate a complete earthquake population in terms of the m_b and M_s parameter space. The $m_b - M_s$ data can be used to determine event parameters by fitting observations, and in particular to obtain stress estimates.

(a) Source description and basic spectral characteristics

In simplest terms, an earthquake is (literally) the vibrational response of the earth to sudden failure of the medium within some small volume. More precisely, however, the medium is stressed and failure results in a wide-spread relaxation or reduction of the stress around the failure volume due to the sudden change in the physical properties of the failed material, so that energy is released from a volume surrounding the failure zone and the reduction of the stored strain energy is accomplished primarily by radiation of this energy away from the region of the failure. The physical process is described mathematically as an initial value problem. It has a simple one dimensional analogy in a stretched spring problem, in this case, release of the spring is analogous to initiation of failure in a strained medium and the relaxation of the spring is accompanied by its vibration, the nature of this vibration depending on the physical properties of the spring and its length. Eventually, as energy propagates down the spring, the spring reaches its new equilibrium state and motion ceases. Similarly the relaxation of the material around a failure zone in the earth is a consequence of the medium adjusting to a new equilibrium state, one defined now with the region containing the failure zone, and the medium adjusts dynamically to this new defined state by transferring energy from point

to point, eventually reaching a final equilibrium state, at which time all motion has ceased. The theoretical models of energy release that explicitly employ these concepts are called relaxation models.

Clearly the origin of the energy of an earthquake is the stored strain energy in the medium surrounding the failure zone and earthquakes are relaxation sources. When the material fails, where we could think of failure occurring in order to reduce the strain energy, energy is released from a large volume around the failure zone. The amount of energy released and the manner of its released would depend on the physical properties of the medium around and within the failure zone, on the rate at which the failure zone grows with time, its ultimate dimensions and shape and most importantly, on the magnitude and spatial variation of the strain energy stored in the entire medium. It is particularly important to remember that an earthquake is a volume source, with the origin of the energy release being a large volume around the failure zone. By contrast, this is not the case for an explosion.

The mathematical formulation of an earthquake as an initial value problem necessarily results in a description of this source as a relaxation volume source with a dependence on a number of physical parameters related to the processes of failure and stress relaxation. In particular, in order to describe the process of failure growth in time, we could introduce a failure condition within the context of the theoretical description and compute the failure surface as a function of time. However, knowledge of the failure conditions in

the earth is sketchy at best, and there are large uncertainties in the appropriate values for parameters and variables known to be important. This problem can be essentially circumvented, insofar as the theoretical description of the radiation field is concerned, by introducing a single parameter; the rupture velocity, v_R , which is defined as the rate of rupture growth. We will treat this parameter as being unknown, but with a range of expected value from zero up to the shear velocity of medium, varying in this range for earthquakes at various points in the earth, and with an absolute upper limit of the compressional velocity of the medium. The motivation in choosing this range of value for v_R is the experimental results, which indicate that rupture rates are less than the shear velocity, and considerations of causality, which require, for a spontaneous process such as the one described for an earthquake, that effects (failure in the present case) that are dependent on the propagation of a wave field for their initiation, cannot occur at a given point before the wave field has reached the point. In effect then, the failure surface cannot propagate faster than the highest wave velocity within the medium, in this case the local compressional wave velocity.

Consistent with the intuitive recognition that an earthquake is a volume source, the mathematical formulation contains a dependence on the effective elastic properties of the material inside the failure zone and outside the zone as well. This arises from the application of boundary conditions at the failure surface. In the model adopted for computations in this report, we take the process of failure of

the material to result in the reduction of the effective elastic rigidity of the failed material to essentially zero, for a short time, followed by a recovery to a value close to its original value. This is effected by allowing a spherical zone in which the rigidity vanishes to grow and translate through the stressed medium in such a way as to sweep out an ellipsoidal region in which the rigidity drops to zero and then recovers its original values after passage of the sphere. This particular model can be called a propagating spherical model and is meant to simulate a rupture followed by healing of the material. We also, in some calculations, have eliminated the healing, or rigidity recovery, by using a spherical geometry such that one edge of the growing spherical failure zone is fixed with the sphere allowed to grow and continuously envelop an ever increasing volume in which the rigidity is zero. This is termed a tangentially expanding spherical rupture model.

While we do not regard these particular models to represent very precise geometrical simulations of the failure volume, which undoubtedly, is a rather thin ellipsoidal region for most earthquake failures, we do not believe that the thickness of the failure zone is critical in the prediction of the radiated field so long as it is relatively small compared to the length of the failure zone. In the earth, this is almost certainly the case and in the propagating spherical model, we have always taken the dimensions of the ellipsoidal failure region (having circular cross section) to be such that the length is much larger than the cross-sectional radius. In order to check that the radiation field predicted is insensitive to the failure

zone thickness, if small, we compare predictions of the propagating spherical model to a two dimensional numerical model, in which the failure zone is essentially a plane (zero thickness), later in this report, and show that the results are nearly the same in all essentials when the two dimensional character of the numerical model is taken into account.

Thus, in the mathematical description of the radiation field from an earthquake, there is a dependence of the field which is clearly related to the failure process itself, in particular, the detailed nature of the radiation depends upon the rate of failure zone growth, the effective elastic properties of the material within this zone and the time dependent geometry of the spreading failure zone. By reason of our choice of a particular model, we find that this dependence manifests itself in a specific functional dependence on rupture velocity and the overall length of the failure zone. Further the field depends directly on the prestress field in a way that is a consequence of the fact that the effective shear modulus is required to vanish in the moving failure zone. Specifically, the magnitude of the effective elastic properties of the material undergoing failure to a large extent determines the magnitude of the stress relaxation in the surrounding medium. In particular vanishing of the shear tractions in the failure zone due to the zero rigidity condition results in a relaxation of stress in the surrounding elastic medium of a magnitude such that the shear tractions in the elastic medium also approach zero as the boundary is approached from the outside. However, in addition, the

initial stress field may vary spatially, so that the relaxation, when relieved spatially, is quite complex, not only because the equilibrium stress field toward which the stress is relaxing is a complex function of the rupture geometry, but also because the initial field may itself have been non-uniform, reflecting inhomogeneities of the medium and complex boundary conditions. Thus the energy release from the source volume will be non-uniform spatially, where, in fact, at some points the energy density will be higher after failure than before, but in total there will be net decrease in stored strain energy. This non-uniformity is present even if the prestress field is uniform. Further if the initial stress is concentrated near the failure zone (hence the reason for the localized failure in the first place), then there will be non-uniformity of energy release due to this initial stress concentration, as well. In particular, less net energy is released from outside the concentrated stress zone than would be the case if the stress were uniform everywhere at the level of concentration.

In the model adopted for the computations of this report, we have taken the initial stress field to be uniform for computational purposes, but have restricted the contributions to the radiated field to be from within a spherical zone of radius R_s around the initial point of failure. The objective here is, in effect, to limit the prestress field spatially. This is based on the view that the prestress conditions in the earth require a finite zone for the prestress, if for no other reason than that the earth itself is finite, but even more realistically, because tectonic stresses are clearly concentrated within particular regions in view of the distribution of earthquakes and tectonic activity.

Thus, while the prestress in the earth is probably non-zero nearly everywhere, it is equally probable that there are zones of relatively high tectonic prestress which are constrained to relatively small regions, compared to the entire earth. Thus, if we assume a prestress, it should reflect this condition. In taking a model with a uniform prestress everywhere (in fact to infinity), we can approximate the condition of relatively high initial stress near the failure zone and very low stress far from the rupture by truncating the contributions to the radiation field at some distance, which is the characteristic dimension of the stress concentration, beyond which we allow no contribution. This restricts the energy release to a zone of radius R_s around the failure. We will treat the distance R_s as an unknown parameter, but bounded below by the maximum dimension of the failure zone and above by a large number of the order of the earth's radius.

This description of the theory and the source model used for earthquakes is designed to provide an intuitive grasp of the physics of this energy source, an idea of the nature of the approximations used in the particular computational model adopted and the definition of the parameter set required to effect a mathematical description.

In summary, the important parameters are: (1) V_R = the rupture velocity, taken to be constant; (2) L = the overall rupture zone length; (3) $\sigma_{ij}^{(o)}$ = the initial homogeneous prestress field, a constant; (4) ρ , v_p , v_s the density and the compressional and shear velocities of the local medium exterior to the failure zone, all taken to be constants.

In addition, of course, the observed field depends on the orientation of the failure surface relative to a fixed coordinate system and the position in space of the point of observation relative to this coordinate system. We shall generally use spherical coordinates (r, θ, ϕ) to describe the observer's point and express the field in terms of these variables. The orientation of the failure envelope will be variously described in terms of Euler angles or strike, dip and plunge angles.

The important features of the radiated displacement field from an earthquake can be described in terms of the Fourier spectrum of the direct field (or free field) from the source, where the source is viewed in an infinite homogeneous space so that medium boundaries and elastic property changes do not complicate the picture. We will generally consider, separately, the parts of the displacement field that propagate with the compressional velocity v_p (P-waves) and with the shear velocity v_s (S-waves). The fixed reference coordinate system will be chosen with origin at the point of initial rupture and with the z axis normal to the earth's surface. Vertical polarized S waves (SV) and horizontally polarized S waves (SH) will be defined in terms of this coordinate system.

Figure (1) illustrates the shapes of earthquake P-wave displacement spectra for various combinations of the parameters v_R and R_s . The spectra shown are the far field components of the radiation from the source, that is, that part of the field that propagates with a distance dependence of $1/r$. (The remainder of the field propagates with a distance dependence that has the form $1/r(\lambda/r)^n$, with $n \geq 1$ and n an integer; so that when $r \gg \lambda$, the wave length, then these terms are

Reproduced from
best available copy.

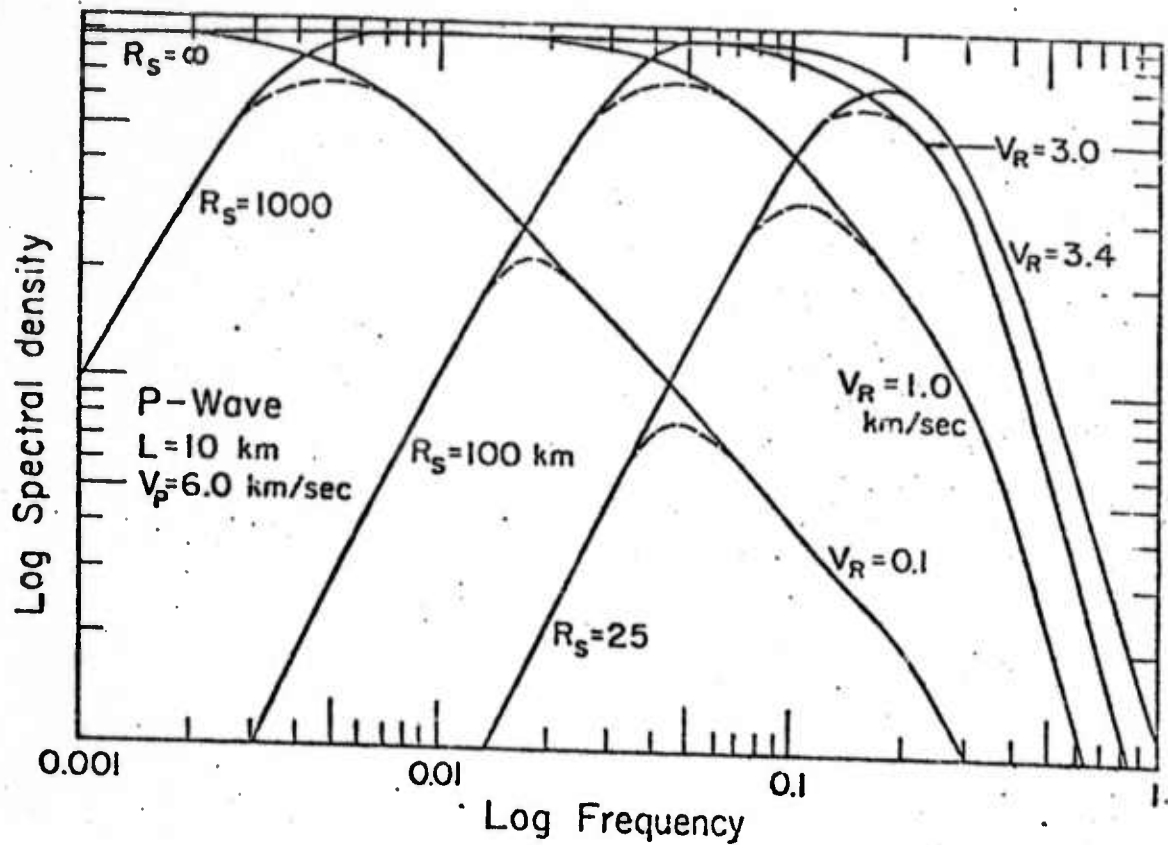


Figure 1. Effects of R_s and V_R on the global shape of the displacement amplitude spectrum. Unilateral growth. P-wave spectra.

negligible).

To determine the shape of the spectrum for a particular v_R , R_s pair from this figure, select a v_R value, say $v_R = 1.0$ km./sec., and starting at the high frequency end of the spectrum, follow the curve labeled $v_R = 1.0$, toward lower frequency. Now selecting a R_s value, say $R_s = 25$ km., cross over to the curve labeled $R_s = 25$, where the cross over is along the dotted curve connecting the two sections of the spectrum for the $v_R = 1.0$, $R_s = 25$ km. case.

The spectrum for this particular parameter pair is seen to be strongly peaked near .1 Hz. This is because the source cannot efficiently radiate energy for wavelengths, λ , greater than the characteristic dimension, R_s , of the source.

For a larger value of R_s one proceeds, analogously, along the part of the curve labeled $v_R = 1.0$ to the point where it intersects the appropriate R_s value, and then move off the $v_R = 1.0$ part of the curve onto the appropriate " R_s controlled part" of the spectral curve to define the complete spectrum. In this example, with $v_R = 1.0$ km./sec., the spectra are peaked for R_s values of 25 and 100 km., while the spectrum attains a broad flat maximum for $R_s = 1000$ km. For R_s infinite it is flat all the way down to zero frequency. For higher rupture velocity, say $v_R = 3.0$ m/sec., the high frequency decline in the amplitude

spectra is seen to begin to occur at a higher frequency than was the case for $v_R = 1.0 \text{ km/sec}$. Further the slope of the spectrum, as it decreases toward higher frequency, is steeper for larger v_R values than it is for the lower values, although at very high frequencies all slopes are approximately such that the amplitudes decay as $1/f^3$, whatever the value of v_R . For very low rupture velocities, the spectrum reaches a maximum only at very low frequency and the high frequency decay of the spectrum has broad frequency ranges over which the fall-off is roughly like $1/f$ and $1/f^2$, before attaining a $1/f^3$ slope at very high frequency.

On the other hand, the low frequency part of the source spectrum, controlled by R_s , has a decay with a dependence on frequency as f^2 (for $f < 1$), and the roll-off slope is independent of the value of R_s . However, the point where the spectral decline at low frequency begins is controlled by the R_s value, this frequency being inversely proportional to R_s .

Figures 2 and 3 show the spectral shape variations for shear waves emitted by an earthquake source. Exactly the same procedures giving the P wave spectra apply here as well. We note on comparison with the P wave spectra, two differences in the spectra for the S waves. (The SV and SH polarized shear wave spectra are in no essential way different from one another). First the spectra shown are shifted somewhat to lower frequency, as the frequencies where maximum are attained are somewhat lower than for the P waves, and the frequency where the low frequency roll-off begins is also somewhat lower. Secondly, the high frequency roll-off slope is initially steeper, for a spectrum

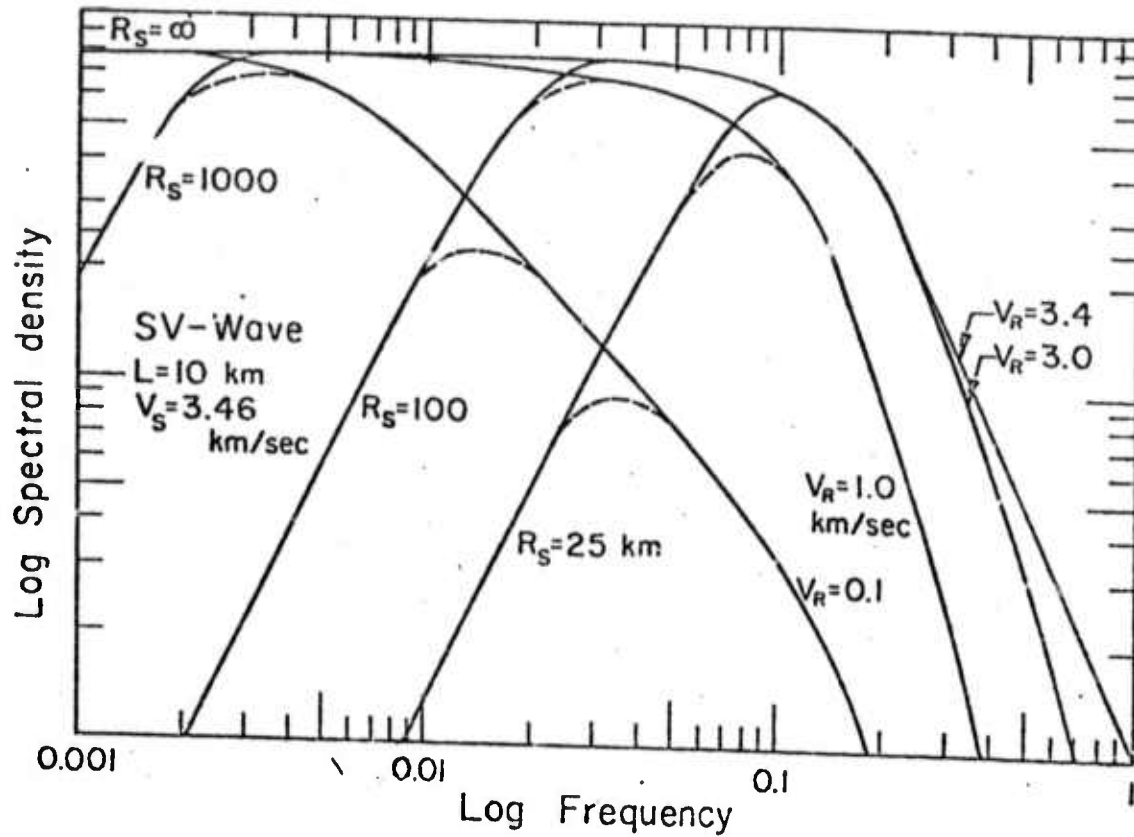


Figure 2. Same as figure 1
 SV-wave spectra.

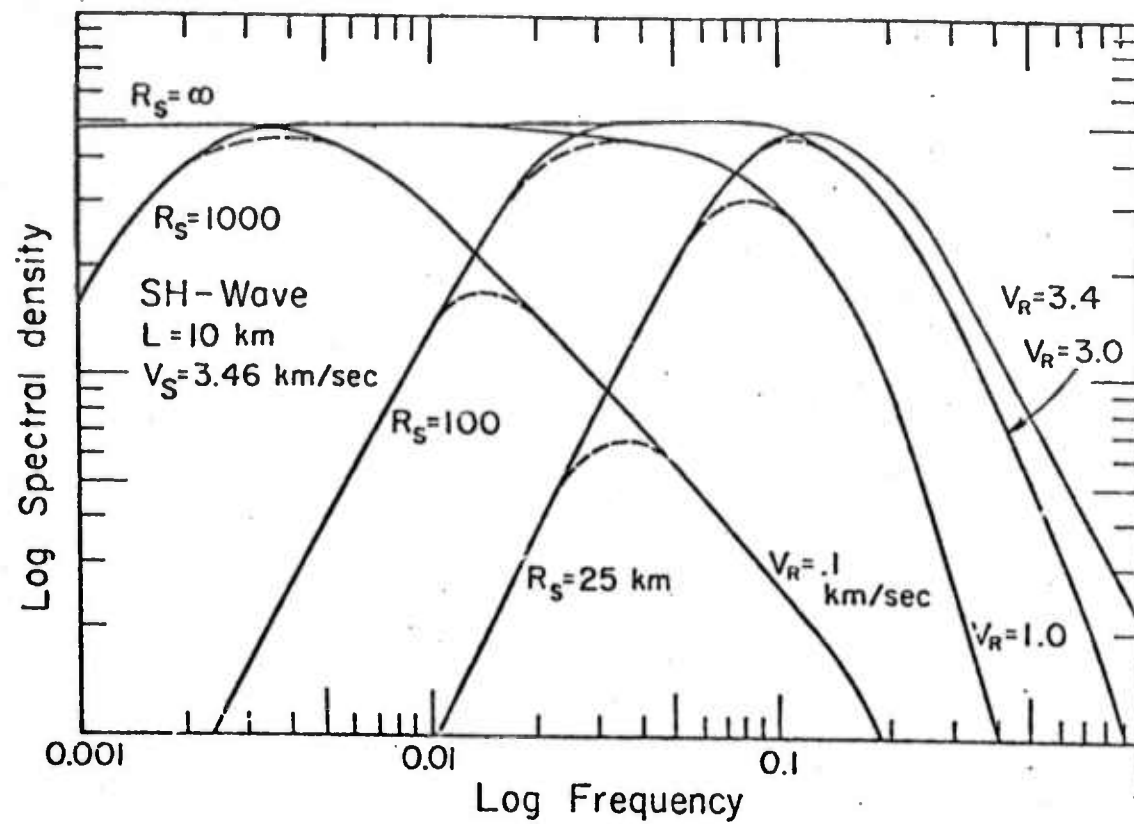


Figure 3. Same as figure 2 SH-wave spectra.

of given v_R value, than for the P-wave spectra. In particular, we note that the S-wave spectrum for $v_R = 1.0$ does not have the same characteristics as the P-wave spectrum for $v_R = 1.0$ km/sec. This indicates that "low" rupture velocity is relative to the P-wave velocity in the one case and relative to the S-wave velocity in the other. However, the S-wave spectrum does not attain the -3 slope at as low a frequency as does the P-wave spectrum. It is found, as v_R approaches v_S , that the frequency at which the S wave attains the -3 slope becomes higher and higher, so that when $v_R = v_S$ the high frequency slope of the S wave spectra is -2 for all f.

As we shall later indicate however, the spectral shape differences between P and S waves are observationally dependent on the angular position (θ, ϕ values) of the observational point with respect to the rupture orientation and one can find points at which the spectral differences just mentioned can be reversed. Hence, there is considerable variation with position, at fixed distance around the source, but on the average the situation is as described earlier.

In view of the spectral properties just illustrated, and upon both analytical and additional computational investigations, it is found that certain characteristics of the spectra for earthquakes scale in a rather simple way with respect to the source parameters illustrated. In particular, it is possible, and convenient, to define two characteristic frequencies for earthquake spectra, one at the frequency at which the spectrum begins to decrease on the high frequency side, the other where the spectrum begins to decrease at low frequencies. We will call these

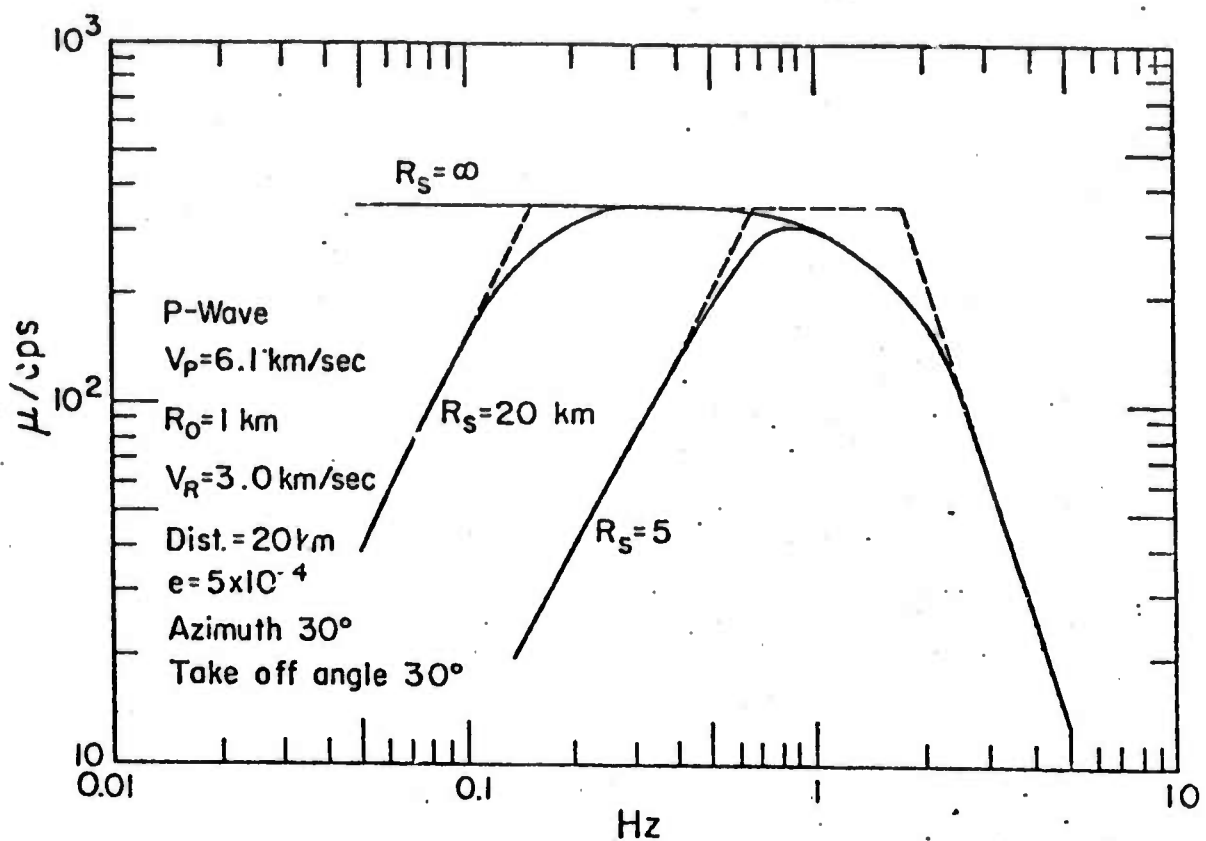


Figure 4. Effect of R_s on the long period displacement amplitude spectrum. Case of equilateral growth.

high and low "corner frequencies", f_c^H and f_c^L , of the spectrum. As we have seen, these are controlled, in part at least, by v_R and R_s respectively. In fact, we find that these frequencies can be quite precisely expressed if we define them in terms of the intersections of the high and low frequency asymptotes with the flat spectral level, defined by $R_s = \infty$. Figure 4 illustrates these intersection points for a rupture length $L = 2R_o = 2$ Km, and for the case of high rupture velocity. The dotted lines are the extrapolations of the high and low frequency asymptotes and their intersections with the $R_s = \infty$ line, defining the flat level or maximum of the spectrum, gives the two corner frequencies in question. Analytically, it is found (Minster, 1974, Minster and Archambeau, 1974) that these frequencies can be expressed in terms of the source parameters as

$$\omega_c^H \approx \frac{v_R}{L} \left[\frac{\frac{3v^2}{2} p, s}{\frac{v^2}{2} R_s} \right]^{1/3} \quad (1)$$

$$\omega_c^L \approx \frac{v_{p, s}}{R_s} \left[\frac{10}{1 - 3/5(L/R_s)^2} \right]^{1/2} \quad (2)$$

where $\omega = 2\pi f$ is the angular frequency and where $v_{p,s}$ denotes either v_p or v_s ; to be used depending on whether P or S wave spectra are involved. These formulae, although obtained by approximate analytical methods from the exact theoretical results, are quite accurate when compared to (essentially) exact numerical evaluations of the complex mathematical results representing the radiation field from the source models.

As we have seen, when R_s is small enough or when v_R is small, then these frequencies will be such that the spectrum peaks at a single frequency due to "overlapping" of the low and high frequency behavior and the flat spectral level will not be attained. (In Figure 4 this occurs for $R_s \leq 5$ km.) A reasonably accurate estimate of this peak frequency is given by the intersection of the low and high frequency spectral asymptote lines. This frequency will be called the peak frequency, f_p , and is given by

$$\begin{aligned} \omega_p &\approx \frac{v_{p,s}}{L} \left\{ \frac{10 \left(\frac{v_R}{v_{p,s}} \right)^4}{(R_s^2/L^2 - 3/5)} \right\}^{1/5} \\ &= \frac{v_R}{L} \left\{ \frac{10 \left(\frac{v_{p,s}}{v_R} \right)^4}{(R_s^2/L^2 - 3/5)} \right\}^{1/5} \end{aligned} \quad (3)$$

where $\omega_p = 2\pi f_p$. In all these results $R_s > L$, and we generally expect that R_s will be at least several times as large as L for actual earthquakes. In general then, the factor $(R_s/L)^2$ is large compared to unity in the relations (2)-(3).

Inspection of these scaling relations shows that f_c^H is independent of ' $'$ while f_c^L is independent of v_R , as was indicated in the spectra shown in Figures (1)-(3). The peak frequency, f_p , on the other hand, depends on all the parameters. These characteristic frequencies scale in a particularly simple way and provide a very useful means of estimating earthquake spectral characteristics without lengthy computation.

We can now precisely define what we mean by the high and low frequency parts of an earthquake spectrum. The high frequency spectrum is simply that part for which $f \geq f_c^H$ and the low frequency spectrum that part for which $f \leq f_c^L$. We term the frequency range $f_c^L \leq f \leq f_c^H$ the intermediate frequency range for an earthquake.

It is important to note that there is a part of both the P and S wave spectrum in the intermediate frequency range where the

spectrum is not flat and is decreasing toward high (or low) frequency with a slope of -1 or -2. For low rupture velocity in particular, the spectrum decreases over a very wide frequency range with slope -1 to -2 before reaching the high frequency asymptote slope of -3 which defines f_c^H . Thus, in this situation in particular, the usefulness of a corner frequency defining high and intermediate frequency spectral ranges is limited. Figure 5 illustrates the situation very well, showing that the P and S wave spectra for $V_R = .3 \text{ km/sec}$ have roughly a decade frequency range, from .1 to about 2 Hz, where the spectra decrease with a slope varying in the range -1 to -2, while the corner frequency f_c^H is near 1 Hz. On the other hand, for the high rupture velocity spectra, we see that the high corner frequency is near the point where the spectrum levels off and the intermediate frequency range spectrum is described accurately as being an essentially flat spectral range.

Figure 5 also illustrates some other important spectral properties. First we again note that for high rupture velocity both the P and S wave spectra approach a $1/f^3$ frequency dependence at high frequency, but that for V_R actually very close to V_S the S wave spectrum has a high frequency dependence of $1/f^2$ in this limit. The P wave spectrum would behave in the same manner if V_R were allowed to approach the P wave elastic velocity.

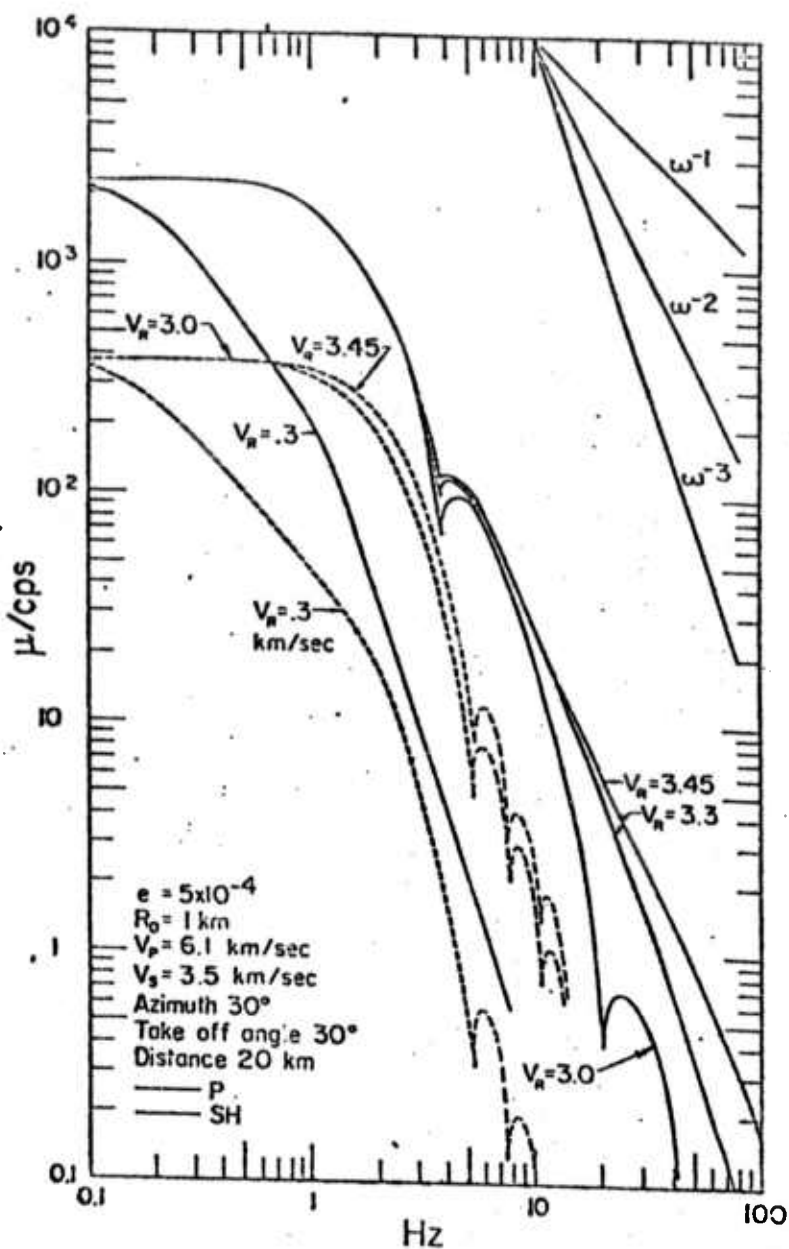


Figure 5. Effect of rupture velocity on the displacement spectrum.
Case of a stationary rupture with equilateral growth.

In addition, the high frequency spectra are shown in more detail here, without averaging, and numerous maxima and minima are shown, these being due to interference effects associated with rupture propagation. These "fluctuations" can have an important influence on measurements if observations are made in a narrow part of the frequency range which happens to lie at one of the maxima or minima. Since most detectors are very narrow band systems and since it is common practice to make measurements from narrow band filtered seismograms, these fluctuations can sometimes give rise to order of magnitude variations from the mean, if spectral amplitudes are being estimated.

Of principal importance, however, are the differences in the maximum values of the P and S spectra shown in Figure 5. We see that the S wave maximum level in the intermediate frequency range is about 5 times that of the P wave. On the average this also holds in the high frequency range. This is an important and distinctive characteristic of earthquake sources that has been well verified by observations. Analytically, we find that the relationship between the P and S wave spectral amplitudes, A_P and A_S respectively, is of the form (Minster, 1973; Minster and Archambeau, 1974):

$$A_S/A_P \propto (V_P/V_S)^3 \quad (4)$$

Thus earthquakes are much more efficient S wave radiators than they are P wave radiators; this is primarily because there are no large volume changes involved in the failure process and the change in elastic properties within the failure zone are largely changes in rigidity resulting in shear stress relaxation for the most part. However because of the Poisson effect, even if there were no volume changes at all and purely a vanishing of shear tractions on the failure surface, there would still be associated changes in compressional stresses and resulting compressional wave radiation.

Figure 6 shows the change in the P and S wave spectra for changes in the maximum dimension, or length L , of the failure zone. Here V_R is fixed and we have set $R_S = 10 L$, so R_S also scales with L , and the spectra, consequently, do not change shape. However, now, the corner frequencies f_c^L and f_c^H will both scale linearly with L . From Figure 6, as well as from analytical results, we see that the amplitude of the P and S spectra are proportional to L^3 . Thus

$$A_{P,S} \propto L^3 \quad (5)$$

The scale shown along the line AA' in the figure shows the positions of f_c^L and the spectral levels for failure lengths, L , in the range 1 to 10 km. Lines BB' and CC' are similar scales for the S waves. This simple dependence on L has been reasonably well verified

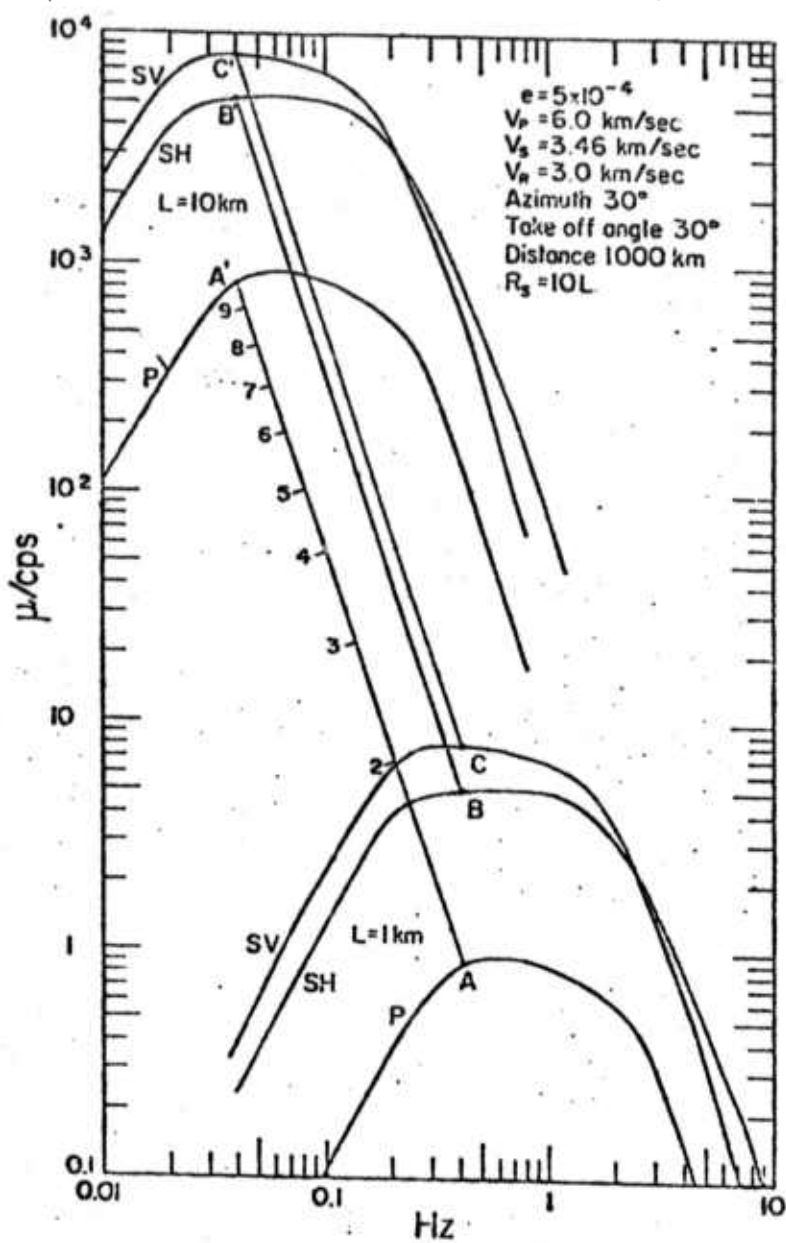


Figure 6. Scaling of the displacement spectra with rupture length.

observationally, although it is of course difficult to obtain reliable, independent estimates of L . Nevertheless, the accumulated information is in strong statistical agreement with (5), even though the individual observations making up the set are subject to considerable uncertainty.

Another rather simple dependence of the spectrum on basic physical parameters is the shift of the spectrum with changing prestress. We find that the spectrum is uniformly raised or lowered, directly as the prestress is raised or lowered. Thus the spectrum scales linearly with the prestress. Therefore with $|\sigma_{ij}^{(0)}|$ denoting the magnitude of the prestress we find

$$A_{P,S} \propto |\sigma_{ij}^{(0)}| \quad (6)$$

As is apparent, however, from the nature of the physical processes involved in an earthquake, that the absolute magnitude of the spectral levels of P and S waves from earthquakes are dependent on the difference in the residual stress sustained within the rupture after failure and the initial prestress $\sigma_{ij}^{(0)}$, and hence not only on the magnitude of the prestress but on the effective elastic constants of the material that has undergone failure. For fixed properties of the material in the failure zone then, this stress difference, or stress drop, is itself directly related to the initial stress, so that it is equivalent to say that the spectral level scales linearly with the

stress drop (or stress difference) or that it scales linearly with the initial stress, as in (6).

Further it can be shown that the stress field inside the failure zone, with constant effective material elastic constants μ' , λ' and density ρ' , is uniform, that is it is a constant (e.g., Minster, 1973). This residual field can be subtracted from all stress fields appearing in the mathematical formulation; the effect being to reduce all static stresses by a constant and to leave unchanged the dynamic stresses appearing in the problem since this residual stress is a constant and independent of time as well as the spatial variables. This procedure is equivalent to reducing the formulation to one for a failure zone with vanishing effective elastic rigidity, if the constant residual shear stress field has been subtracted, and this is the model employed in this study. However the difference is that now the effective prestress for this new zero shear strength failure zone problem is: $\sigma_{ij}^{(0)}$ minus the constant residual shear stress, rather than $\sigma_{ij}^{(0)}$ itself. But this reduced prestress is just the stress difference or "stress drop" that was previously mentioned as being the parameter upon which the absolute spectral magnitudes depend.

Therefore in (6), we should view $|\sigma_{ij}^{(0)}|$ as being the true prestress value, only, if, in fact, the rigidity does vanish within the failure zone at least for a time comparable to, or longer than, the periods of the radiation field of interest to us. However, it should be viewed as

the stress difference or stress drop, defined as $|\sigma_{ij}^{(0)} - \tau'_{ij}|$, if the effective rigidity does not vanish, where τ'_{ij} is the constant residual shear stress in the failure zone.

Figure 7 illustrates the spectral shape of the composite near and far field spectra from an earthquake. Up to this point we have only considered the far field spectra since it is essentially the only part observed telesismically, that is at distances r large compared to the wavelengths of the displacement field recorded. However, if we display the total spectrum at various distances from the source, we find that at very low frequencies (long wavelengths) the near field gives a strongly dominating contribution that behaves as $1/f$ at frequencies such that $\lambda > r$. This figure also illustrates the combined effect of R_S and the near field contribution to the overall spectral shape at various distances from the source. In effect, the frequency at which the near field begins to be important is given by $T = 1/f = r/V_p$ or $T = 1/f = r/V_s$ for P and S wave spectra respectively. If this frequency is close to f_c^L then the characteristic decrease in the spectrum for frequencies lower than f_c^L will be modified, at small distances strongly, by the near field contribution. Figure 7 illustrates this by showing two values of R_S for a total source spectrum at particular distances.

In the near field distance ranges the P and S wave fields can still be separated analytically, Figure 7, however, shows the sum of

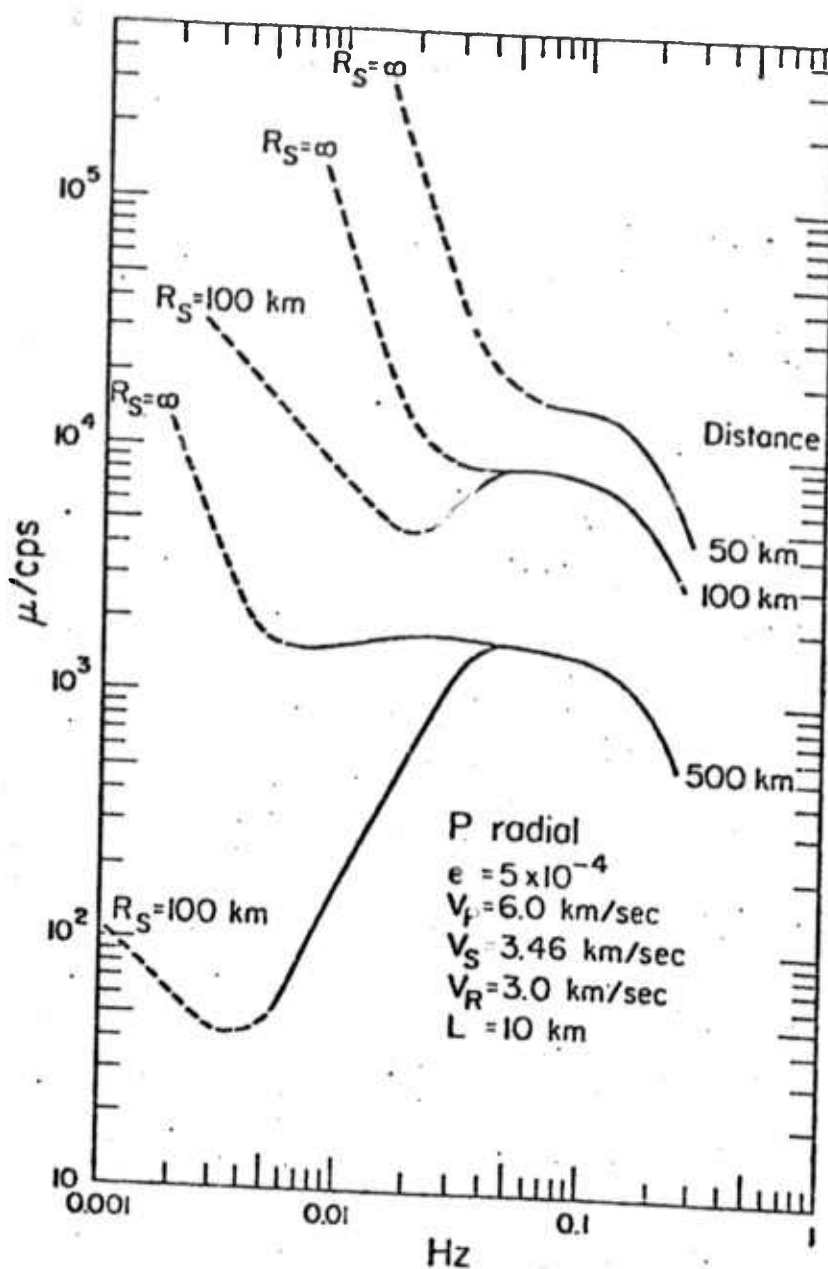


Figure 7.

Dependence of the near-field on hypocentral distance.

these fields. If we investigate the total field for the P wave from the source we find that,

$$A_P \propto \frac{1}{f^3}, \text{ for } 1/f = T > r/V_P \quad (7)$$

and similarly, for the total S wave amplitude variation with frequency in the near field,

$$A_S \propto 1/f^3, \text{ for } \frac{1}{f} = T > r/V_P \quad (8)$$

However, as Figure 7 shows and as we find analytically, the sum of the P and S wave fields in the near field range varies with frequency as

$$A_{P+S} \propto \frac{1}{f}, \text{ for } 1/f = T > r/V_P \quad (9)$$

where A_{P+S} denotes the summed P and S spectral amplitude.

It has been observed that near field spectra from earthquakes do in fact appear to show a $1/f$ frequency dependence. This, of course, is not at all surprising in view of the fact that the inverse Fourier transform of a spectrum that behaves as $1/f$ at low frequency will give a step offset in the time domain and hence yields the expected result that there is a static change in the displacement of the medium after an earthquake. It is, however, further verification of the validity of the models used in this study that they also yield this required result.

Observations of the radiation from earthquakes also indicate that the spectral shapes are dependent on azimuth relative to the direction of failure in the medium. Figure 8 shows an example of the predicted variation based on the propagating spherical model, where azimuth is the spherical angular variable ϕ measured from the direction of the failure zone propagation. The spectra show that the mean slope can change considerably resulting in very different spectral levels at particular frequencies in the high frequency range for different azimuths. This is in general agreement with the observations.

Observations, when available and reliable, are, in general, in good agreement with the theoretical spectral properties discussed. The features described and their variations have been observed, but there is uncertainty in the observations due to earth structure effects and nearly all the observations have been over a narrow band width. Further, noise and spurious data analysis effects (e.g., truncation of the time series) always contaminate the observations, making it difficult to draw solid conclusions.

In particular, the existence of the characteristic corner frequency f_c^L and associated spectral decrease at low frequencies in the far field spectra has been a subject of debate and the resolution of the question is still pending; but appears near. High quality near field observations of small (and numerous) earthquakes is currently

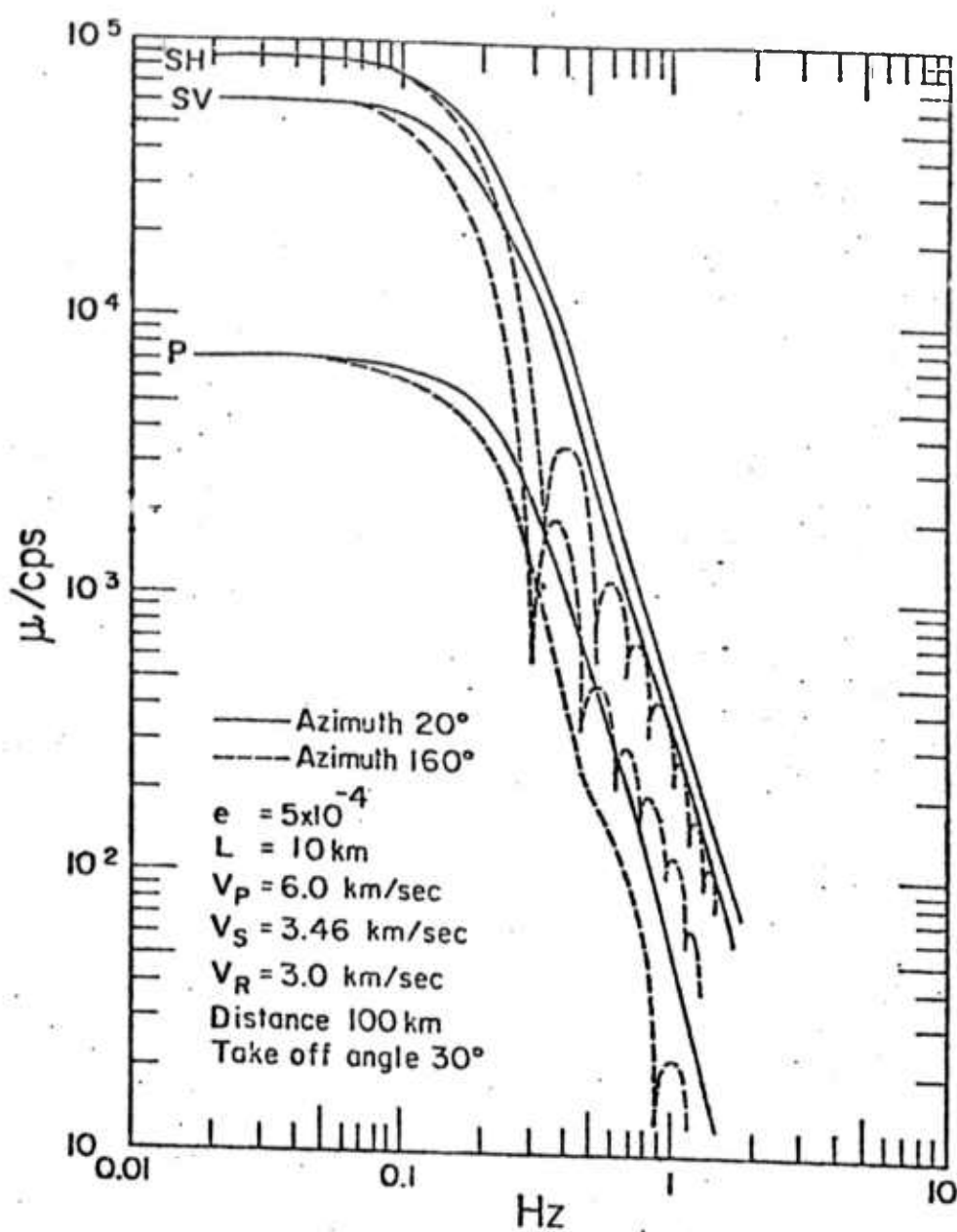


Figure 8. Azimuthal dependence of displacement spectra.

in progress and is expected to resolve the question. It happens that this is a critical question in as much as it strongly affects the expected surface wave magnitude for an event. In this study we shall therefore consider the complete range of possibilities regarding R_S ; that is by allowing R_S to range from infinity to something of the order of the failure zone maximum dimension, we will be able to cover all possible situations and models.

Two particularly important magnitude parameters for a seismic event are the body wave magnitude, m_b , measured from among one of the amplitudes of the first 2 to 3 cycles of the P wave arrival as recorded through a narrow band seismometer with center frequency near 1 cps., and the surface wave magnitude, M_S , measured from the Rayleigh surface wave horizontal (or vertical) component as recorded by a long period seismometer with a band pass centered around .05 Hz. The M_S is computed from the log of the amplitude of that part of the surface wave train that has a period of oscillation near 20 seconds (.05Hz). The m_b magnitude is usually computed from the log of the amplitude of the largest peak to peak amplitude in the first two or three cycles of motion and usually the effective period of this transient motion is close to 1 second. Thus the m_b and M_S measurements are proportional to the logarithms of event spectral values at 1 Hz and .05 Hz respectively.

Consequently in view of the spectral properties of earthquakes previously described, we can obtain a good estimate of the nature of

the $m_b - M_S$ values to be expected for earthquakes as functions of failure zone length L , prestress level, rupture velocity and stress concentration dimension R_S .

It is therefore particularly appropriate to summarize the spectral properties and their parameter dependence in terms of magnitude related spectral characteristics. This is best effected by considering the log of the spectra at .05 Hz as a function of the log of the amplitude spectra at 1 Hz and plotting the results for a series of events in this parameter space. Since we have shown that the S wave radiation from an earthquake is considerably larger than the P wave, and since the Rayleigh surface wave is excited by a combination of P and S waves through interference effects within the layered medium, with the relative efficiency of the Rayleigh type surface wave excitation by P and S waves roughly of the same order*,

*Hannon (1972) suggests that S waves are more efficient than P waves in exciting Rayleigh waves. Gilbert (1973) has demonstrated that the amplitude ratio of Rayleigh waves to P waves is dependent on the square root of the ratio of shear energy to compressional energy produced by the source. In effect then, S waves from an earthquake, being much larger than the P waves, constitute the major portion of the shear energy, and hence control the Rayleigh wave generation. A similar conclusion was reached by Douglas et al. (1971) in a study similar to Hannon's.

then we will take the log of the S wave spectral level at .05 Hz to be a measure of the surface wave magnitude M_S , since it is so much larger than the P wave.

Figure 9 shows the results obtained from computations involving a whole series of earthquakes of varying dimension L , with R_S and V_R as parameters that are varied for a given event. The locus of events in this parameter space cover a rather large region, showing that $m_b - M_S$ observations for earthquakes can show a large "scatter" which is due to the possibility of many different "kinds" of earthquakes, that is earthquakes with high and low rupture velocity and large and small R_S factors; this latter reflecting events occurring within a spatially very broad, high prestress zone or within a prestress zone of small dimension. The character of these curves can be understood in terms of the spectral shape and amplitude scaling relations previously discussed.

As an example, suppose we consider a series of events of increasing dimension L , all with small R_S equal to $R_S^{(1)}$ and high rupture velocity V_R equal to $V_R^{(3)}$. The locus of these events in the parameter space of Figure 9 begins, for small L , along the lowest curve labeled $R_S^{(1)}$, near $\log A_S = -5$, $\log A_P = -3$, and continues, as shown, to the point C along the locus of "event points" with the largest $\log A_P$ values and the smallest $\log A_S$ values. For yet larger L values for the events of this class, the curve traced by the

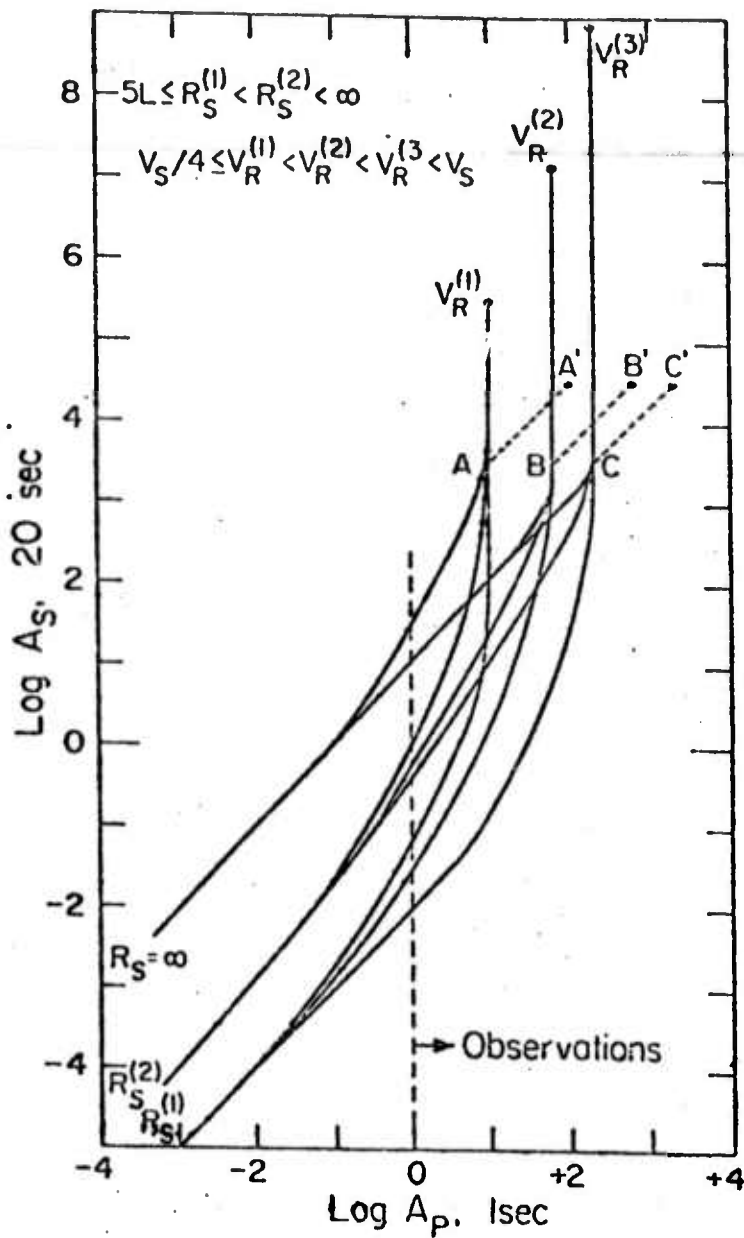


Figure 9. Plot of S spectral amplitude at 20 seconds versus P spectral amplitude at 1 second period. Simulation of m_b / M_s plots.

events in this space is vertical along the line labeled $V_R^{(3)}$ in the figure and continues up to a termination point near $\log A_S = 8.9$.

Similar loci are traced by event series with varying L values for other fixed sets of the parameters (V_R, R_S) , as indicated.

Clearly there is a continuum of such curves, bounded by limiting curves such as the one for $R_S = R_S^{(1)}$, $V_R = V_R^{(3)}$ and, at the other limit, of maximum $\log A_S$, the curve for $R_S = \infty$, and $V_R = V_R^{(1)}$.

Between such bounding curves for the earthquake population we can find earthquakes with all combinations of R_S and V_R values. In addition to the R_S and V_R parameters, the value of the prestress will affect the position of the event loci in this parameter space. The prestress level has a rather simple effect and is indicated, for example, by the shift of C to C' along the dotted line shown in the plot. That is, increase of the prestress by an order of magnitude causes a uniform shift of the whole curve such that it will pass through point C' instead of through C . Thus dragging the whole curve rigidly over to C' gives the new curve for a prestress of an order of magnitude higher. Because the amplitude scaling with prestress is linear, C' is related to C by one unit change in $\log A_P$ and in $\log A_S$. Hence the line CC' has unit slope. Of course this line may be extended in all directions so that for any change in prestress the point C moves along a line of unit slope for a distance which is simply related to the logarithm of the ratio of the new prestress to

the old prestress value (i.e., it is the square root of two times this logarithm). Precisely the same relationships hold for the points A-A' and B-B', for the other curves shown.

The shapes of the curves shown in Figure 9 are easily understood. For small events, f_c^H is above 1 cps. and for events small enough, the measurements of $\log A_p(1)$ and $\log A_s(.05)$ are made in the low frequency range of the event spectrum so that the R_s factor controls the values of both these measurements and the value of V_R is immaterial. Thus as L increases in the range of small L , for fixed R_s , both $\log A_p$ and $\log A_s$ increase by nearly the same amounts since both measurements are made along a part of the spectral curves that have the same slope -- whether that slope is 2, 1 or zero is immaterial. Thus the curve in this portion of the parameter space will have close to unit slope.

As L increases further, the measurement of $\log A_p(1)$ is made at values above f_c^L but below f_c^H , that is in the intermediate spectral frequency range, while $\log A_s(.05)$ is still made in the low frequency spectral range. Since the spectral slopes are different in these two ranges (see Figure 6, for example) where the intermediate frequency range can have a slope of zero, -1 or -2 depending on V_R , the increase of $\log A_p(1)$ may not be as large as the increase in $\log A_s(.05)$ for an increase in L . In particular, if $\log A_p(1)$ is measured in the range where the spectrum is decreasing with slope

-1 or -2 while $A_S(0.05)$ is measured below the f_c^L point, then the L^3 amplitude scaling, coupled with the linear shift in f_c^L and f_c^H with increasing L , will cause an increase in $A_S(0.05)$ by a factor of 8 in magnitude, for L increasing by a factor of 2, provided, $.05 < f_c^L$ holds for both L values. However the same change in L will increase $A_P^{(1)}$ by only a factor of between 4 to 2, depending on whether the spectral slope is -1 or -2 in the range near 1 Hz.

Thus the event curves in the magnitude space will begin to steepen. Of course where this begins to occur depends on the value of R_S , since it determines the low frequency bound of the intermediate frequency range for the spectra. Further the shape of the spectral curve in the intermediate frequency range depends on V_R , for high values of V_R the spectrum is essentially flat between f_c^L and f_c^H while for low V_R it will have a gradually increasing negative slope toward the high frequency end. An extreme case illustrating this point is the case for $R_S = \infty$ shown in Figure 9. In this case f_c^L is zero and both $A_P^{(1)}$ and $A_S(0.05)$ measurements are in the intermediate frequency range for small L . For high rupture velocity, the spectrum is nearly flat all the way to f_c^H and so both $A_P^{(1)}$ and $A_S(0.05)$ increase by the same amounts for increases in L . The event curve is linear with unit slope in the parameter space as shown in Figure 9 all the way to point C for $R_S = \infty$ and $V_R = V_R^{(3)}$, the high rupture velocity case. Near point C however the size of the events will be

such that f_c^H will be less than 1 Hz, so that $A_p^{(1)}$ will be measured in the high frequency range where the spectral slope begins to become negative, eventually reaching a -3 slope. Thus in the range, $A_p^{(1)}$ will not increase as much as $A_s(.05)$ for an increase in L and eventually when the 1 Hz amplitude measurement is made in the range where the spectral slope is -3, $A_p^{(1)}$ will cease to increase at all. This is because the slope of the scaling line (see Figure 6 again) with increasing L has a slope of -3 and further increases of L simply slides the spectra along the -3 slope asymptote, so that at a fixed frequency in this asymptotic frequency range, the spectral levels for two events with different L values do not change. In the case of a very high rupture velocity, this -3 spectral slope region is reached after a brief frequency interval and the curve in the $\log A_p - \log A_s$ space rapidly changes slope from unity to a vertical line marking the termination of the $\log A_p^{(1)}$ values. For earthquakes with lower rupture velocity values, the change from unit slope to a vertical slope in the $\log A_p - \log A_s$ plane is more gradual, reflecting the broader frequency range over which the spectrum changes from zero slope to -3 slope. Eventually however, whatever the value of the rupture velocity, a point is reached where $A_p^{(1)}$ ceases to increase with increasing L , as is shown in Figure 9.

For yet larger events, for which $A_p^{(1)}$ remains constant, the value of $A_s(.05)$ continues to increase rapidly until $f_c^H = .05$ Hz,

whereupon, for larger events, $A_S(0.05)$ increases more slowly since the spectrum is now being sampled in the range where it has negative slope. If the rupture velocity is below the shear wave velocity of the medium, then eventually the -3 slope asymptote of the S wave spectrum will be reached and $A_S(0.05)$ will also cease to increase.

This point is shown as the termination point at the high $\log A_S$ ends of the curves in Figure 9. If, however, the rupture velocity can be trans-sonic, that is $V_S \leq V_R < V_P$, then the -3 slope is at infinite frequency and the highest slope of the S wave spectra is -2, in which case $\log A_S(0.05)$ will continue to increase with increasing L .

However a -3 slope for P wave spectra will still occur at finite frequency for P wave spectra when V_R is in this range so that $\log A_P(1)$ will still have an upper bound.

If, finally $V_R \geq V_P$ (shock conditions), then neither the S nor the P wave spectra will have -3 slope at finite frequency and so both $A_P(1)$ and $A_S(0.05)$ will be unbounded in L . In this case there are no termination points in the $\log A_P(1) - \log A_S(0.05)$ (or $m_b - M_S$) plane. However, neither the trans-sonic nor super-sonic cases appear to occur in nature, although they cannot be ruled out even though the physical conditions required for their occurrence are rather extreme. In any case, statistically speaking they are ignorable in view of the probabilities for their occurrence, and we shall not consider them further.

The translation of the spectral properties of earthquakes into $m_b - M_s$ like data has a number of important uses. Obviously for discrimination purposes we will compare these results to those for explosions. Further, comparisons to observations for earthquakes gives us information regarding the stress levels, rupture velocities and event dimensions for earthquakes as functions of depth and tectonic location. Perhaps as importantly, theoretical exploration of this parameter space allows us to investigate the expected range of magnitude values for earthquakes as a function of the physical parameters characterizing these events, hence to map the population of events and hence to understand what magnitude data means and to explain its scatter in terms of classes of earthquakes and the physics of the process itself.

To compare the results of Figure 9 directly to observed data is awkward since observations are made in the time domain in the manner described earlier and there is, necessarily, uncertainty in the correlation of such measurements with frequency domain results. In addition, there are the effects of earth structure that enter into the interpretation of the teleseismic $m_b - M_s$ observations that have not been included in the results of Figure 9. Therefore we will instead reproduce these results in the $m_b - M_s$ plane later, where we will generate the time domain signals equivalent to the spectra, taking into account earth structure, and measure m_b and M_s from the time domain in exactly the manner as in observational studies. At this point we will compare the predictions to observations.

However, in spite of the uncertainty involved in interpreting observed $m_b - M_s$ data in terms of the spectral results of Figure 9, it is a fact that the shapes of the curves shown are very similar to least square fits to $m_b - M_s$ data. Further the amount of scatter in $m_b - M_s$ data is about what is expected if it is primarily due to variations in V_R , prestress and R_s values. We shall consider these points in more detail at the end of this section, in part C., where we compare the theoretical $m_b - M_s$ to observations.

Additional spectral characteristics of earthquakes that are important include the radiation patterns of these events as functions of frequency. Figures 10, 11 and 12 show the direct source field radiation at fixed frequency, as a function of azimuth ϕ . The frequency range covered is from the low frequency end of the spectrum ($f \sim f_c^L$) to the high frequency end ($f > f_c^H$), where the rupture dimension $L = 10$ km.

Since the earthquake source may be viewed as a multipole radiator, and in fact is mathematically equivalent to a point multipole source (Archambeau, 1968), we shall discuss these patterns in these terms. We should observe that explosions can similarly be described, and the difference in multipole excitation by these two different kinds of sources constitutes a means of discriminating between them observationally. Further, an ideal explosion will radiate as a monopole for P waves and generate no direct source S waves at all. If tectonic stress release occurs for an explosion, then the P wave radiation will be

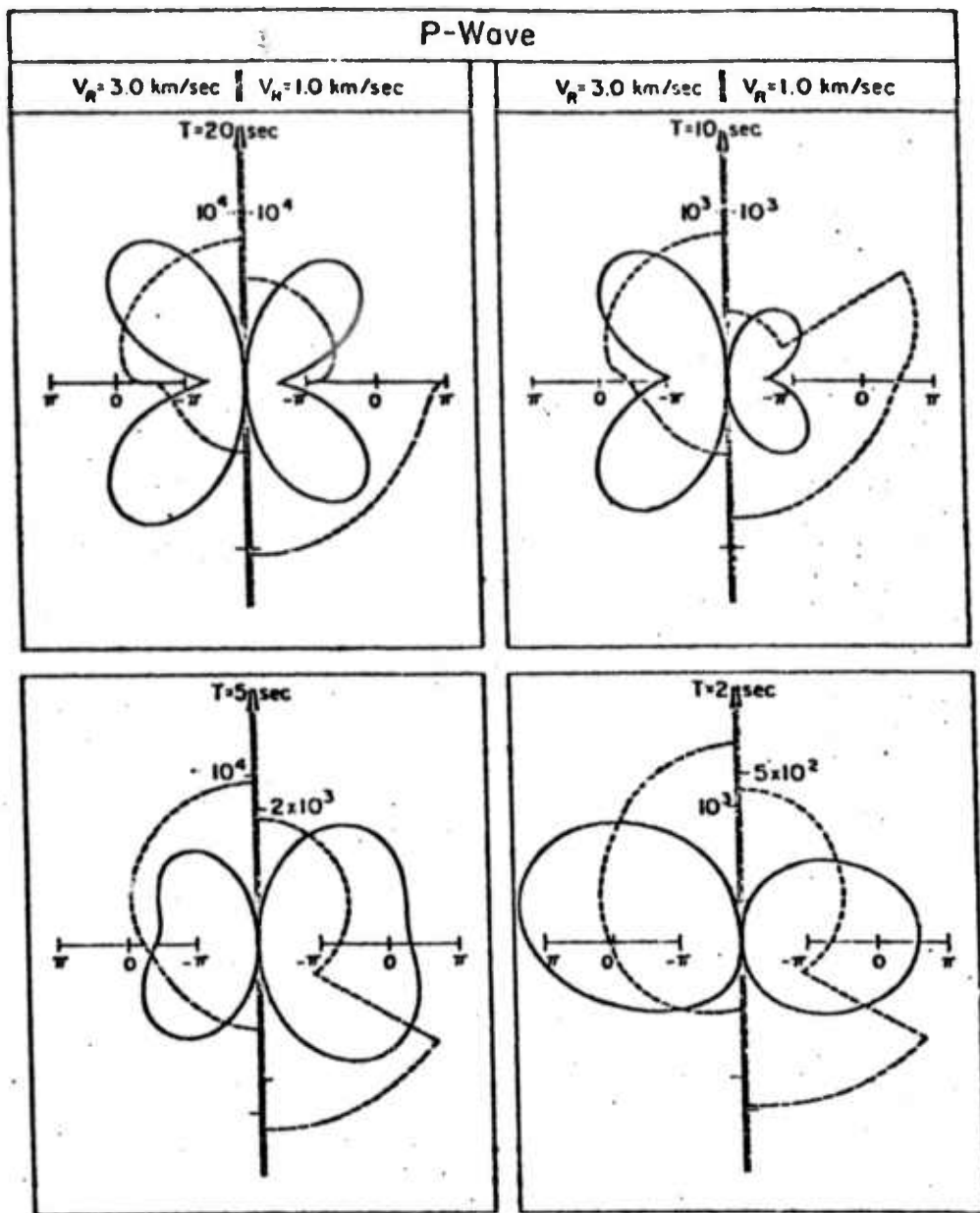


Figure 10. P-wave radiation patterns at four periods, and for two rupture velocities. Only half-patterns are shown. The solid line is the amplitude pattern; the broken line is the phase pattern.

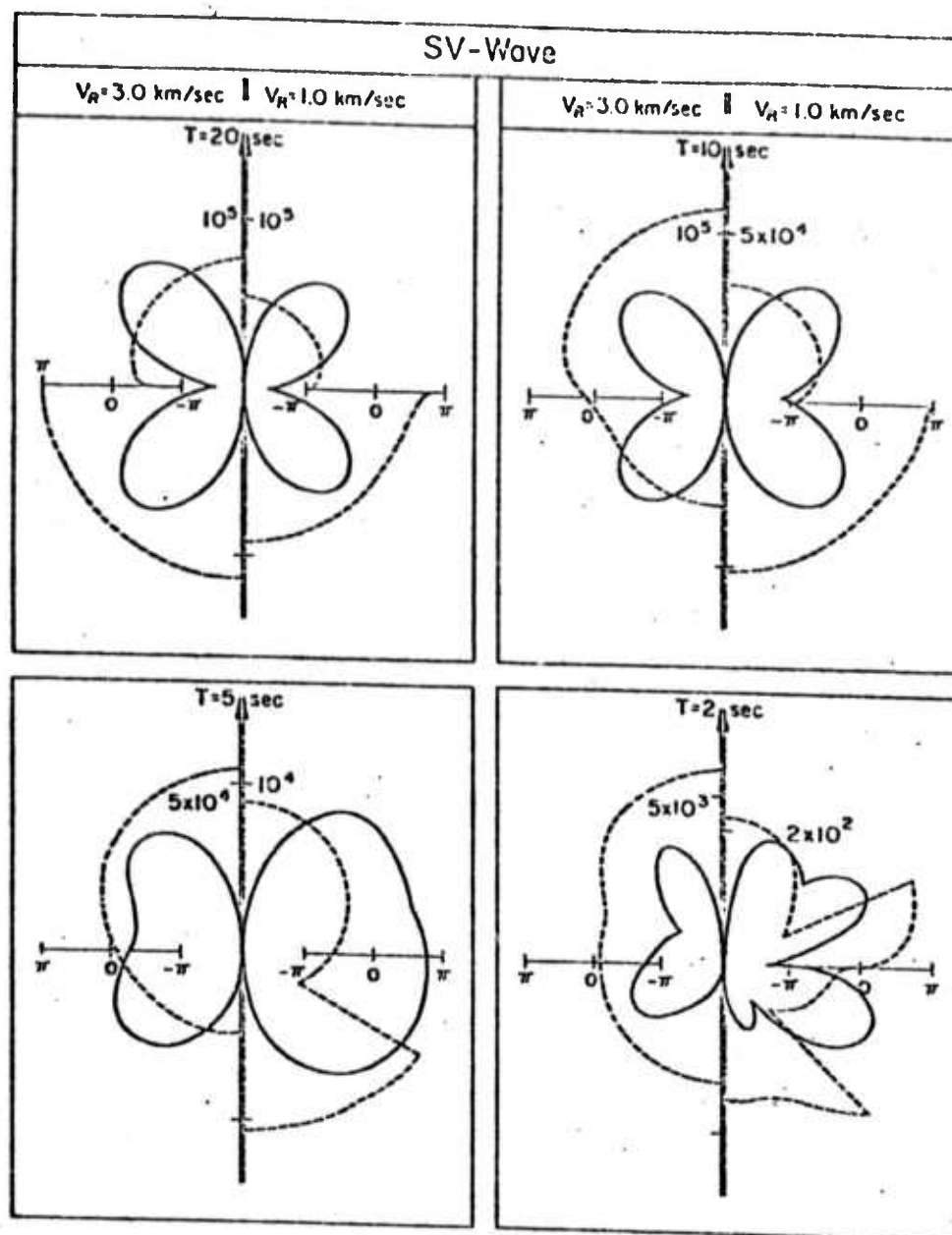


Figure 11.

Same as figure 10

SV-wave.

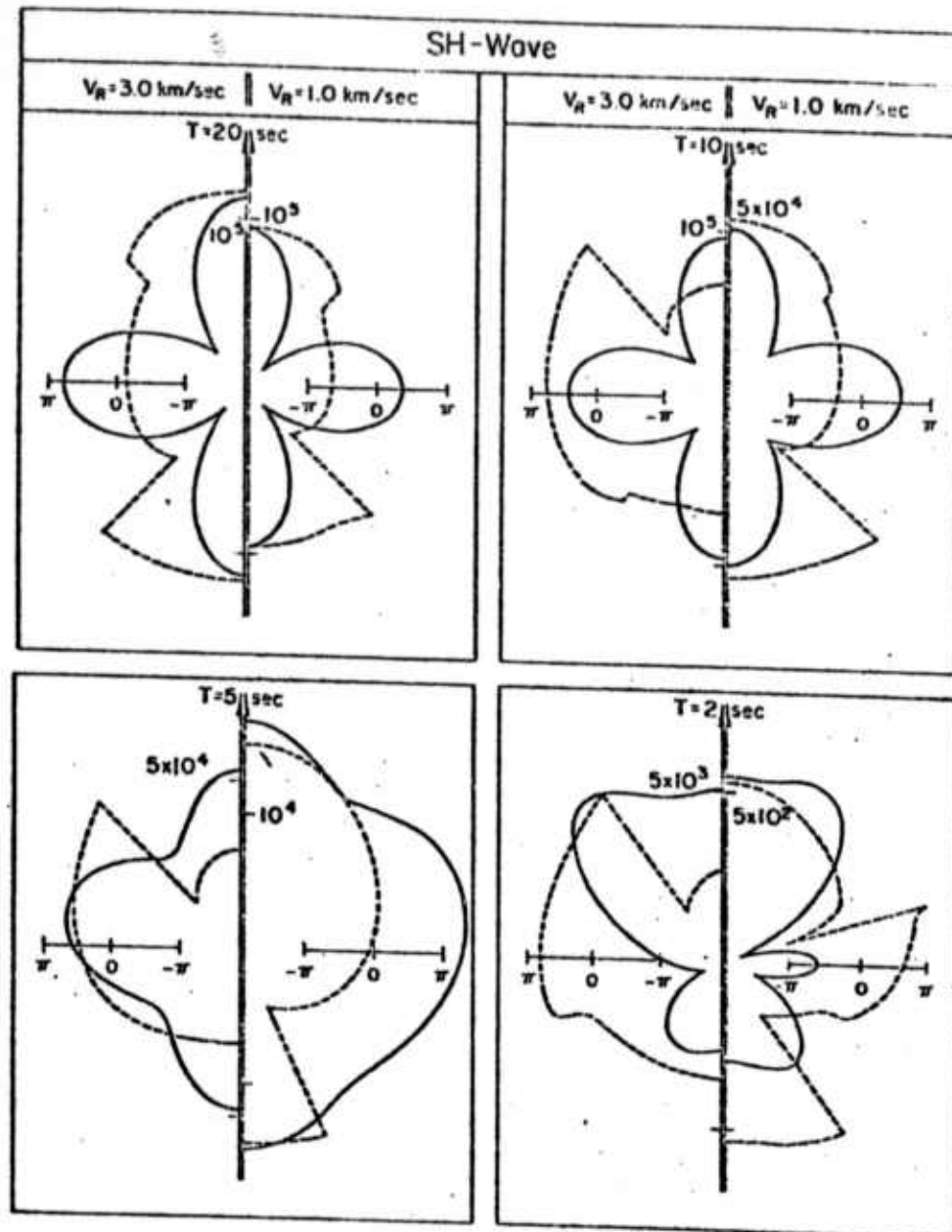


Figure 12, Same as figure 11 SH-wave.

monopolar and quadrupolar, with the monopole component an order of magnitude larger, and there will now be quadrupole S wave radiation.

Inspection of Figures 10 - 12 shows that at low frequency the earthquakes are strong quadrupole radiators, in fact the patterns are nearly pure quadrupole. (Note that half patterns are shown since the full pattern has symmetry about the vertical axis in the figures.) At higher frequency, energy is preferentially radiated in the direction of rupture propagation, indicated by the arrows along the vertical axes in the figures, and the patterns are distorted (rotated) in the direction of rupture propagation. Further, at higher frequencies, higher order multipoles are excited and the patterns loose their strong quadrupole form and actually begin to look more dipolar. Note, however, that the phase maintains a quadrupole form to higher frequency than does the amplitude, especially for the low rupture velocity case shown.

At high frequency ($f = .5$ Hz) the patterns are strongly distorted and complex, yet the phase which prescribes the sense of motion, is still essentially quadrupole. The pattern complexity is due to higher order multipole excitation at high frequency and can be associated with the effects of rupture propagation. (Part of the complexity shown for the high frequency patterns may be due to the fact that the multipole series was truncated in the computations made, and it is possible that inclusion of additional higher multipoles would result in interference such as to give more uniform patterns. But whatever the case, the

patterns do clearly become more distorted from quadrupole patterns, at high frequency.)

The pattern behavior illustrated here has been observed and it is well documented that the pattern is quadrupole at low frequencies and "distorted quadrupole", in the manner indicated here, at intermediate frequencies, (e.g., Lambert et al., 1972). Standard "fault-plane solution" procedures utilizing the sense of first motion of the signals in the time domain, principally for high frequency signals, show also that the phase is quadrupolar or nearly so, to high frequency. This is in essential agreement with these predictions.

In view of these results and the corresponding results for explosions, the P wave radiation pattern for earthquakes is seen to always be radically different than the monopole P wave pattern generated by explosions and is therefore a diagnostic criteria for event discrimination. However identification on this basis requires a large number of observations at many distances as well as azimuths in order to properly sample radiation patterns from earthquakes of all types, and is therefore of limited use. Further, an application of the criteria to a large number of events of all classes is an involved and resource consuming procedure. Nevertheless, it has important application to the identification of particular classes of events.

An interesting feature of earthquake radiation fields that will show up in considerations of the time domain signals from them, is the time delay associated with the release of energy from the source

region (i.e., the source group delay). This time delay t_g is defined by

$$t_g = -\frac{1}{2\pi} \left(\frac{d\phi}{df} \right)$$

where $\phi(f)$ is the frequency dependent phase of the source spectrum.

Figure 13 shows the phase $\phi(f)$ as a function of frequency for an earthquake.

We note that if the phase were a linear function of frequency then t_g would be a constant, and the same for all frequency, so that the time domain signal emitted by the source would be an undispersed pulse.

However as is seen here, the phase curves at high frequency flatten for both P and S waves, but at different frequencies where the strong flattening for the P waves actually occurs at frequencies higher than 1 Hz and has only started to occur in the frequency range shown in the figure. In any case this departure from linearity for the P and S phase curves has two effects, first the signals will be inversely dispersed, that is the high frequencies will arrive before the low frequencies; and second, the S wave dispersion will be inverse, as for the P wave, but different than that for the P wave; such that the low frequencies will be more delayed than those for the P wave, but for the intermediate frequencies, less delayed than those for the P wave. The

group delay at low frequency is approximately equal to L/V_R for both wave types, while at very high frequency the source group delay is zero for both types. This means that the long period radiation derives from relaxation associated with the entire failure zone while the high frequencies arise essentially from relaxation induced by the

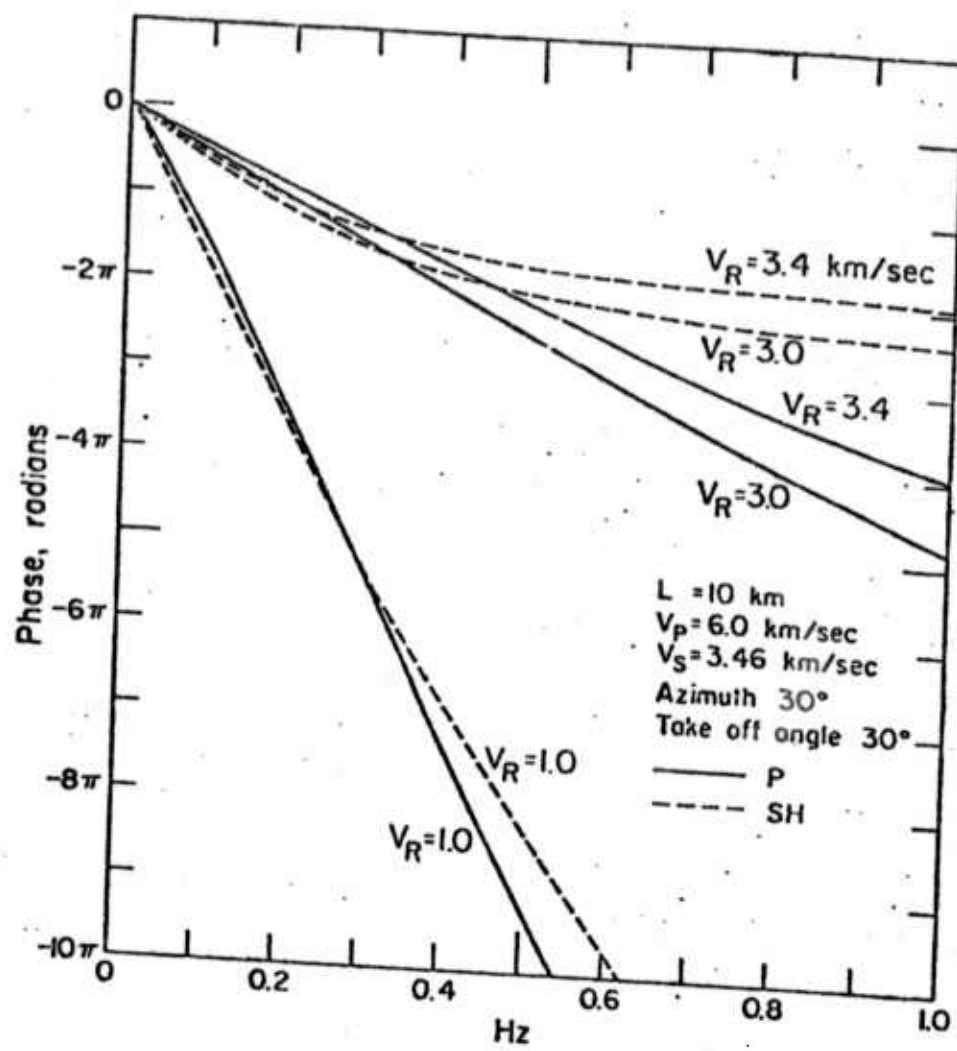


Figure 13. Far-field phase spectra corrected back to equivalent point source. Effects of rupture velocity.

initiation of failure. Further the high frequencies will arrive first at a receiver, so that location of the event based on arrival times of the signals at a net of stations will tend to give a location for the point of the initiation of failure, assuming high frequency seismograms are used for the location. However for band limited systems in the 1 Hz range or lower, this need not be so, depending on the event size and the value of V_R . Further, locations based on S waves will be different than those obtained from P waves generally. In addition these phase curves are azimuth dependent, so that different delays are seen in different directions. The mislocation effects can be large since t_g ranges from L/V_R to zero, and L/V_R will, of course, range from a fraction of a second for very small events to tens of seconds for large events. Thus for precise location of events, which is important for discrimination, these effects should be taken into account. Since these results are new and essentially unverified, although there has been discussion of the phenomenon in terms of the different delays for P and S waves (which has been called the "Z phenomenon"), no effort has been made to take account of them in event location work. It is probable, however, that better depth determinations could be made using this correction.

Aside from these location considerations it happens to be useful that the signals are dispersed in this manner when we come to considerations of frequency dependent magnitudes later in this report. Further, it tells us that if the signal pulse begins with large amplitude,

then the source is rich in high frequencies because they arrived at the beginning of the signal; while if the pulse begins with low amplitude and gradually grows in time, then the source is rich in low frequency and poor in high frequency. Earthquakes produce signals that are more typically of the latter type and explosion signals are more typically of the former type, even when the signal levels are of the same size for these two different events. This then suggests a spectral difference in the events and a means of discrimination that we will exploit. Insofar as the emergent signal characteristics for earthquakes have been commonly observed, although not systematically or quantitatively studied, they are a verification of the spectral predictions for signals from earthquakes; in particular the dispersive properties of the source, and lend further support to the predictions of the theoretical model used here.

The theoretical model predictions of the radiation field spectra can be checked against other theoretical models involving purely numerical approaches to the calculation of the radiation field; that is finite difference or finite element calculations of the response of the medium to failure. Figure 14 shows results for the moving spherical failure model, used in most of the computations of this study, as compared to results from a two dimensional numerical model (Cherry, 1973) in which the source length, prestress, rupture velocity and medium parameters were the same for both calculations. However, the failure zone for the numerical calculation was essentially a plane,

and the physics of the failure process was represented in an entirely different manner, since a particular stress drop was imposed on the system and plastic flow was allowed to occur prior to failure at the rupture front. In spite of the model differences however, we see that two models predict nearly the same field. In particular, the r component of the relaxation model displacement field is comparable to the x and y components of the numerical model field, and we see that at high frequency both give a predicted $1/\omega^3$ frequency dependence. Further, the amplitudes are in close agreement. There are, however, some differences in the details of the spectral variations which may be due to the fact that a spherical component is being compared to cartesian components. In addition, there may be high frequency "noise" generated by the finite difference method or in the Fourier transform of the numerically specified time domain signal. There is also some lack of resolution of detail in the relaxation model calculation, however, since a truncated series of multipoles was used to evaluate the field, which leads to errors at high frequencies. Considering these possibilities the agreement is remarkably good. Furthermore, both model spectra begin to change slope at about the same frequency indicating that both calculations give about the same f_c^H value. Since these calculations are made in the very near field range, the near field terms become dominant near f_c^H , and the far field part of the spectrum is completely "swamped", by the near field at the lower frequencies. It is seen that both models predict the same general trend for the spectrum, a

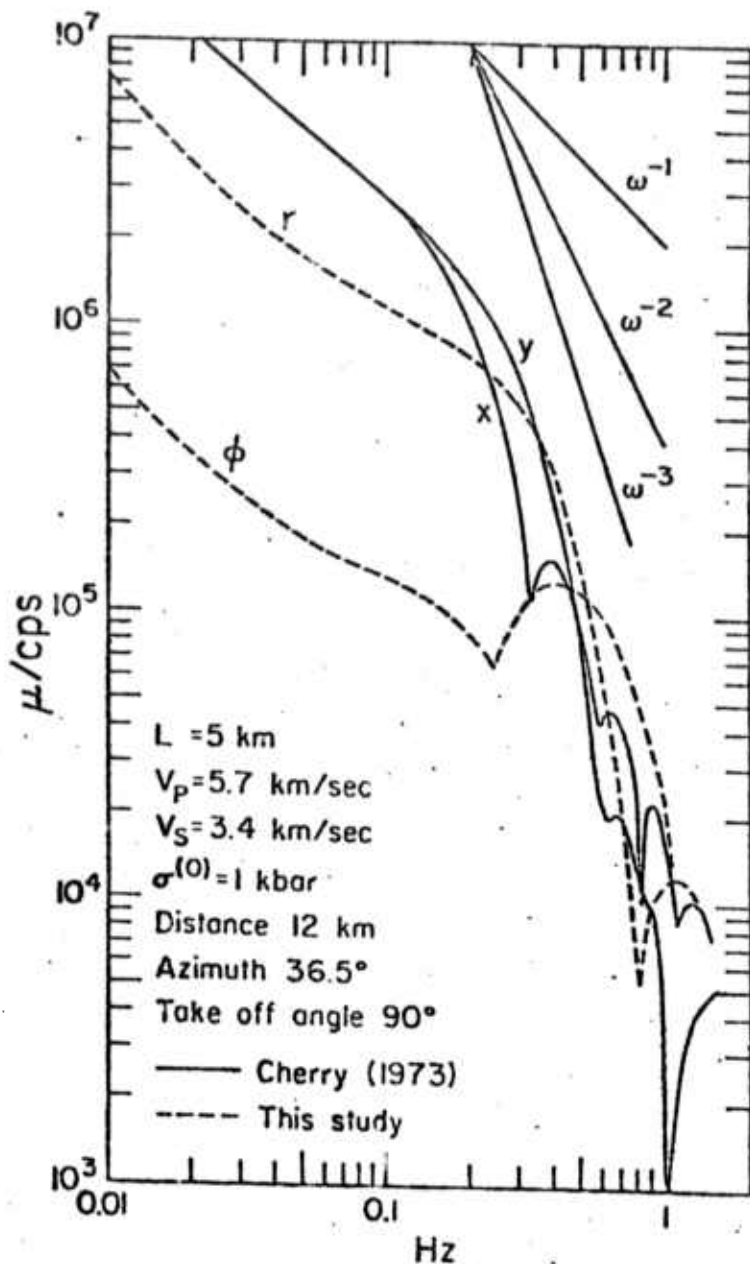


Figure 14. Comparison of spherical rupture model with results from a two-dimensional numerical finite difference code.

behavior with frequency like $1/\omega$ for $\omega < 1$. However, the relaxation model low frequency spectra is displaced downward from that predicted by the numerical calculation. Noting that the relaxation model is a three dimensional space calculation while the numerical model is two dimensional, leads us to conclude that this is as would be expected, since the two dimensional near field decreases more slowly with distance from the source than does the three dimensional field and hence should be larger at this distance. Therefore we conclude that the spectra are in good agreement over their entire range in frequency and that the details of the models are not critical in the description of the radiation field. In particular, the relatively large width of the zone swept out by the moving spherical failure model does not have a profound effect on the spectrum, so long as it is small compared to the failure zone length (i.e., less than $1/4$ say). In addition, non-linear behavior, such as plastic flow at the failure "front" where stress concentrations are high, does not appear to manifest itself directly or strongly in the radiation field, although it is important in determining the rupture velocity, at least in the particular model used for the numerical calculation shown. Finally, somewhat unexpectedly, the rapid drop of rigidity and subsequent "healing" of the failure zone involved in the moving sphere model appears to be nearly equivalent to the particular form of stress drop imposed in the numerical model. This is probably just fortuitous, in that the "effective stress drop" of the moving sphere model just happened

to be close to that chosen in the numerical model. However part of the difference in the long period levels of the two model results could be due to this latter difference in the models or possibly also associated with the plastic flow permissible in the numerical model. In any case the differences are not profound insofar as prediction of the far field spectra are concerned, although not all properties of the far field spectra can be compared in this way since the numerical calculations are restricted to the near field, and the near and far field contributions cannot be separated as they can for the analytical relaxation source calculations. (This incidently shows one advantage of the analytical models, the others being that they are three dimensional and 30 to 40 times faster to compute on standard computers than are the two dimensional numerical models and probably 300 to 400 times faster than any three dimensional numerical model. In addition of course, the very fact that they are analytical allows us to investigate their properties by algebraic means without computation at all, and to obtain scaling laws, etc., besides closed form expressions in terms of known functions for the field itself, all of which help us understand and visualize the properties of the field in a compacted conceptual way. Further, the field can easily be calculated at large distances from the source, which is, in a practical sense, not reasonable if purely numerical methods are used for such a calculation. The numerical models are, however, very flexible in that arbitrary geometries may be considered, complex and spatially variable medium properties

may be incorporated with no difficulty and non-linear rheological behavior of arbitrary form may be treated. Ideally an approach incorporating the best features of both approaches should be arrived at. Two different techniques aimed at an optimal modeling method are now being developed, and should give us nearly complete modeling capability. For the present however, where we confine ourselves to the general features of the radiated field from earthquakes in an effort to isolate large differences between this kind of a source and explosions, the particular relaxation models used in this study appear quite adequate.)

It is of course critically important that detailed comparisons with earthquake data be made in order to verify the theoretical predictions and to check that the model is realistic. It is, in part, a matter of judgment as to what are reasonable values for model parameters, such as prestress, since while the model may be made to fit a given set of observations through a judicious choice of parameter values, the question is whether the set of parameters required is reasonable in terms of what they imply about the physics of the failure process and the earth itself.

The difficulty with such comparative studies is that the basic data is extremely difficult to analyze and interpret, since the earth is sufficiently complex that it acts to complicate the total signal recorded because of the multiple paths available for energy propagation, and also because it filters out energy from the source signal by the

mechanisms of scattering and anelastic attenuation. Thus any uncertainties about the properties of the earth involving elastic and anelastic structure give rise to uncertainties in the interpretation of the field in terms of the source. Further, identification of particular signal types in the time domain, particularly determining where a signal transient begins and ends, is somewhat arbitrary and often done on a subjective basis that is strongly observer dependent. The net result is an uncertainty as to the "identity" of the data obtained and an even larger uncertainty to its accuracy when transformed into the frequency domain in view of the uncertainties concerning the beginning and "end" of the signal transient.

The superposition of all these uncertainties usually makes the interpretation of distant seismic signals in terms of source spectral properties a rather unsatisfactory process from a scientific point of view. However, as our knowledge of the earth and ability to account for the earth's propagational characteristics have improved, so has our ability to infer the source properties improved. Further with the use of more sophisticated time series techniques, better instrumentation, and wider observation coverage, the uncertainties of signal analysis are reduced. Another approach is to try to simply avoid the uncertainties, or minimize their influence, by recording events at very short range in order to reduce propagational uncertainties and complexities and to interpret the total field recorded; treating it as the direct source radiation field. In this case, of course, the time series recorded is in

the near field range of the event, so that, as we have seen, it makes sense to work with the complete recorded signal of all P and S waves as a single "total" signal. The spectrum is then computed from the complete seismogram in the near field and compared to the total spectrum (P plus S wave spectra) of the source.

Figure 15 shows an example of a fit to observed spectra obtained in this fashion for a small strike-slip earthquake of magnitude 4.6. The theoretical source parameters used are indicated in the figure and appear quite reasonable. An anelastic Q factor of 100 was used which modifies the high frequency end of the theoretical source spectrum somewhat. The strain level is $e = 5 \times 10^{-4}$ and corresponds to approximately 300 bars prestress for the medium. The event appears to have been a rather high rupture velocity event. The fit to the observed data in the high and intermediate frequency ranges is about as good as the scatter in the data will allow, although manipulation of the source parameters by small amounts could provide a somewhat more detailed fit to the data. At the long period end of the spectrum, where the near field component predominates, the fit deviates systematically from the observed spectral data, being lower in amplitude and having a different rate of increase with decreasing frequency; in fact having a $1/\omega$ dependence on frequency while the data appears to have a $1/\omega^3$ dependence. The data is almost certainly contaminated by long period noise, of both instrumental and medium origin. Hence the data is known to be too high in amplitude in this range and removal of

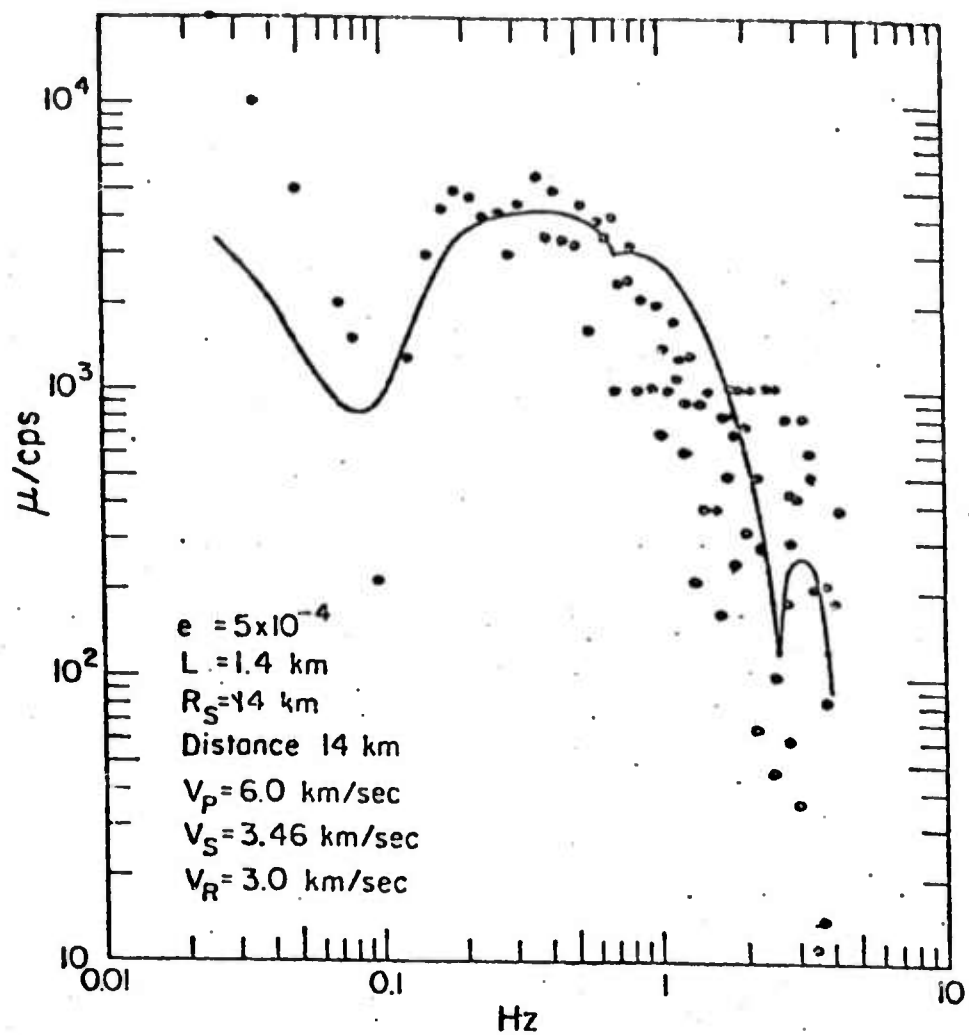


Figure 15. Comparison of observed spectrum from the Harris Ranch earthquake of 27 October 1969 with theoretical spectrum from the propagating spherical rupture model.

the noise would move the corrected data closer to the theoretical curve. For this reason, even though the correction to be applied to the data is quite uncertain, it is felt that the fit is reasonable.

It is important to note that the event spectra appears to require a rather small value for R_s , the 'stress concentration distance-factor', of 14 km. or about 10 failure zone dimensions. This requirement is associated with the presence of the decrease in the spectral level near .1 Hz. If a large or infinite R_s value were used, the theoretical spectrum would have a flat or an increasing spectral level in this range with no spectral minimum at all. Further, this spectral minimum is reflected in the shape of the time signal for the event as well, with the theoretical pulse shape for the peaked theoretical spectra shown in the figure also fitting the very large S wave pulse shape observed. On the other hand the theoretical pulse shape for a large or infinite R_s value deviates in a noticeable way from the recorded S wave pulse, which is by far the dominant signal form on the entire seismogram.

We therefore conclude that all the spectral features we have discussed are represented in the data shown in Figure 15; in particular the characteristic frequencies f_c^H and f_c^L , the high frequency $1/\omega^3$ slope, the flat or broadly peaked level in the intermediate frequency range, the decrease of the far field spectra for $f < f_c^L$ due to finite R_s , and the near field component contribution becoming important for frequencies such that $1/f = T \geq r/V_s$ and behaving as $1/\omega$ as a function of frequency.

The observations of numerous small earthquakes in this near field range are generally similar to this example. However there are variations dependent on the tectonic area of the survey: there are regions of survey where many if not most event spectra show the spectral decrease indicative of "small" R_s , while data from different areas do not often show such minima. Thus it appears that the stress zone dimensions can often be small enough to be manifested in the observed spectra, while in other areas the prestress is uniform over a large region with large enough R_s so that f_c^L is so low that it is within the near field frequency band and not observable. In any case, there appear to be classes of events with small R_s - that is events occurring within high stress concentration volumes of relatively small dimensions. As we have seen in Figure 9 this will result in a spread in the earthquake population at low magnitude, with the events of small R_s being most explosion-like and therefore most critical for event discrimination between earthquakes and explosions of all types.

(b) Time Domain Signal Properties

Most seismological observations are made directly in the time domain. In particular, the important magnitude parameters, m_b and M_s , are generated from time domain measurements. Therefore in order to compare directly to the measurements we want to produce theoretically generated time domain signals and make measurements from these in precisely the same way as they are made in observational work. We do not, therefore, introduce non-essential uncertainties in interpretations of the observed data in terms of theoretical models. We therefore consider, in this section, the nature of the time domain signals and the spectrums associated with these signals at teleseismic distances as they would be recorded by standard seismometers.

In part (c) the m_b and M_s values measured from the theoretical time domain signals are compared to some of the observed data.

Figures 16 and 17 show the amplitude response of standard seismometers used for the long range seismic monitoring program (LRSM), Project VELA Uniform. We will compare theoretical seismograms, filtered by these instruments, to actual seismic data recorded by the field array of LRSM stations.

In order to account for the propagation of the energy from the source to an arbitrary receiver, we will approximate the high frequency propagation by a ray theory calculation and the low frequency (surface wave) propagation by an exact wave theory calculation in a

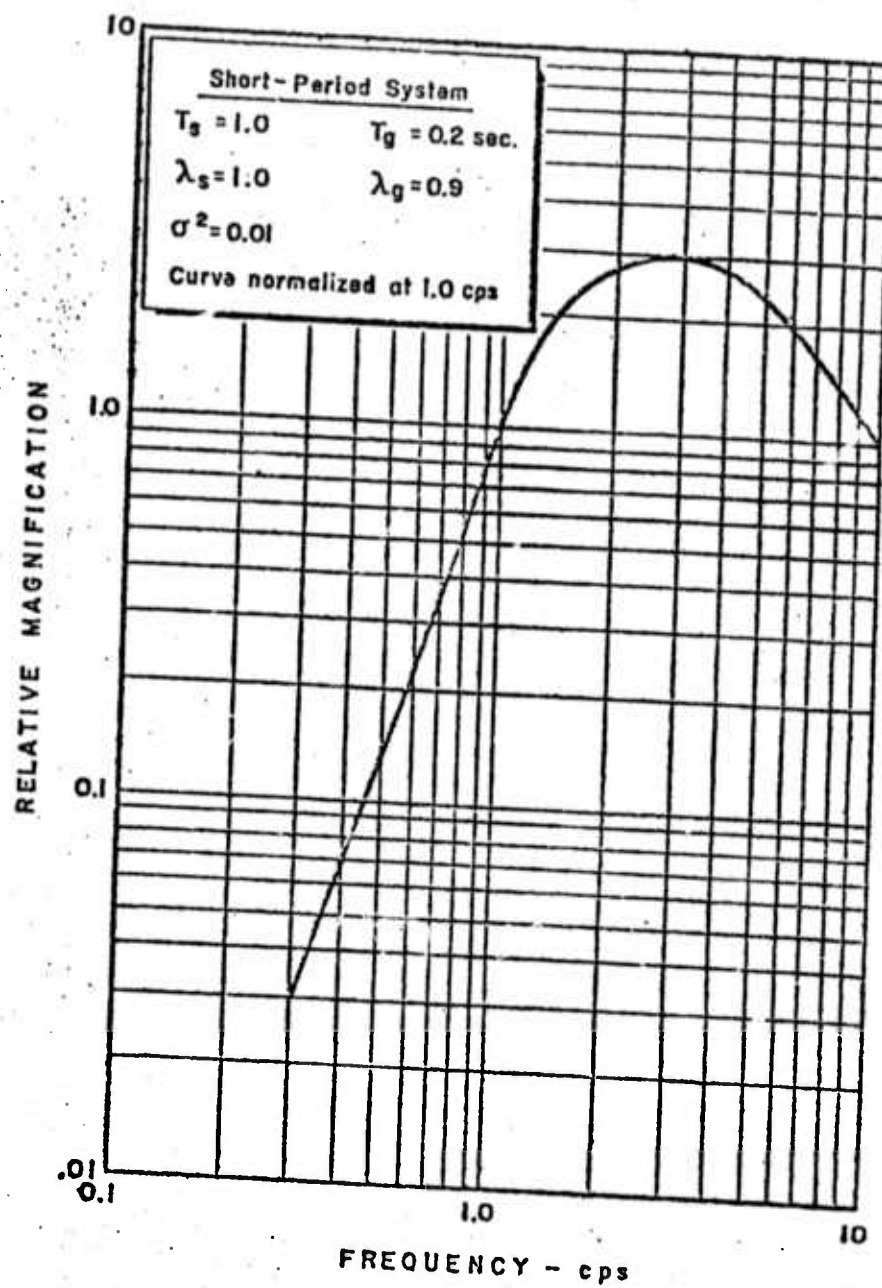


Figure 16. Instrument response of the LRSM short period seismograph

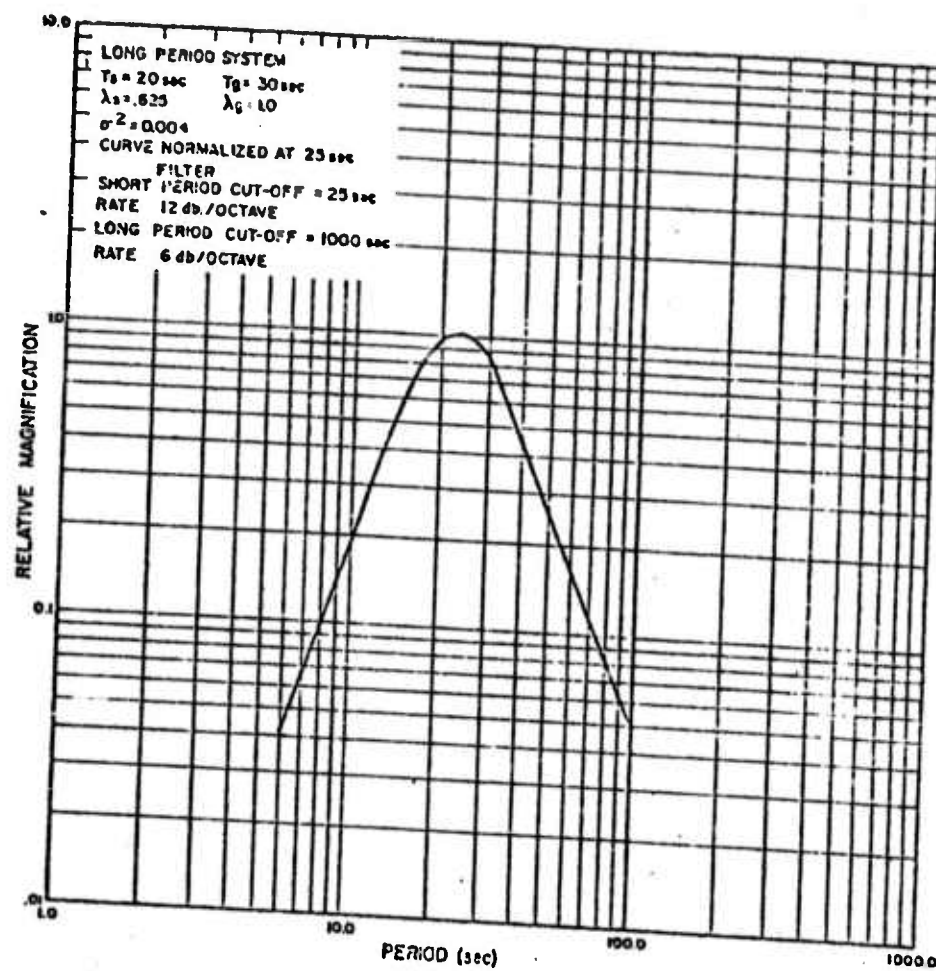


Figure 17. Instrument response of the LRSM Long Period Seismograph.

layered half space approximation for the earth. For the ray theory calculations, which are applicable to signals propagated as body waves in the earth, we use a continuously varying elastic velocity model of a spherical earth, where the velocity is constrained to vary radially. When necessary, lateral variations in earth structure are taken into account in this approach by using different "mean earth models" for different source and receiver locations. The "flat, layered earth" approximation is perfectly adequate for surface wave calculations at periods less than 200 seconds. Since our interest here is in surface waves in the period range near 20 seconds, this approximation of the earth is more than adequate.

Figure 18 shows velocity models of the earth obtained from both body and surface wave studies, the structures shown are from Archambeau et al., 1969 and Helmberger (personal communication, 1974). They are obtained from data recorded over different parts of the U. S. and indicate, by their differences, the variation in velocity to be expected for different areas in the continent. However, the differences at depths greater than 300 km. are considered to be more a measure of the uncertainty in velocity variations in the earth's upper mantle. In this study, the CIT 109 models will be used primarily. (This does not mean that these are considered to be more accurate, but only that for the computations made, it happened that these models were available in a form from which it was easy to generate results.)

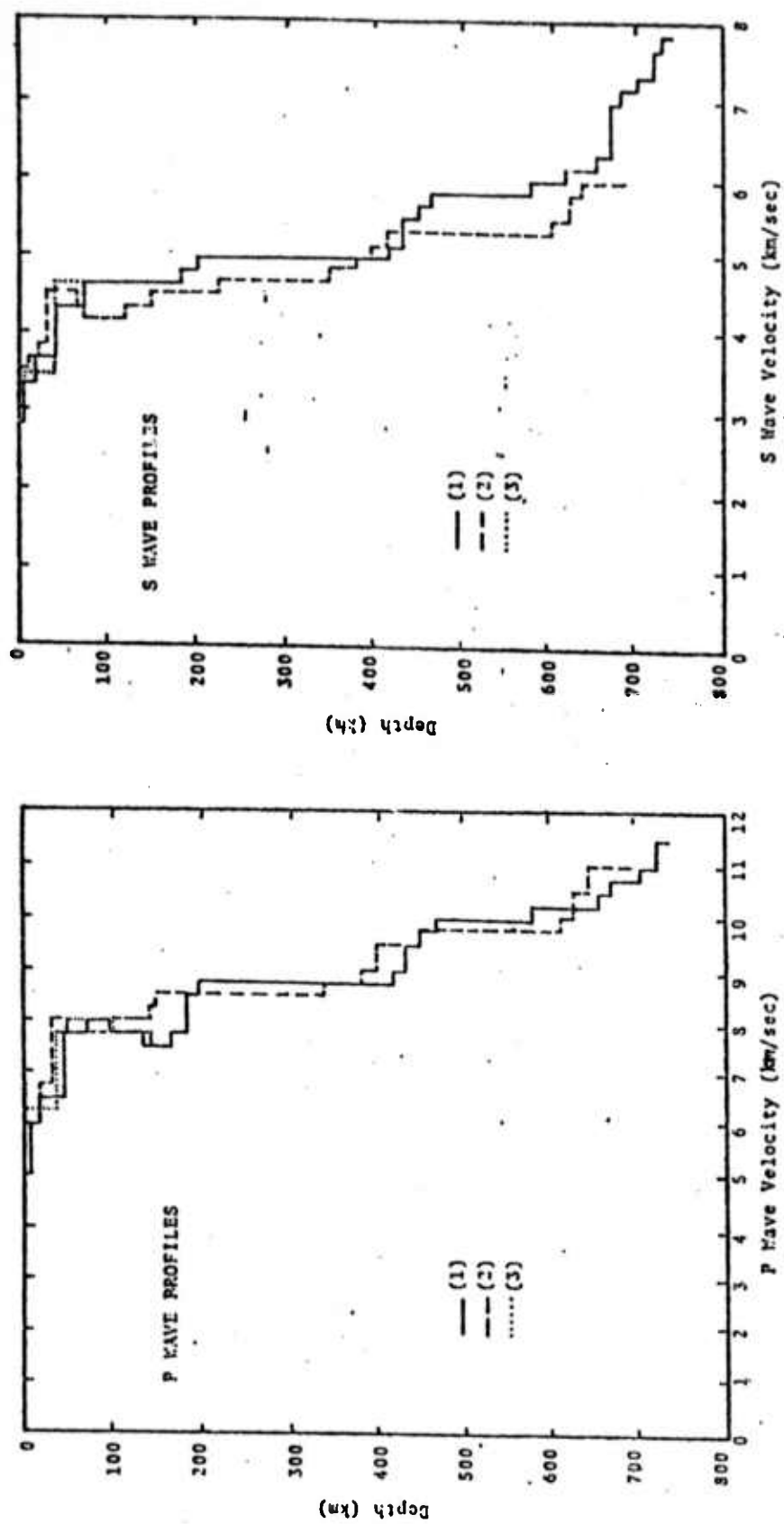


Figure 18. P and S wave velocity versus depth for three models of the crust and upper mantle. Line (1) is Fallon to Ruth crust, over Helmberger mantle; line (2) is model CIT 109; line (3) is NTS Granite crust over Helmberger mantle.

Figure 19 shows a more detailed plot of the compressional wave velocity variation with depth, for the depth range required to calculate body waves out to epicentral distances, Δ , of about 6000 km. In the surface wave propagation calculations, only the upper 100 km. is important for the wave lengths of interest in this study.

In addition to the elastic velocity structure, the anelastic properties of the earth are important in the wave propagation calculations, especially for the body wave calculations at high frequency since the energy loss due to anelasticity is exponential with frequency. Further, anelastic dissipation also causes a frequency dependent phase shift (see, Futterman, 1962; Strick, 1970; and Cherry et al., 1974) which is a strong effect at high frequency, and this must be taken into account. Convenient expression of the anelastic properties of the earth can be obtained in terms of the intrinsic quality factor, or dissipation function, Q for the material. Figure 20 shows the depth variation of the dissipation factor for P wave S, Q_p , as obtained from body and surface wave studies by Anderson and Archambeau, 1964 (low Q model) and by Archambeau et al., 1969 (high Q model). The high Q model was obtained from studies of the amplitude attenuation of high frequency body waves, while the low Q model was derived from low frequency surface wave studies. There is a corresponding Q function for S waves, Q_s , which has a similar variation with depth in the earth, but with uniformly lower value than Q_p . (See

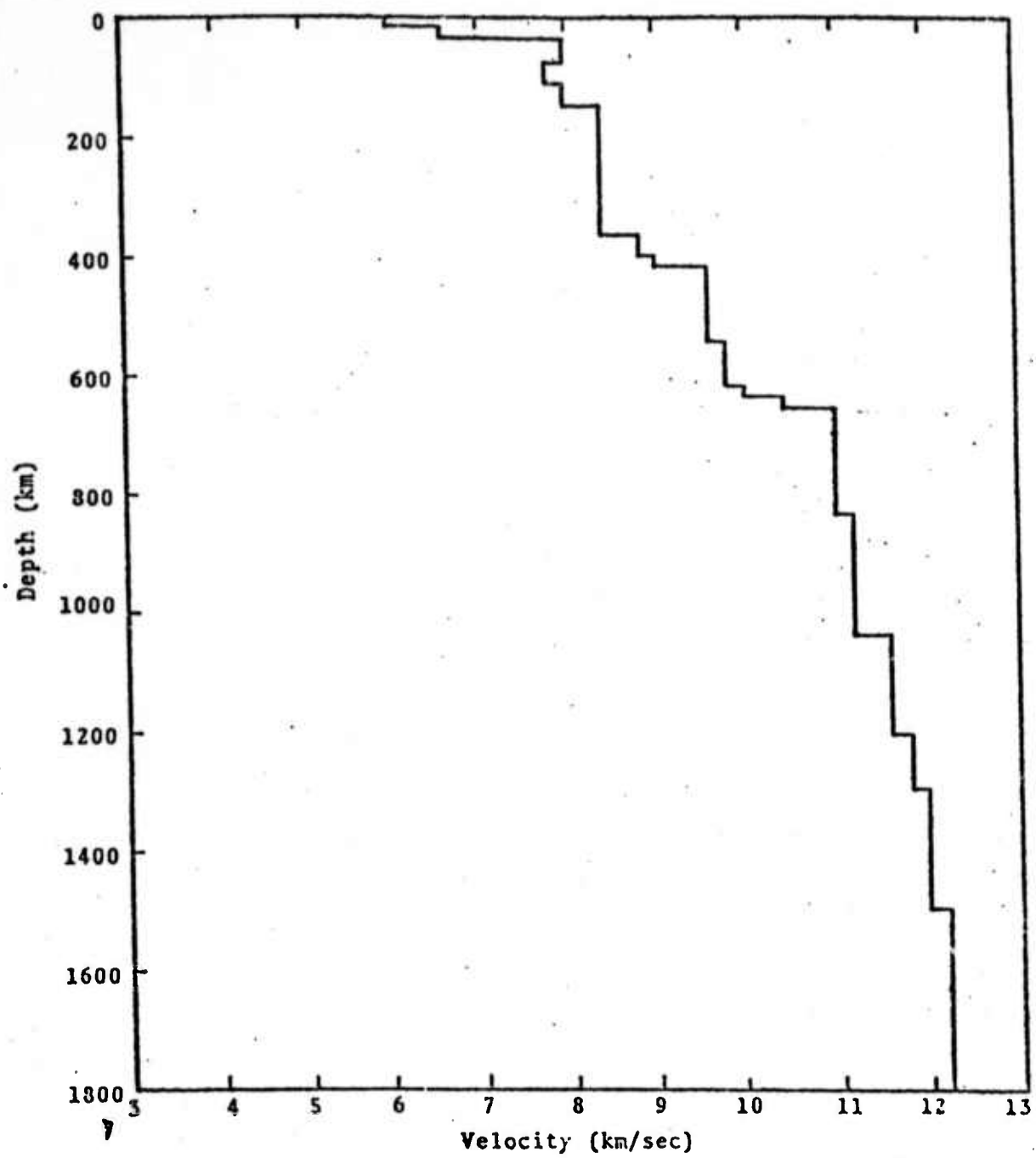


Figure 19. CIT 109 compressional wave velocity versus depth profile for the upper mantle, Basin and Range Province

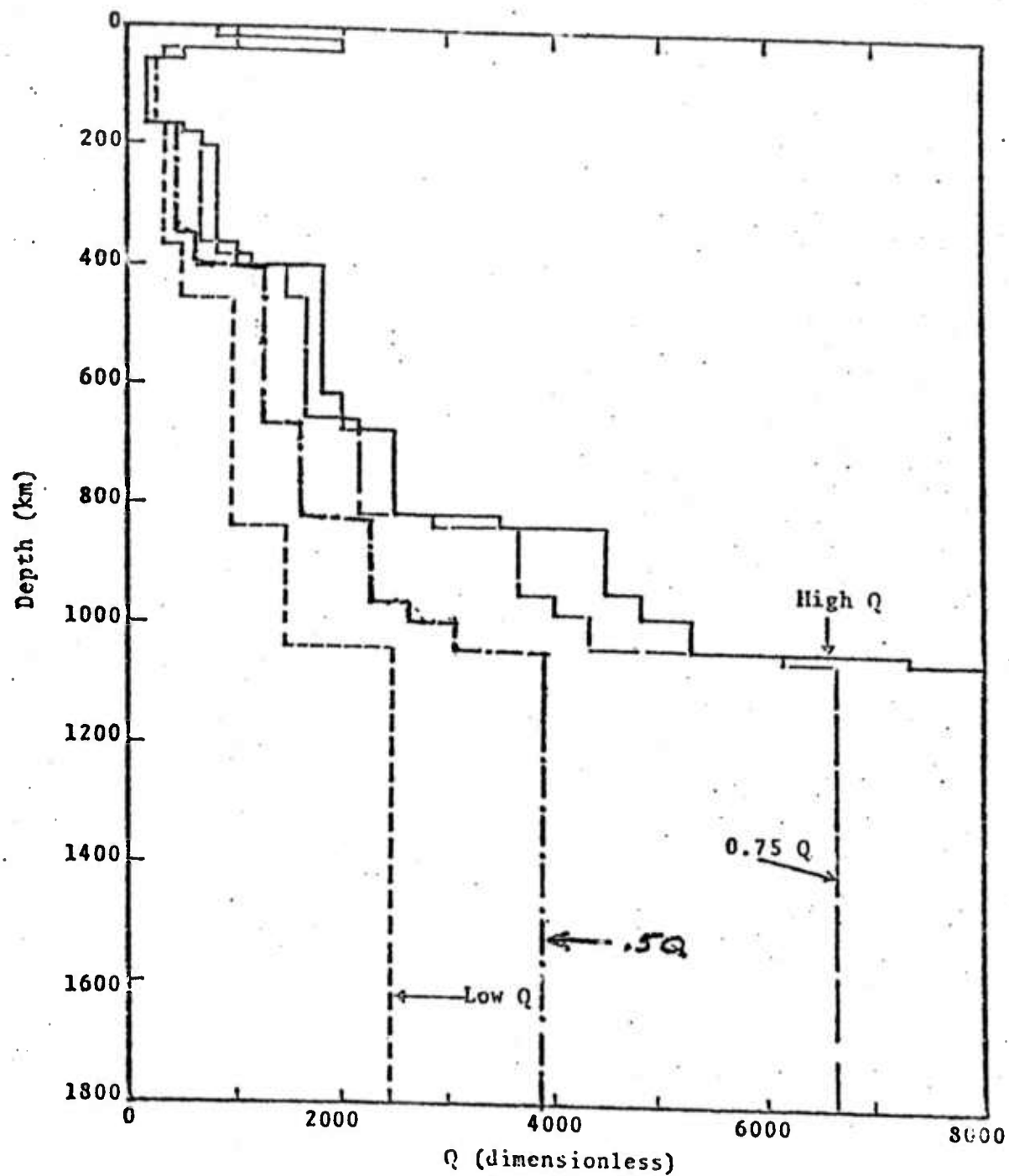


Figure 20. Depth profiles of the dissipation function Q_p . The $.5Q$ model provides the best fit to explosion and earthquake data in the .3 to 3 cps. range.

for example Anderson and Archambeau, 1964.

In preliminary investigations of the effects of Q_p on body wave amplitudes and pulse forms from earthquakes and explosions, it was found that the ".5Q" model shown gave results which were consistent with observations from both kinds of events. We therefore use the .5Q model in the body P wave calculations in this study. A Q_s model very similar to that given by Anderson and Archambeau, as model MM8, is used for the surface wave and S wave attenuation Q_s factor.

The rather rapid velocity variations in the upper mantle of the earth in the "low velocity zone" starting at 30 to 80 km. depth and extending to a depth of 100 to 200 km. (the precise depths depending on tectonic region), as well as the velocity increases near 400 and 600 km., give rise to complicated travel-time curves for body waves and, as a consequence, complicated observed amplitude variations with distance for first and later arriving body wave signals.

Figure 21 shows the variation in the P wave travel time as a function of distance from a shallow source, at 400 meters depth from the surface of the earth, for the velocity structure CIT 109P of Figure 19. The data are from the Bilby underground explosion test and this data was used, in part, to generate the CIT 109P velocity profile. The travel time curve is multi-valued and this gives rise to multiple arrivals within the distance range shown. We term these "P wave mantle arrivals" and denote them as "first, second, third, etc. mantle arrivals"

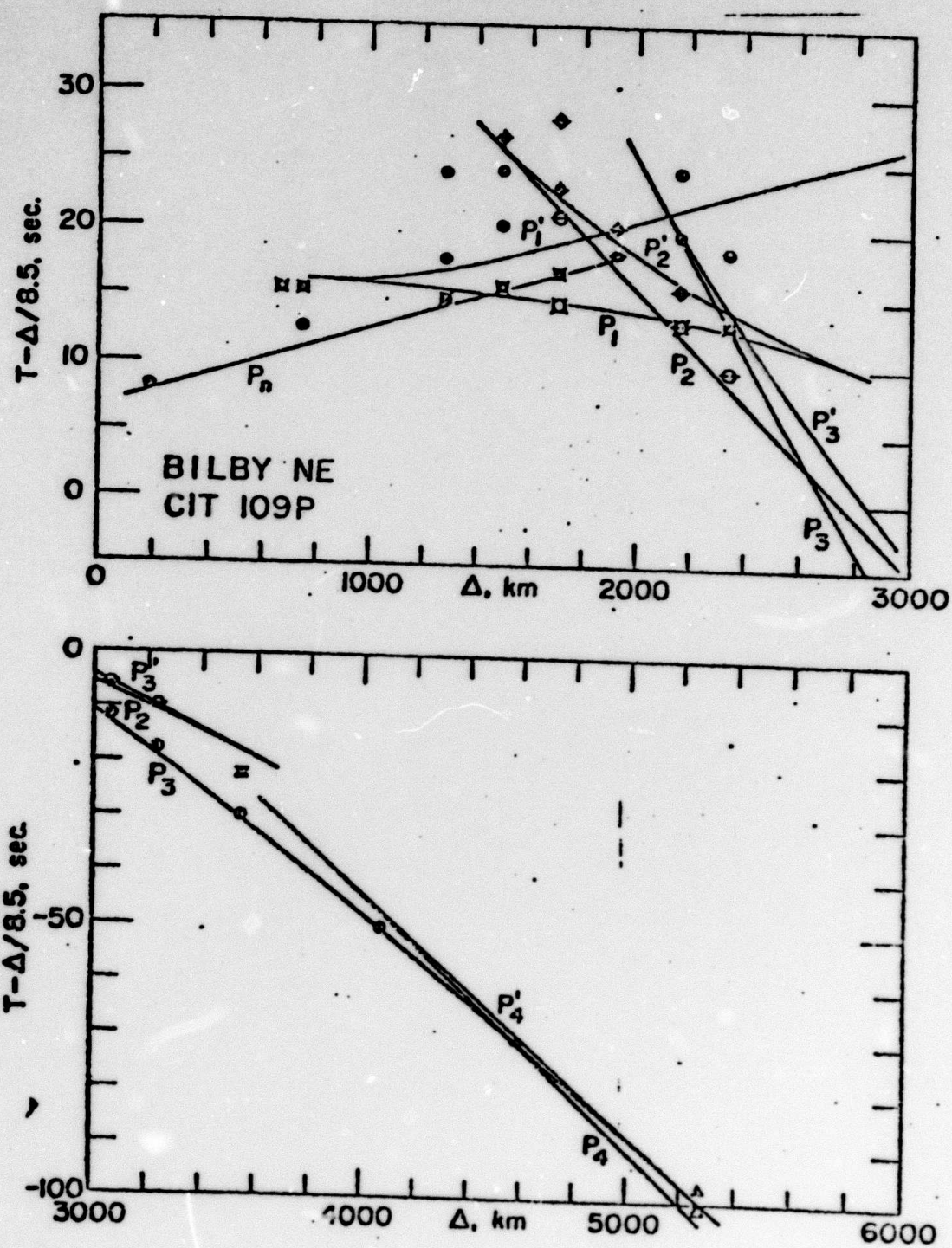


Fig. 21 --Travel time versus distance curve for the CIT 109P structure. The points shown are observations for the Bilby event. Note the multiple branches of the curve, which arise from the presence of the low velocity zone and velocity transitions at 400 and 650 km in the upper mantle. (Archambeau, et al., 1969).

at a given distance. The "branches" of the travel time curves are denoted P_n , P_1 , P'_1 , P_2 , etc. in the figure. Thus an arrival associated with one particular branch of the travel time curve may be the first arrival at one distance, but the second, third or later arrival at other distances. For example at $\Delta = 1600$ km. the P_1 branch gives the first arrival, followed by a P_n arrival less than two seconds later, then a third arrival from the P'_1 branch about four seconds after the first arrival and finally five seconds after the first arrival two more arrivals, separated by less than a second in time, due to the P_2 and P'_2 branches. On the other hand at 2200 km. the sequence of arrivals is P'_2 , P_1 , P'_2 , P_3 and P'_3 , all rather closely spaced in time. This leads to a rather complicated superposition of signals in time, so that seismograms, in the distance range where the travel-time curve is complicated, are also complex. Further the first arrival "phase" as it appears on a seismogram may actually be the superposition of several distinct signals since these curves show that the various mantle phases will arrive with very little time separation after the first onset of ground motion. Finally, we see that the first arriving signal corresponds to different branches of the travel-time curve at different distances and since these mantle arrivals are distinct signal transients propagating over different paths within the mantle of the earth, the amplitude of a first arrival phase will often change rather drastically when passing from one branch of the travel

time curve to another as distance is varied. Hence, for two observations on either side of the distance point where the travel time curves for two branches cross, one could observe quite different amplitude characteristics for the first arriving signal. In fact the whole signal train composed of the many mantle phases could change rather drastically.

The actual nature of the amplitude change with distance for compressional body "phases" is shown in Figure 22. Here we have plotted the transfer function for the earth as a function of distance for the 1 Hz. frequency component of the first, second and third mantle P waves. These, of course, are theoretical transfer functions using the ray theory approximation and including the effect of anelasticity on the amplitudes. The amplitude of the 1 Hz. spectral component of the various mantle phases is obtained by multiplying the source spectrum at 1 Hz. by the appropriate mantle phase transfer function. Similar transfer functions for the entire band width of interest can be computed from the structure models of the earth, so that the entire source spectrum can be scaled by the earth's transfer function and hence the effect of propagation from source to receiver at any distance taken into account. To obtain the time domain signal pulse then, it is only necessary to inverse Fourier transform the new spectrum obtained after scaling by the filter function of the earth.

The transfer function also includes, in addition to the amplitude effects illustrated in Figure 22 for one frequency, a phase shift

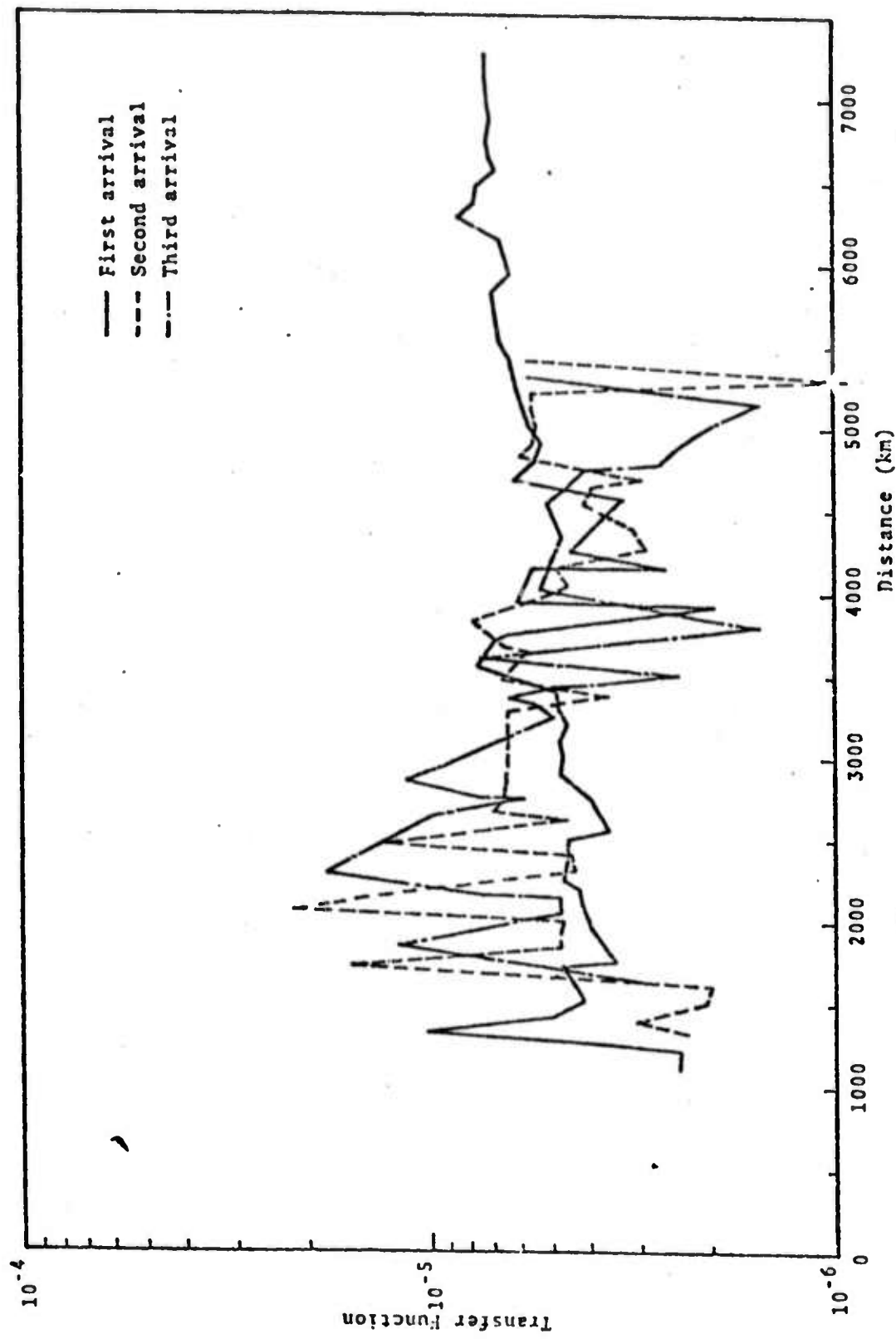


Fig. 22 --Transfer function versus distance for earth model CIT 109P; 0.75 Q (for an event at a depth of 700 meters). The arrivals within 100 km intervals are ordered by travel time (Cherry et al., 1974).

associated with anelastic attenuation which is non-linearly dependent on frequency plus the ordinary phase shift due to propagation time. The latter is a linear function of frequency and just gives a constant shift in time to the whole signal corresponding to the ray theory travel time, T . The anelastic phase shift however gives rise to dispersion of the pulse so that different frequencies are delayed by different times. The analytical form used here for this anelastic dispersion effect is that given by Strick (1970). Neglecting the linear phase shift associated with the ray theory propagation time, the transfer function, $\mathcal{J}_m(\omega, \Delta)$, for the m^{th} mantle phase has the form

$$\mathcal{J}_m(\omega, \Delta) = \bar{\mathcal{J}}_m(\Delta) \exp \left\{ -\frac{-\omega T_m(\Delta)}{2 \bar{Q}_p^m} \left[1 - \frac{2i}{\pi} \ln(\omega_h/\omega) \right] \right\}$$

where $\bar{\mathcal{J}}$ is just the frequency independent radial spreading factor obtained from the ray calculation for the medium, $T_m(\Delta)$ is the ray travel time to the distance Δ , \bar{Q}_p^m is the path averaged effective Q for the m^{th} mantle P phase, and ω_h is a high frequency cut-off for the anelastic effect considered.

The application of the procedure just outlined, that is multiplication of the source spectrum by $\mathcal{J}_m(\omega, \Delta)$ and the instrumental transfer function, followed by inverse Fourier transformation of the resulting spectrum, yields the pulse form in the time domain corresponding to the source radiation field as it would be recorded at a distance Δ by a seismometer with transfer function $I(\omega)$.

Figure 23 shows the result of such a calculation for the P wave "signal train" from a 2.5 km. length earthquake. The basic wave form of the first arrival P wave recorded at 4000 km., by a short period LRSM seismometer, is shown at the top of the figure. We will take into account all reflections at the free surface of the earth. Therefore, for compressional waves arriving at a teleseismic receiver the reflected P wave at the surface (pP) and the converted S wave (sP) will arrive as P phases at the receiver. These phases are shown, as they would be individually recorded at the receiver, in the second and third traces in the figure. The fourth trace from the top shows the superposition of these phases. Since these individual phases leave the source region at the same angle with respect to the vertical through the hypocenter of the event, they travel through essentially the same part of the mantle and arrive at the receiver as a complex "mantle phase", made up of P, pP and sP . As previously discussed, there are usually several paths through the mantle of the earth which will contribute to the total displacement of the medium at a given distance from the source. The ray paths differ in the transfer function associated with them and hence in the travel time of the wave from the source to the receiver. Hence we can have several mantle phases, each composed of a superposition of direct and reflected waves, arriving within a short time interval. At the 4000 km. distance chosen for the calculation illustrated, there are 3 possible mantle arrivals.

60.A

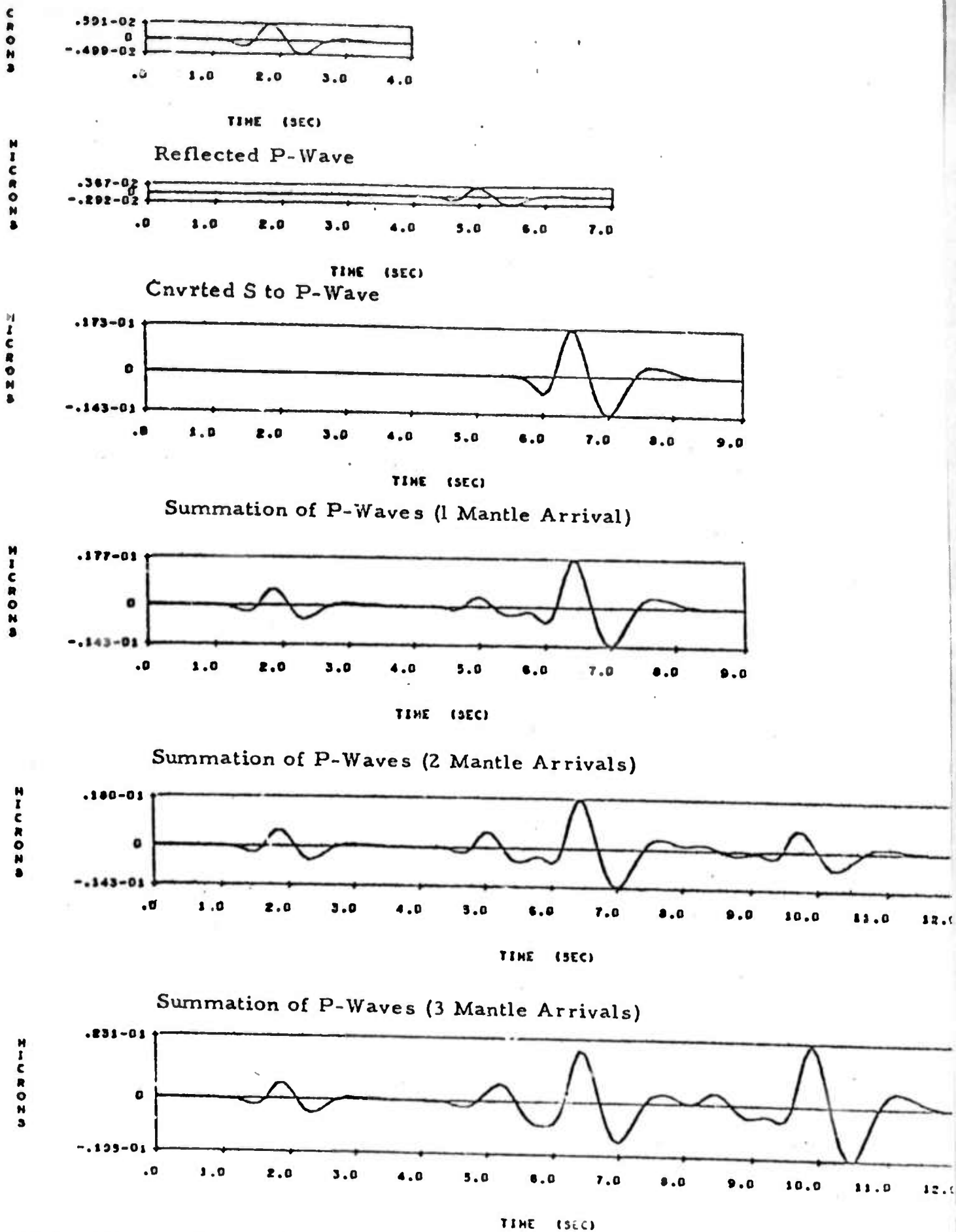


Figure 23. Synthesis of a compressional wave seismogram for an earthquake of fault length $L = 2.5$ km. Distance 4000 km, azimuth 30° .

The fifth trace shows the sum of the first two mantle phases, each a composite of P, pP and sP from the source region, and the bottom trace is the sum of all three mantle arrivals. The lower trace is then the complete composite P wave train that would be received at $\Delta = 4000$ km. This predicted seismometer output, where we have included the LRSM seismometer transfer function in the calculation, is a reasonably comprehensive representation inasmuch as we take into account all major source properties, all the major reflected phases and all possible mantle paths. It is, however, an approximation to what can be expected; in several ways. First, of course, there are several approximations involved in the source representation as previously discussed. In addition to these however, we have not taken into account reflections and conversions within the crust of the earth, except those at the free surface. Since the velocity contrast between layers in the crust can be large, reflected and converted energy at the layer interfaces can be significant and would give rise to additional "delayed" signal or "reverberations", at both the source and the receiver. This would result in a more complicated signal form than that shown in the figure. Further, we have used ray theory to calculate the geometrical effects of wave propagation; and while this approach is adequate for the prediction of the first arriving mantle phase in particular, it is a rough approximation for some of the later arriving

mantle phases. In particular, if the distance at which the prediction is made is near a caustic, then the amplitudes predicted for the later arriving mantle phases will be too large.

In view of these approximations, as well as others of lesser significance, we expect that we can quite accurately predict the first few seconds of the P wave train signal but that the later part of the signal train will lack detailed agreement with observations. We know, in fact, that the displacements at later times will be higher than that observed, in general, and that they will lack the complex features generated by crustal reverberations at the source and receiver sites. However, there are instances where we have generated P wave train signals that are in remarkable agreement with observed signals. This appears to be the case when we select receivers that are located at sites where the crustal structure is simple and when the source location, depth, etc., are accurately known, so that we have a situation approaching our model configuration and a source whose location we know accurately.

The significant point here is that we can predict the most important characteristics of the P wave train and that we know in what ways the predictions will deviate from the observations. We conclude therefore, that this approach is quite accurate for purposes of magnitude prediction in particular. More generally, we conclude that

those features of the entire wave train essential for discrimination are accurately predicted.

To illustrate some of the features of earthquake P wave signals that are important for discrimination, particularly for body wave magnitude determinations, we show examples of the P wave signal train for earthquakes of various sizes at a fixed distance and azimuth. We also fix the failure surface location and orientation, prestress, rupture velocity and medium parameters; allowing only the rupture length to change. Thus we can study the effect of earthquake size, expressed in terms of the maximum rupture dimension, on the signal form. In addition, we consider the effect of the superposition of mantle arrivals by displaying first the signal corresponding to the first arriving mantle phase and then the composite signal due to all mantle phases arriving at the distance in question.

Figure 24 shows the P wave train for the 2.5 km. dip slip earthquake previously illustrated in Figure 23. The upper trace shows the first mantle arrival alone, and the prominent later arriving phase is sP. This phase is large and is characteristic of shallow earthquakes, in this example the depth of the hypocenter is 10 km. Of course the size of the P, pP and sP phases represented in this mantle arrival will be dependent on the azimuth and distance from the source, due to the quadrupole like radiation patterns associated with

63.A

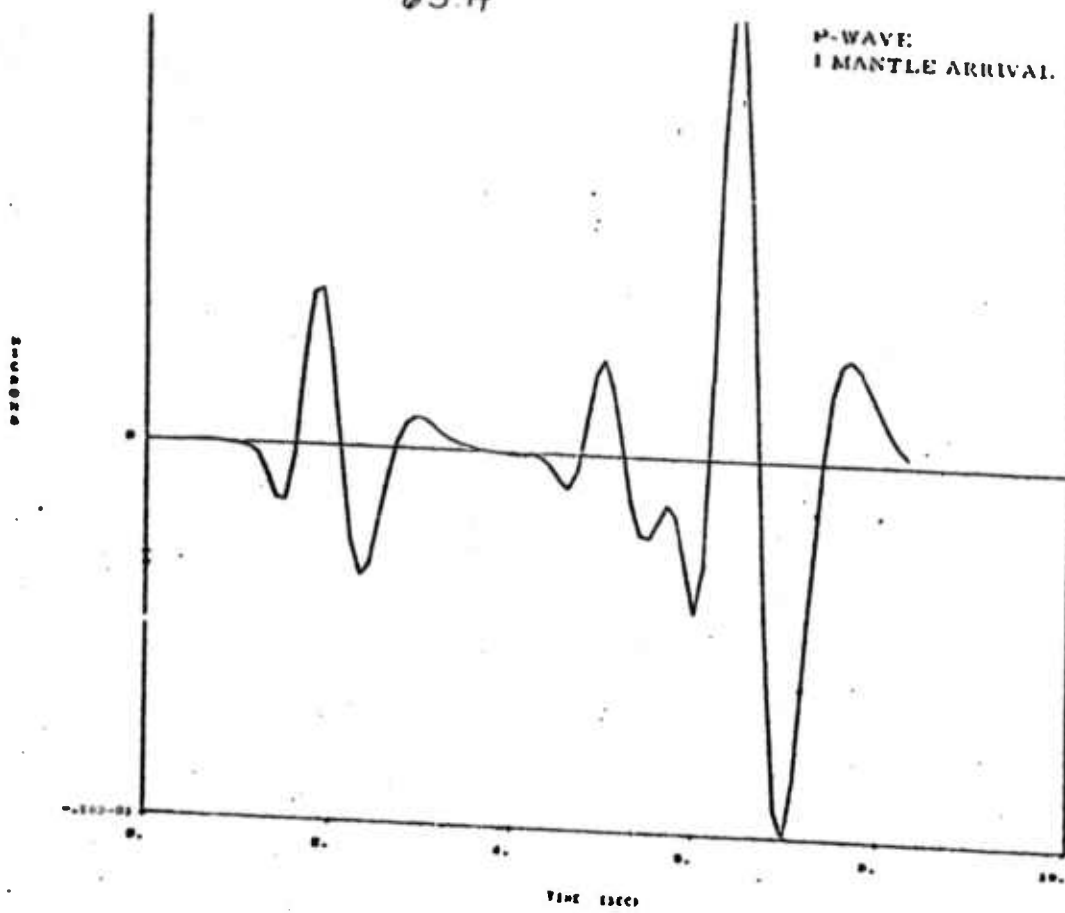
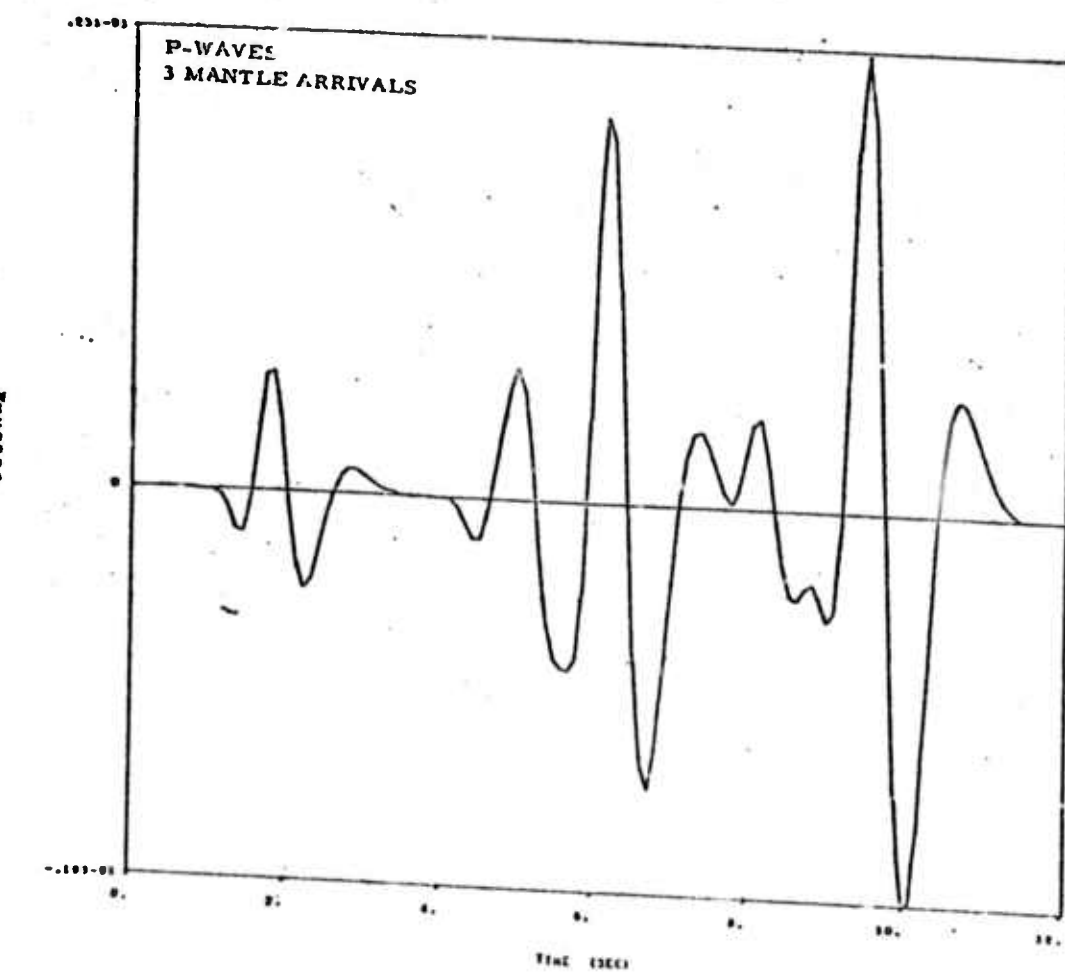
P-WAVE
1 MANTLE ARRIVAL.P-WAVES
3 MANTLE ARRIVALS

Figure 24. Theoretical earthquake ($L = 2.5$ km.) compressional wave train, showing a distinct and large SP phase and effects of later arriving mantle phases. Dip slip event, 500 bars prestress, distance 4000 km., azimuth 30° .

the P and S waves. The lower trace is the superposition of all three mantle arrivals predicted at this distance and the largest pulse (near the 10 second time) is due to a superposition of sP phases contained within the second and third arriving mantle phases. The first pulse on both traces is the direct P wave contained in the first arriving mantle phase. If a magnitude is measured from this synthetic seismogram in the conventional manner, namely by measuring the largest peak to peak amplitude in the first two or three cycles of motion, then the cycle beginning just before the 2 second mark and ending just after this time point would be used in the magnitude calculation. In this case the magnitude computed would reflect the amplitude, near 1 Hz., of the direct P wave from the source. It is conceivable, but not too likely, that one of the sP phases would be used for the magnitude calculation under noisy conditions where the direct P wave could not be clearly identified. In such a case of course, the resulting magnitude would be much larger than the proper magnitude for two reasons, first because we would be measuring the superposition of several mantle arrivals and second and most importantly, because the dominant phase in this composite is sP, which is large because of the relatively high efficiency of the earthquake as an S wave generator.

This possibility becomes more likely for a larger event.

Figure 25 shows the wave trains for a 10 km. fault. Now the

64-A

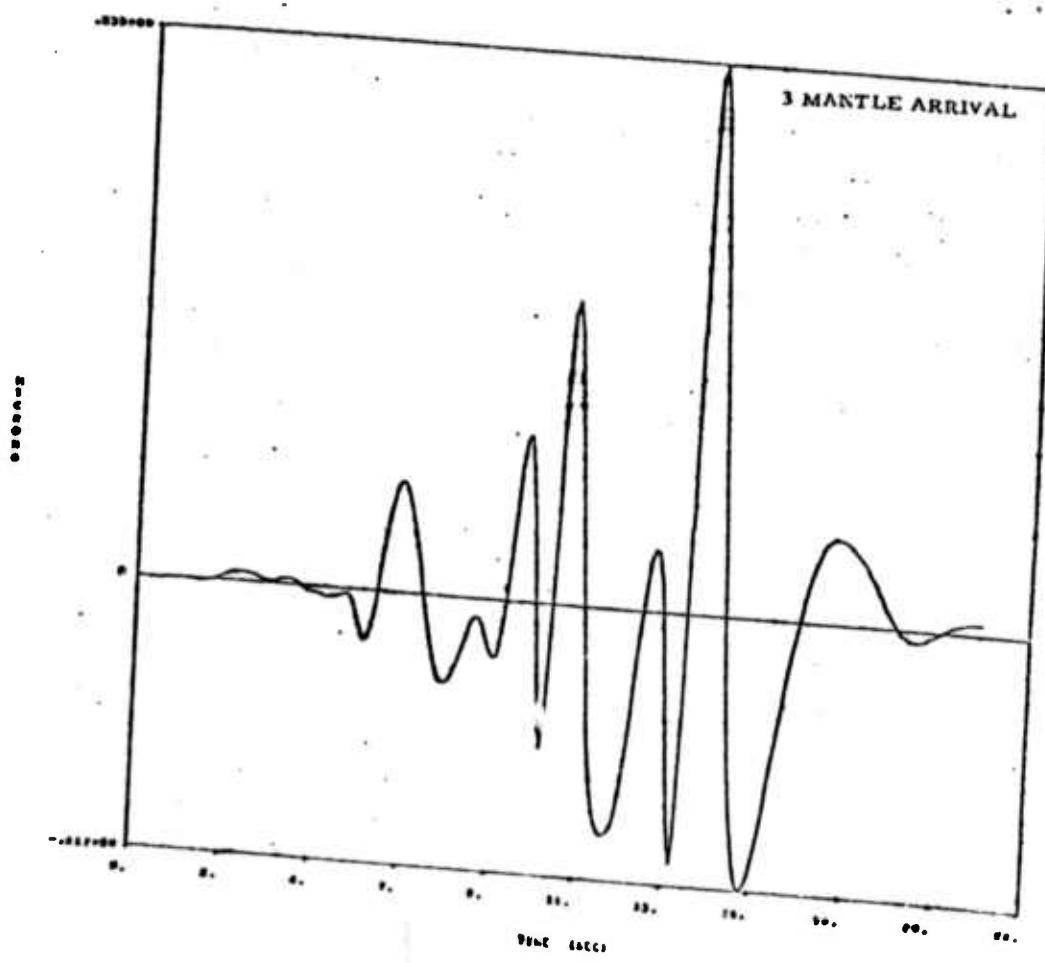
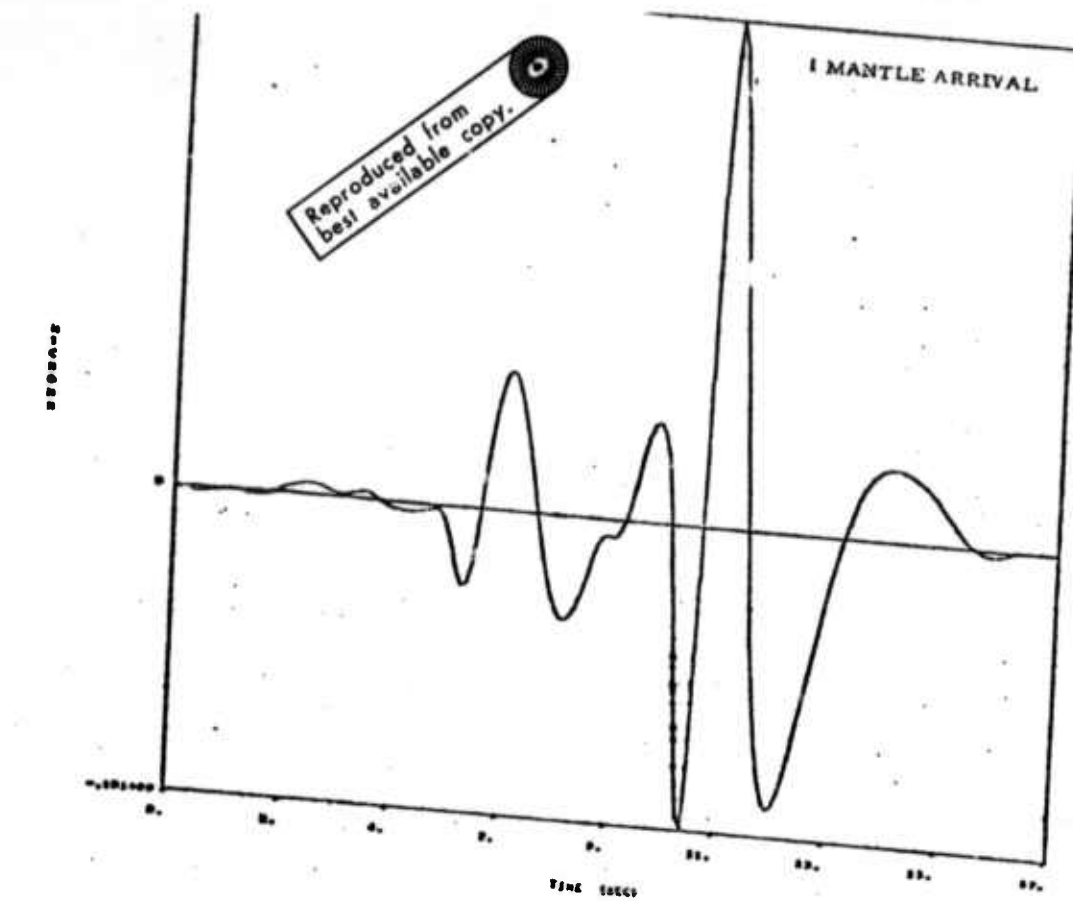


Figure 25. Theoretical earthquake ($L = 10$ km.) compressional wave train with same event parameters as in Figure 24. Largest amplitude cycle is sP contribution and for the 3 mantle arrival and for the 3 mantle arrival superposition the largest amplitude is due to the superposition of the second and third sP mantle phases.

dominant period of the radiation observed is somewhat larger, and the individual "phases" overlap in time more strongly. Since we have fixed all the parameters to be the same as for the 2.5 km. event, the phases making up the wave train are the same as in the previous example. In particular, the largest motion is due to sP as it is represented in the three mantle arrivals. In this case it is almost certain that the sP phase near the 10 second time on the trace would be used in the magnitude calculation if the conventional procedure is used in the selection of the appropriate cycle of motion for an amplitude measurement. As a result the magnitude would be a measure of the S wave amplitude near 1 Hz. rather than the P wave amplitude.

As the event dimensions become larger, the measurement of magnitude in the conventional manner for shallow earthquakes results in a measurement of sP from a later arriving mantle phase, rather than from the first arriving mantle phase. Figure 26 shows the predicted signal train for a 20 km. event; and because of the longer periods and the strong overlap in time, none of the various individual phases are discernable, so that a magnitude would be calculated from the amplitude cycle near the 19 second point. This would result in a very much larger magnitude than that appropriate to the event, assuming of course that we wish to maintain a consistent magnitude measurement for all events regardless of rupture size.

65-A

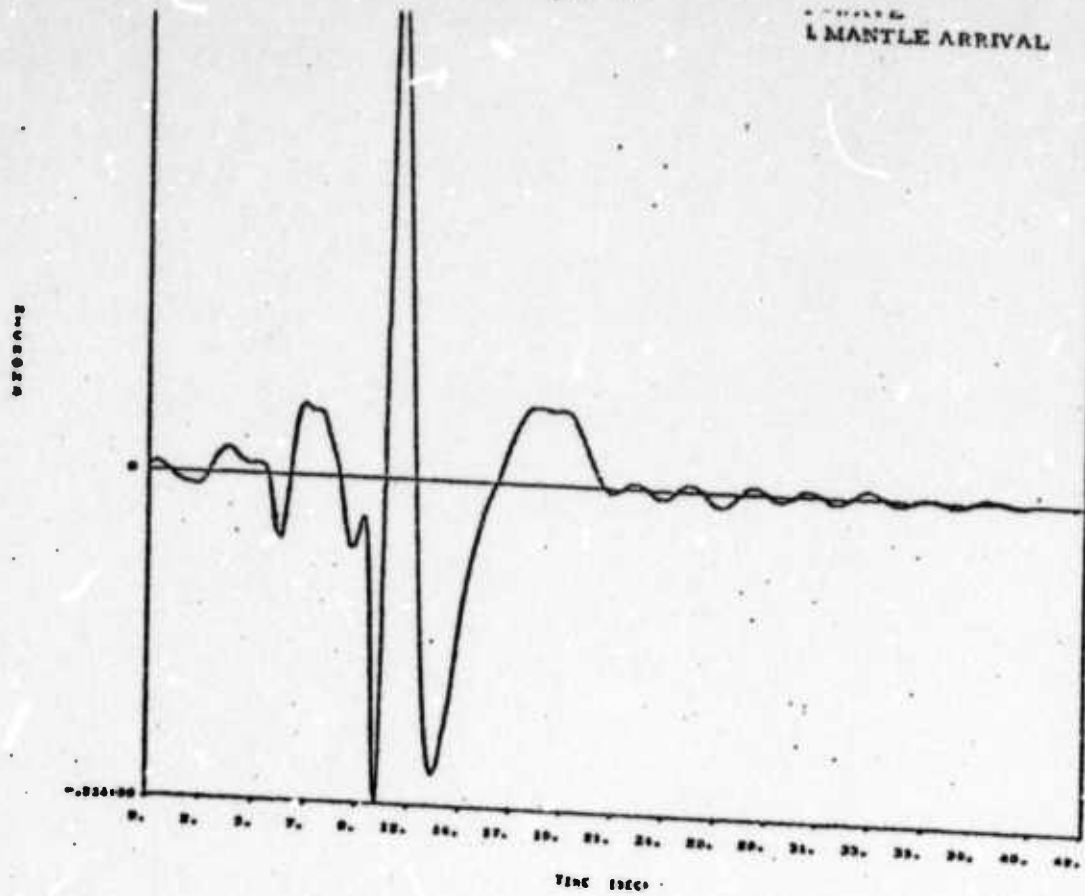
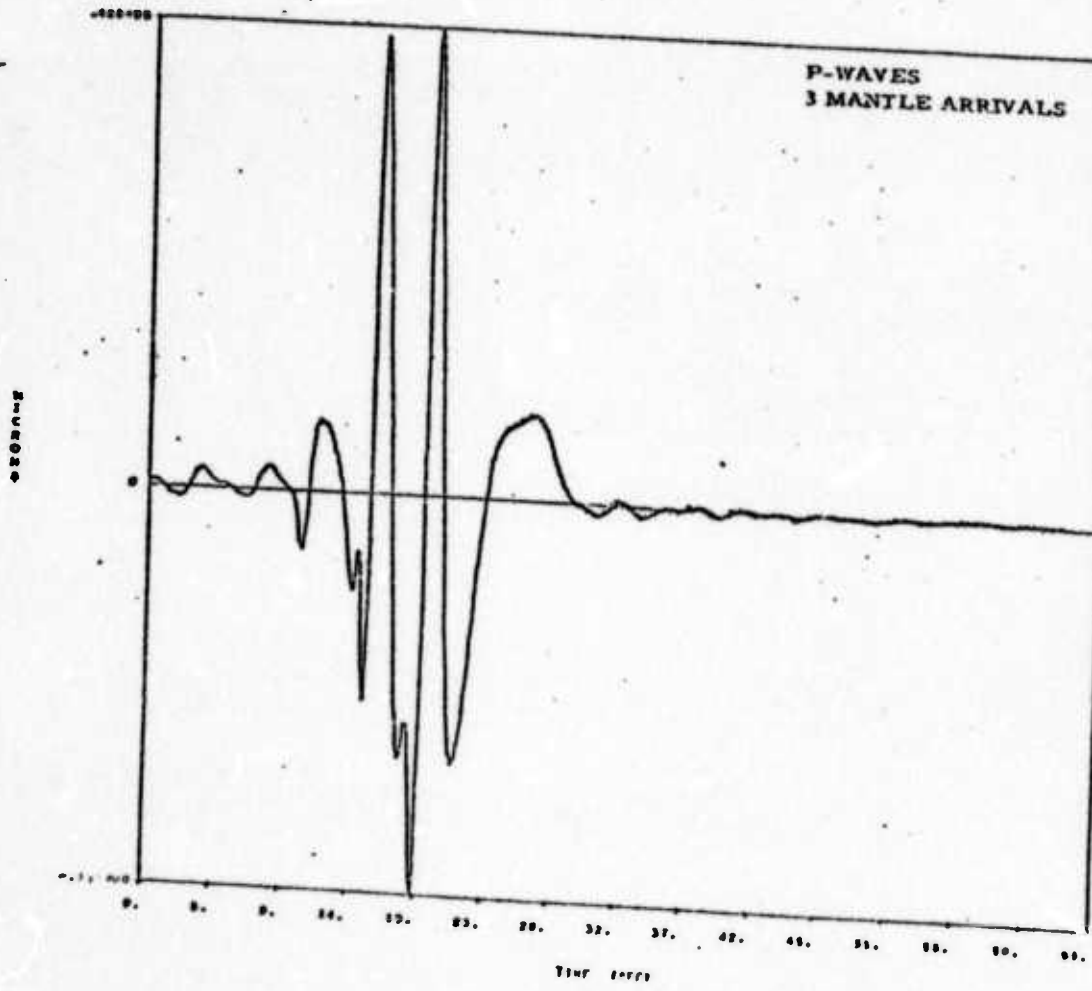
P-WAVES
3 MANTLE ARRIVALP-WAVES
3 MANTLE ARRIVALS

Figure 26. Theoretical earthquake ($L = 20$ km.) compressional wave train with same event parameters as in Figures 24 and 25. First arrival is at approximately 5.5 seconds in the upper figure and near 10. seconds in the lower figure. The amplitude prior to these times is noise arising in the Fourier transformation to the time domain. The signals are all rather long period and the various P

Thus we have seen that under even the best of conditions, that is without noise, the conventional magnitude measurement lacks consistency and thus for small events the magnitude is measured from the direct P wave from the event; for intermediate events the magnitude is probably measured from the sP phase of the first mantle arrival; and for large events (and at distances where later arriving mantle phases are present), it is very likely that the magnitude is measured from a superposition of later arriving sP pulses associated with later arriving mantle phases. If we add noise, then it becomes almost certain that this shift in measurement to an sP measurement will occur and that it will occur for even smaller events.

We must therefore keep two things in mind when we consider m_b data, first that such a shift is likely to have occurred for measurements involving shallow earthquakes and second that it is highly desirable that the m_b measurement be redefined in a much more precise fashion. This will be considered in the next section where we calculate m_b and M_S magnitudes from the theoretical seismograms and compare the results to observations.

Figure 27 shows the array of P wave signals from the five theoretical earthquakes that will be used throughout this study. We consider dip slip events and show here the signal forms for different fault lengths at a fixed prestress level, as they would be recorded by a short period LRSM seismometer. As we noted earlier, the entire

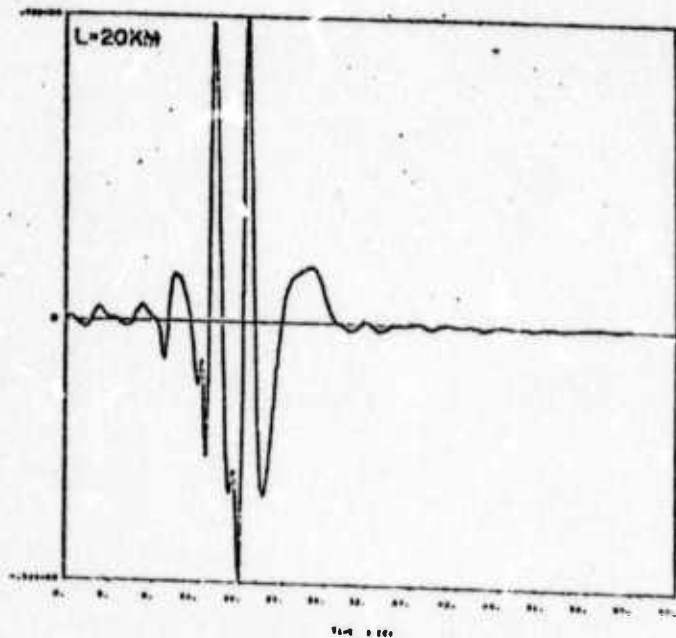
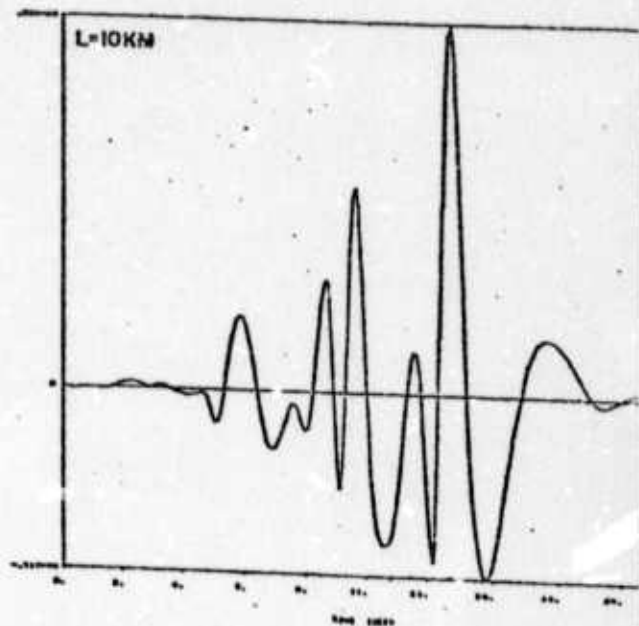
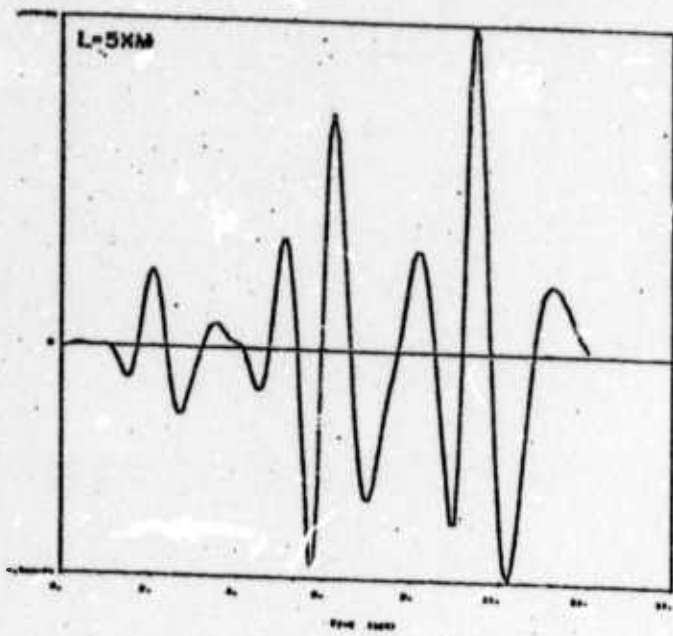
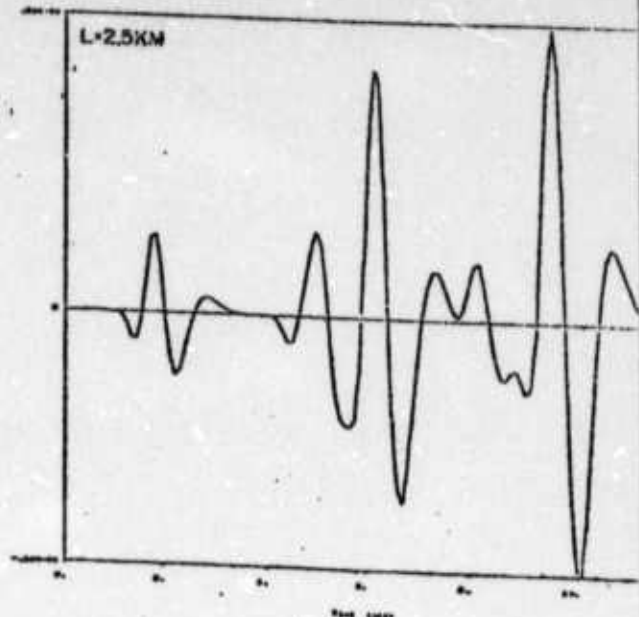
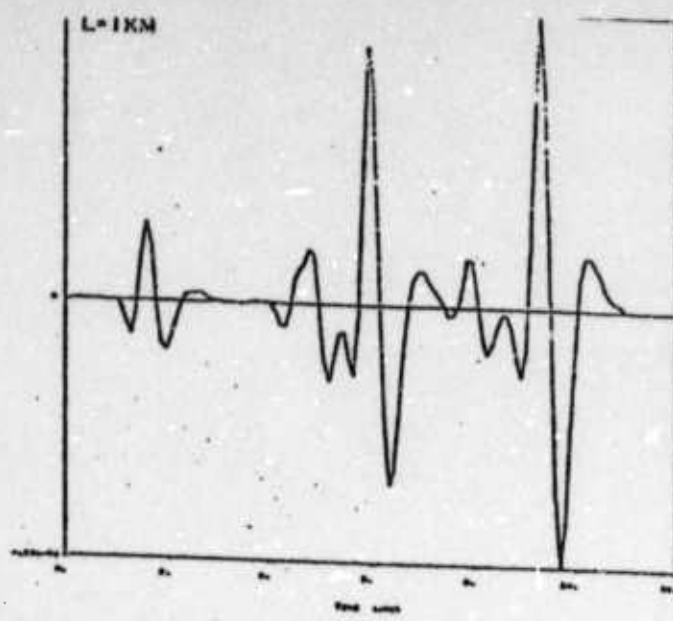


Figure 27. Theoretical P-wave signals from vertical "dip slip" earthquakes of various fault lengths. All signals are at 4000 km. and at an azimuth of 30°.

spectrum scales linearly with prestress level, so that changes in prestress result in a linear scale change for the amplitude of the time series shown here. For example, reducing the prestress from 500 bars to 250 bars results in the same wave form, but with the amplitude scale divided by two. Unfortunately changes in rupture velocity distort the amplitude and phase spectra in such a way as to require a complete recomputation of the theoretical seismogram. We will therefore treat the high rupture velocity case ($V_R = 2.4 \text{ km/sec.}$) as the case of greatest interest, since these events are most explosion-like and hence of greatest interest in this study. We then will simply infer the characteristics of the lower rupture velocity events from what we know of the spectral properties of these events, using the high rupture velocity time domain computations as a guide.

In addition to P waves, we will make use of the Rayleigh and Love type surface waves generated by these events in order to measure surface wave magnitudes. Figures 28 and 29 show the Rayleigh and Love waves from the earthquake set at a distance of 4000 km. and at an azimuth of 30° from the direction of the major axis of the failure zone.

The largest amplitudes of the surface wave trains are Airy phases that are typical of surface wave trains which have propagated over continental paths. The Airy phase part of the surface wave train is controlled by the velocity structure of the continental crust,

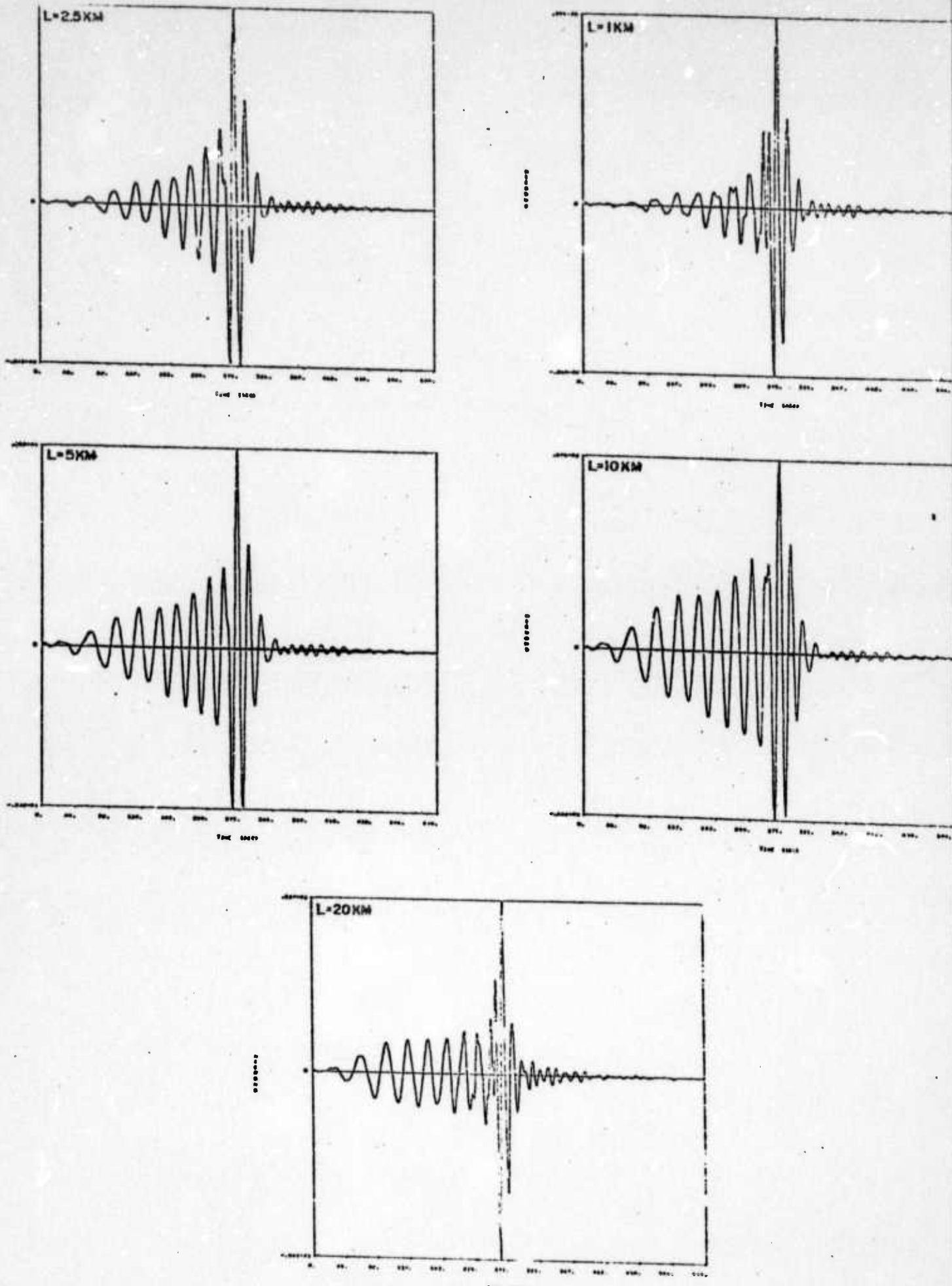


Figure 28. Theoretical Rayleigh wave signals. The events are the same as those of Figure 27 and at the same distance and azimuth.

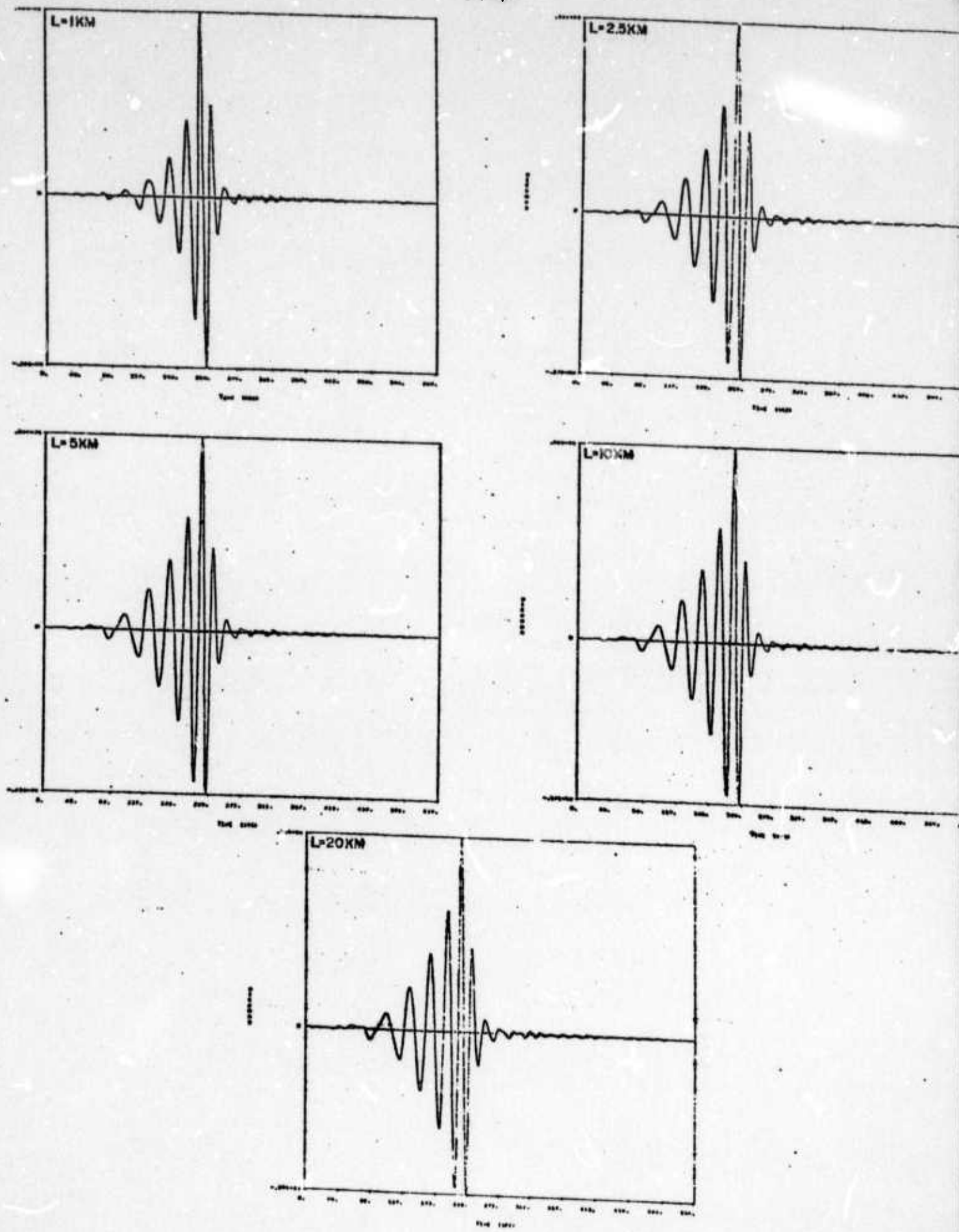


Figure 29. Theoretical Love wave signals. The events and distance and azimuth variables are the same as those on Figures 27 and 28.

and is particularly large. The CIT 109 structure was used in these computations, and we shall see later that this structure gives results in good agreement with observations. (See section III-b for example.)

The conventional surface wave magnitudes are calculated from the time domain signals by measuring the amplitude of that part of the wave train with period close to 20 seconds. The amplitude measured is then normalized by dividing by the effective period of the cycle where the amplitude measurement is made. Obviously, this can only be accomplished if the wave train is well dispersed, that is if the group velocity is a reasonably strong function of period and if the point of observation is sufficiently far from the source so that the wave train is well spread out in time. In the examples shown this is clearly the case. However, for small events or in cases of high noise relative to signal levels, it is often the case that the largest amplitude in the wave train is measured. The normalization procedure, consisting of division by the effective period of the wave train near where the amplitude measurement is made, is assumed to correct for the change from a measurement at 20 seconds period, and to yield a magnitude consistent with that which would be measured at 20 seconds. We see, however, from the examples of surface waves predicted for continental paths, that measuring the largest amplitude would result in a measurement of the Airy phase amplitude, with an effective period of 14 to 15 seconds. Thus the amplitude would be very

much larger than the 20 second amplitude, which occurs from 3 to 4 cycles earlier in the wave train, and the normalization procedure would result in an even larger value of the ratio A/T for the Airy phase than for this ratio for the 20 second period wave. This would then lead to a much larger M_S value using the Airy phase amplitude than if the 20 second amplitude were used. Because of the decrease of amplitude with event size, such measurements are common for small events, with a systematic switch to the 20 second measurement for larger events so that one can expect a systematic bias in M_S measurements. A similar observation was made by Evernden et al., 1971.

These variations in M_S measurement procedures lead to both scatter in the observed data and systematic bias. When coupled with the m_b measurement errors which lead to over estimates of m_b for large shallow events, since the amplitude of sP would usually be measured; one can expect certain systematic bias in $m_b - M_S$ data as well as considerable scatter.

In view of the importance of $m_b - M_S$ data for discrimination and as a potential data source which will allow us to determine regional tectonic characteristics (e.g., stress levels), we will consider m_b and M_S measurements from the theoretical signals and cover the entire range of measurement possibility, that is, we will measure amplitudes from the 20 second surface waves and from the Airy phase, for M_S , and from all three of the first three cycles of

the P wave train for m_b estimates. This will define a range of m_b and M_S values that could be observationally associated with a given event, and we will compare this range to the data for earthquakes.

(c.) $m_b - M_S$ predictions and observations

In view of the results of the previous section, it is imperative that we precisely define the m_b and M_S measurements that one can obtain within the rather loose prescription used in the measurement of magnitudes.

In the Appendix 1 we have reproduced the standard criteria as set forth under Project Vela for the measurement of signal amplitude and determination of body wave magnitude (e.g., see: Technical Report No. 63-122, Long Range Seismic Measurements Project 8.4, Fallon Earthquake, Geotechnical Corporation, Feb. 1964). In the example given the P_n body phase amplitude measurement is illustrated, the same procedure is applied to P phases at larger distances as well, when an event magnitude is to be calculated. We will follow the same procedure and use the same magnitude relation for the body wave magnitude, except that we will use m_b to denote body wave magnitude and define an m_b for each of the first three cycles of displacement. Thus referring to the figure for P_n in the Appendix 1, we will define $m_b^{(1)}$ as the magnitude computed from the amplitude measured from "b", $m_b^{(2)}$ as the magnitude measured using

the amplitude denoted as "c" and finally $m_b^{(3)}$ as the magnitude from "d". Obviously $m_b^{(3)}$ will correspond to the m_b defined by the procedure specified in the Appendix. As we will see, however, this results in the measurement of an sP amplitude for large shallow earthquakes and hence a large over-estimate of the true body (P) wave magnitude--in fact a magnitude measurement not related to the ordinary P wave magnitude, but actually an S wave magnitude.

Therefore, we define the body wave magnitudes $m_b^{(i)}$, $i = 1, 2, 3$ as:

$$m_b^{(i)} = \log_{10}(A_i / T_i) + b \quad (10.)$$

where the index i denotes the amplitude and period of the first, second or third cycle of motion. A_i is the zero to peak amplitude corrected for instrument response in millimicrons. The value of the constant b , the distance correction factor used in (10.), is the same as the constant (B) value listed in the Appendix 1. The period T_i should be "close" to 1 Hz.

The surface wave magnitude M_S is defined for all periods "near" 20 seconds by

$$M_S = \log_{10}(A/T) + 1.656 \log_{10} \Delta + 3.119 \quad (11.)$$

where Δ is the source to receiver distance in degrees (111.1 km./deg.) with $\Delta > 15^\circ$ required for applicability of this relation. Here A is

the zero to peak amplitude, measured in microns, of the wave train for the horizontal component of the fundamental mode Rayleigh wave with period T near 20 seconds. The amplitude A is to be corrected for the seismometer response at the period T .

Because we measure a surface wave magnitude for both Love and Rayleigh waves, we will denote the surface magnitudes as M_S^L and M_S^R respectively.

It is clear that all these magnitude definitions are frequency dependent. In particular, with regard to body wave magnitudes, we previously discussed the spectral shapes for P and S waves and showed that the spectral slope in the high frequency part of the earthquake spectrum is f^{-3} for events with normal rupture rates. For earthquakes with magnitudes above about 4.5, the body wave magnitude measurement is usually made in the high frequency spectral range of the event, since the effective period for the measurement is near 1 Hz and for events of this size and larger, the characteristic frequency f_C^H is less than 1 Hz. Because of the steep slope of the source spectrum in this frequency range however, relatively small changes in the effective period at which the measurement is made will result in significant changes in the magnitude obtained for the event. This is clearly seen if we observe that $A \propto T^3$, in the range $f > f_C^H$. Thus, $A/T \propto T^2$ and so $m_b \propto 2 \log_{10} T$. For the effective period ranging between 2 and .5 seconds, which is usual, this will result in

variations of m_b of roughly $\pm .5$ in magnitude, giving rise to a scatter in m_b about the mean, assumed measured at 1 Hz., of about one magnitude unit. In addition to the strong dependence of the source spectrum on frequency in the high frequency range, the attenuation of the field with propagation will provide an additional steepening of the high frequency slope, so that as observed at a distant point, the spectral amplitude will have a form more like $A \propto T^4$ in the high frequency range of measurement and hence $m_b \propto 3 \log_{10} T$ in this range. Thus, relatively small changes in the effective period at which the measurement is made can result in large magnitude changes.

While this effect probably gives rise to considerable scatter in m_b data, it also will bias the m_b measurements systematically, since the measurement is usually made at $T \lesssim 1$ Hz. for small events and $T \gtrsim 1$ Hz. for larger events. Thus the body wave magnitudes will be smaller for the small events and larger for the larger events, than what would be obtained if a 1 Hz. measurement could be made in all cases.

The magnitude results of the present section are obtained by measurements from theoretical time domain signals in the conventional manner; no attempt is made to apply any extra correction for a shift in the effective period of the wave amplitude measured away from 1 Hz., and the relation (10.) is used as it stands to calculate the $m_b^{(i)}$. This will allow us to compare the resulting m_b (and M_S) predictions

directly to observed data. In later sections we will reconsider the magnitude definitions in terms of ultra-narrow band filtered amplitudes at precisely 1 Hz. and .05 Hz., and provide a uniform definition of m_b and M_S at these frequencies, using the filter output amplitudes. However it is important to first examine the nature of the m_b and M_S predictions based on the standard magnitude definitions.

Figure 30 shows M_S^R as a function of m_b for the five standard dip-slip earthquakes previously discussed and illustrated in Figures 27-29. The m_b and M_S values are computed from the signals predicted at an azimuth of 30° and a distance of 4000 km. from the source. This azimuth and distance was chosen to be representative of the mean value that would be obtained from m_b and M_S measurements from a random distribution of teleseismic receivers ($\Delta > 2000$ km.). The azimuth choice (30°) is based on our knowledge of the radiation patterns for the events; and if the signal sampling obtained by a station network is reasonably well distributed over at least one full quadrant, then the 30° signal should be very close to the mean signal observed. Similarly 4000 km. is in most respects a representative distance for teleseismic signals, since the transfer functions for the body and surface waves are typical of those at teleseismic distances and approximate the mean values to be obtained. Further, the complexity of the P wave signal train is more

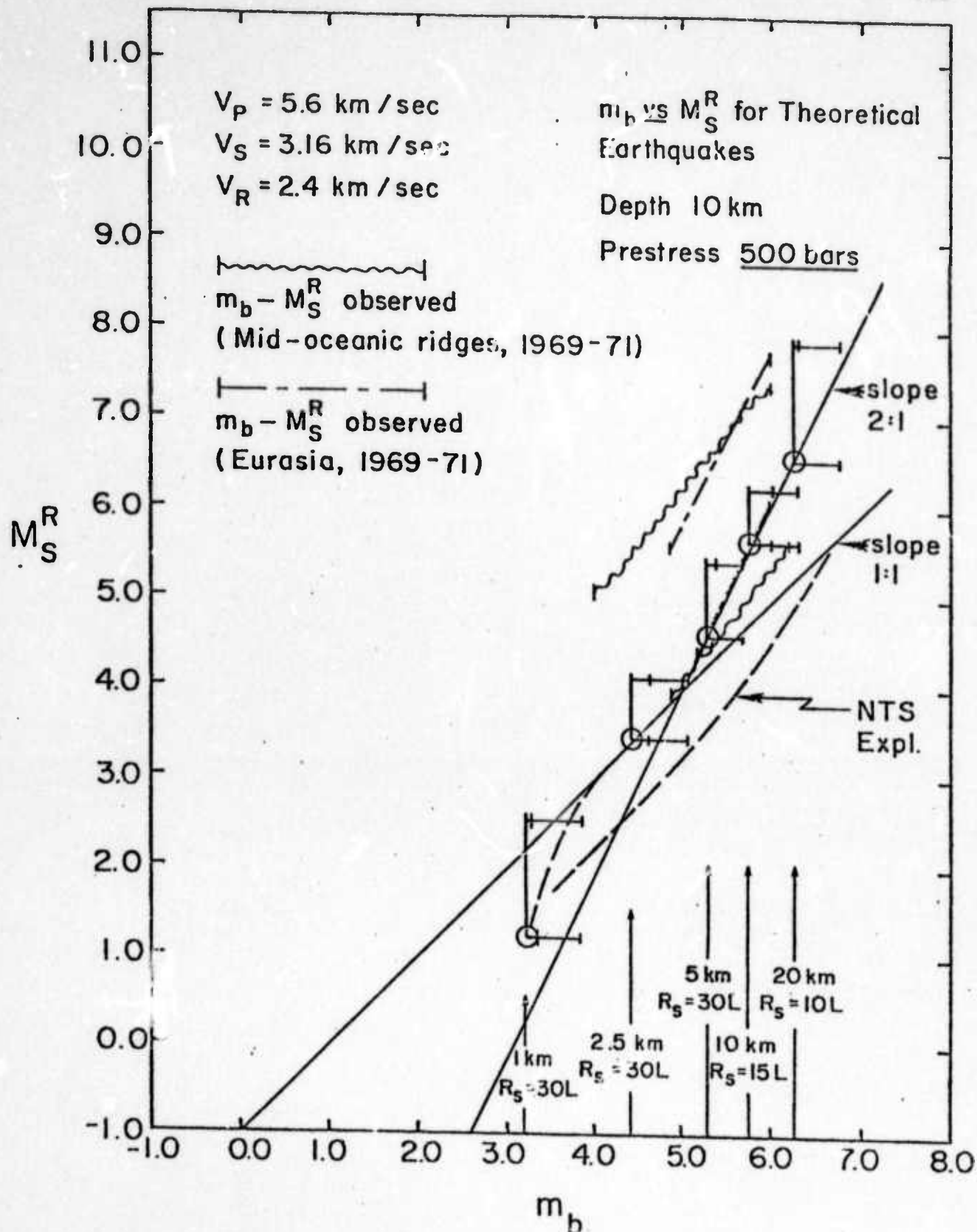


Figure 30. Rayleigh surface wave magnitude (M_s^R) as a function of body wave magnitude (m_b) for high stress drop, "dip slip" earthquakes. The theoretical results fit the high m_b bound of observed $m_b - M_s^R$ data for Eurasia. Shown for comparison is the observed mean $m_b - M_s^R$ curve (Continued on the following page)

Figure 30 (Continued).

for NTS explosions and the range of $m_b - M_s^R$ data for mid-oceanic ridge earthquakes. The circles denote $m_b^{(1)}$ magnitudes and M_s^R measured at 20 seconds. The horizontal line denotes the possible range of measurement of m_b . The upper theoretical bound for M_s^R , indicated by the vertical line from the $m_b^{(1)}$ value, is obtained by measuring the largest amplitude in the Rayleigh wave train in the 12 - 24 second range.

or less typical of that observed in the distance range $2000 < \Delta < 5000$ km., inasmuch as three "mantle phases" are present. At larger distances a single mantle phase would be observed, and the signal form would be somewhat simpler. However, the 2000 to 5000 km. range is most appropriately studied since our interest is in the entire range of event sizes, and small events can only be detected in this near teleseismic range. We also consider only "dip slip" events, that is events for which the stress field orientation is such that the displacement of the medium due to relaxation at the failure surface is downward on one side of the surface and upward on the other, as viewed relative to the earth's free surface. Clearly the excitation of surface waves, in particular, is affected by the choice of stress field orientation, but the effect is not large enough to change the results significantly from what would be obtained for some other stress orientation. This is particularly true because we sample the field at an azimuth such that we obtain an estimate of the mean signal level to be observed from many observations at different azimuths and so radiation pattern effects are "averaged out". This same rationale applies to the body wave signals from the dip-slip events used. Thus, without predicting signals for many kinds of events (varying stress field orientations), at many azimuths and distances, we can still obtain an accurate estimate of the average m_b and M_S values that would be obtained from a receiver network for a wide class of events. However, we have

computed the body wave radiation fields for events at a fixed depth of 10 km. so that the m_b values predicted are appropriate for shallow earthquakes in the 5 to 15 km. depth range. Events in this range are most important from the point of view of discrimination and also constitute the typical event for most tectonic regions outside regions behind oceanic trenches. The surface wave fields are computed using an effective source depth different from the 10 km. depth used for the body wave predictions, since the event failure zone dimensions are relatively large compared to the depth of the hypocenter, resulting in energy release from a large volume, clearly extending to the surface. Therefore the excitation functions (or transfer functions) for the surface waves were calculated using an effective point source depth of 1 km., where it was concluded that such a depth would give a reasonable approximation for surface wave excitation for such a shallow volume source.

The prestress level used in the calculations was 500 bars, and the $m_b - M_S^R$ curve defined by these events is seen to pass along the lower boundary line for the $m_b - M_S^R$ data for Eurasian earthquakes. This boundary line has the same slope in the $m_b - M_S^R$ plane as does the mean line through the data which is located, roughly, mid-way between the upper and lower boundary lines shown in the figure. The event rupture lengths are indicated along the m_b axis, along with the size of the stress zone characteristic dimension, R_S . Three $m_b^{(i)}$

magnitudes were computed, as previously defined, and the circles denote the $m_b^{(1)}$ value, while the horizontal bars extending to higher m_b values indicate the m_b value range, with the vertical tick marks indicating $m_b^{(2)}$, closest to $m_b^{(1)}$ in value, and $m_b^{(3)}$ which is the largest. In these computations for body wave magnitude $m_b^{(3)}$ was computed from sP or from a composite of this phase and P phases from later arriving mantle phases. For the smaller events with $L < 10$ km., $m_b^{(3)}$ was calculated from an amplitude of sP which was reasonably well separated from the first P phase (see Figure 27) and would not have been used as the "observed m_b ". However, for the two largest events it is possible that the $m_b^{(3)}$ value would be given as the observed body wave magnitude for the event, and for the $L = 20$ km. event, this is almost a certainty. This switch to $m_b^{(3)}$ occurs only for large shallow events, and for the predictions in Figure 30 the $m_b^{(2)}$ value would be assigned for all the small events even at the shallow depths used. The $m_b^{(2)}$ values do not differ much from $m_b^{(1)}$ values. Further we note that if the Eurasian events were reasonably deep, say 20 km. and deeper, then $m_b^{(1)}$ or $m_b^{(2)}$ values would be assigned to all events in the magnitude range shown since the large sP phase giving the $m_b^{(3)}$ value would be late enough in the signal train so as not to be used to determine the event m_b value. In view of the trend of the observed data from Eurasia, this would appear to be the case, that is the events were all probably deep enough so that

no confusion with sP occurred, and all quoted m_b values were $m_b^{(1)}$ or $m_b^{(2)}$ values measured from the direct P wave.

On the other hand the observed data from the mid-oceanic ridges shows a distribution that suggests that these events were of a different character than those from Eurasia. In particular, it is quite possible that many of the events were shallow, in the depth range 5-15 km., and that the sP phase was used rather than P for the magnitude calculations. This would have the effect of biasing the body wave magnitudes toward larger m_b values for the larger events and hence rotating the $m_b - M_S$ population in the $m_b - M_S$ plane to a distribution having bounding lines and a mean line with lower slope, just as is the case for the mid-oceanic ridge data. In this case the selection of the $m_b^{(3)}$ theoretical values may be appropriate for the larger events, in which case the theoretical $m_b - M_S$ line calculated for 500 bar prestress events would provide a fit to the mid-oceanic data as well as to the Eurasian data.

On the other hand an alternative explanation of the mid-oceanic $m_b - M_S$ data is perhaps equally likely. If we refer back to Figure 9, which shows the logarithm of the S wave source spectrum, where M_S^R is proportional to this quantity, plotted as a function of the logarithm of the P wave source spectrum, where m_b is proportional to this later quantity, we see that there are large differences between loci for different R_S and V_R values in the region in which the loci change

slope from near unity to infinity. In particular, if we were to choose a uniformly larger value of R_S for all the theoretical events calculated, we would obtain a theoretical $m_b - M_S$ curve having lower slope in the magnitude range $4.5 < m_b < 6.0$ than the theoretical loci shown in Figure 30. This is exemplified in Figure 9 by the difference in the curve denoted by $R_S^{(2)}$ as compared to the curve denoted $R_S^{(1)}$, in the case when $V_R = V_R^{(3)}$ for both. The range of observations delineated in Figure 30 are also indicated in Figure 9 as lying to the right of the dotted line at $\log A_p = 0$.

Therefore we see that the lower bound line for mid-oceanic ridge data can probably be fit, as it stands, using theoretical events with larger R_S values than those used in the calculations shown in Figure 30; that is with values of the order of 500 km. as compared to the values of around 150 km. used in the current calculations, and with a slight increase of rupture velocity and reduction in the prestress from 500 bars. This interpretation suggests then that the ridge events occurred in a region that was stressed fairly uniformly over a rather broad region of dimensions quite large compared to the maximum dimensions of the events occurring within the tectonic zone. The fact that the upper bound line on the ridge data has the same slope as the lower bound line suggests that all the events occurred in a similar tectonic setting, that is in a broad uniformly stressed region, with large effective R_S near 500 km., and that the events differed only in

the stress drop associated with the individual failure events making up the population. By the same line of reasoning the Eurasian data would require a series of variable stress drop events occurring in a tectonic region in which the characteristic dimension of the stressed zones within which the individual events occurred were relatively smaller (near 150 km.) than that to be associated with the mid-oceanic ridge events. Then, as with the ridge data, the upper and lower bounding lines of the event population would be explained in terms of low stress drop events (upper bound) and high stress drop events (lower bound) occurring in a similar tectonic (prestress) setting and all having similar rupture velocity and depth values. Further, on the basis of the theoretical model used, we could draw the inference that the lower bound lines of the populations define the actual prestress of the tectonic region, and by a fit to this boundary line the ambient prestress level would be determined. All other events lying between the population bounds would then be interpreted in terms of the effective elastic properties in the rupture zone required to provide a fit to the observed $m_b - M_S$ values for this ambient prestress level. This would allow us to investigate the nature of the failure process and go beyond the over-simplified concept of a "stress drop" on the failure surface.

There are, of course, alternative explanations of the data in terms of theoretical fits to the populations, involving combinations of

variable prestress (or stress drop) stress zone characteristic dimension, R_S , and rupture velocity for a given population. Before we can assess which of the previous two possibilities is appropriate or whether some other combination of parameter variations and measurement "variations" best describes an event population from a given tectonic region, it is clear that the population must be defined in more detail than is the case for the data shown. In particular, isolation of populations based on depth and "fault plane solutions" involving failure zone orientation and prestress field orientation as well as on the basis of tectonic province, would provide a much "cleaner" data set, with the result that ambiguities in interpretation could practically be eliminated and a considerably more confident theoretical explanation of the $m_b - M_S$ data obtained. The benefits of data pertaining into populations of this type are considerable from several points of view; first we would acquire a much more confident and detailed understanding of $m_b - M_S$ data and a basis for extrapolation designed to delineate the extreme limits of such data for earthquakes; second, we could determine ambient stress fields in the earth as a function of tectonic province and depth and finally we could determine rupture velocities, event dimensions and effective elastic properties of the material in the failure zone and so acquire some insight into the mechanics of the failure processes at different points in the earth.

While it is clear that the $m_b - M_S$ data bounds shown in Figure 30 do not allow us to draw totally unambiguous conclusions regarding prestress levels, stress zone dimensions and other source parameters, it is nevertheless the case that we can fit the observed data remarkably well by using a reasonable set of event parameters. Furthermore, if we adopt the reasonable hypothesis that the event populations are distributed in the $m_b - M_S$ plane between the bounds indicated because of a variation in the stress drop among the events, then we can change the prestress level used for the theoretical calculations and simulate the lower stress drop events.

Figure 31 shows the result of reducing the prestress to a level required to fit the mean of the $m_b - M_S$ data for Eurasia. The mean $m_b - M_S$ line for this data is actually somewhat closer to the lower boundary line than to the upper bound and is almost exactly along the slope 2 line drawn through the theoretical points in Figure 31. The prestress level required is 100 bars, and this is to be interpreted, along the lines previously discussed, as the difference between the stress level within the rupture zone and the prestress level in the surrounding medium. In terms of the theoretical model used in this study, this means that the effective rigidity within the failure zone had some non-zero value at all times. If we consider the events defining the lower bound of the event population as representing cases in which the rigidity vanished in the transient sense stipulated by the

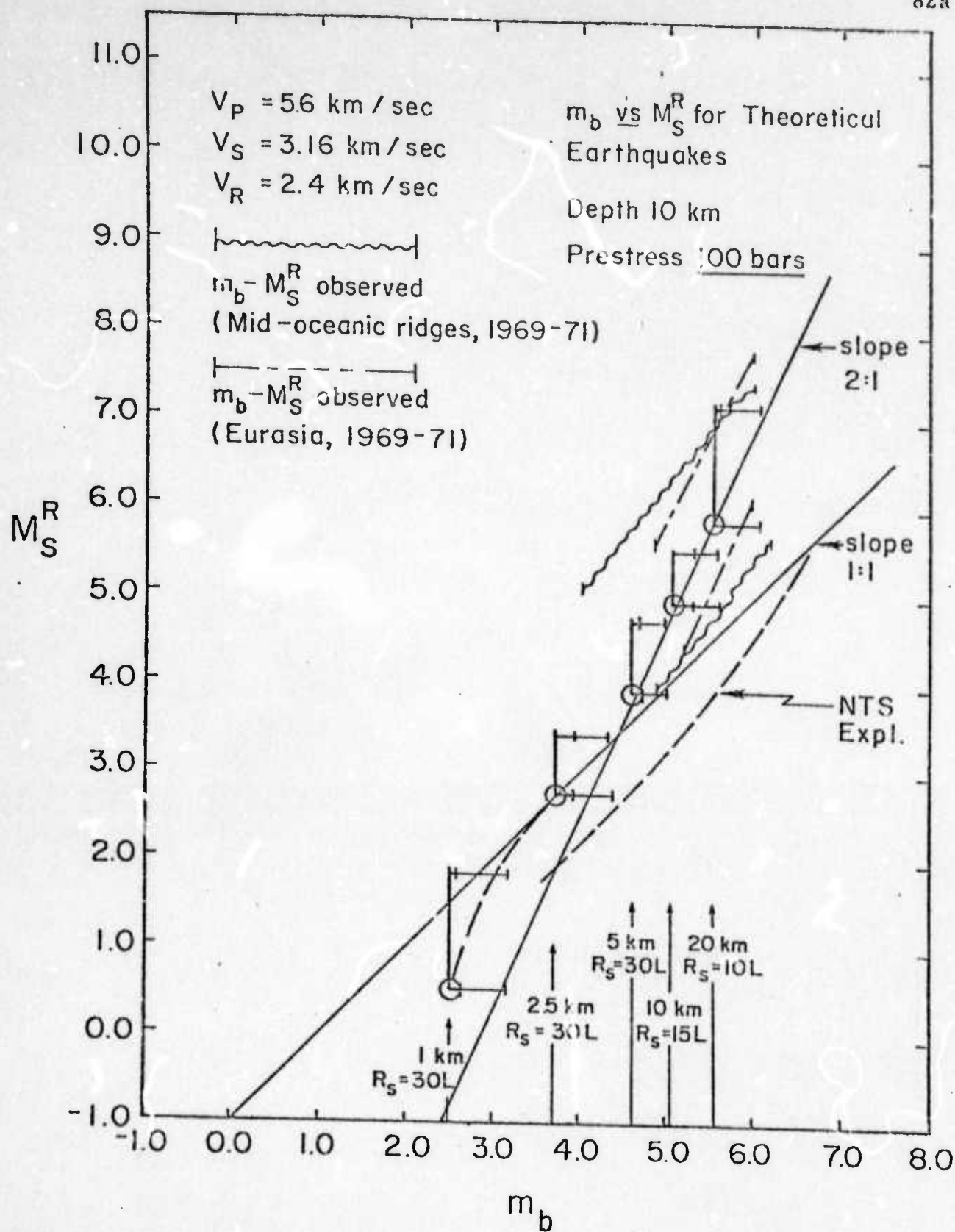


Figure 31. Rayleigh surface wave magnitude as a function of body wave magnitude for intermediate level stress drop, "dip slip" earthquakes. The theoretical $m_b - M_s^R$ curve lines on the approximate mean curve of the observed $m_b - M_s^R$ data for Eurasia. Note that the slope 2 line (Continued on the following page)

Figure 31 (Continued).

has a different intercept here than in Figure 30. The theoretical results follow a slope 2 curve at high magnitude and cross over to a slope 1 curve near $m_b = 4.5$. The $L = 1 \text{ km.}$ event falls off the slope 1 line (note dotted line) because R_s is taken less than the wave length of the 20 second Rayleigh wave, resulting in a reduction of M_s^R .

model we have used (e.g., melting followed by locking), then 500 bars represents the ambient stress field for the event population and a 100 bar "prestress" represents a rigidity drop to 1/5 the value of the initial rigidity within the failure zone. Under this interpretation then, most earthquakes involve a transient reduction in material cohesion such that the effective rigidity of the material in failure is about 20% of its normal value.

Figure 32 shows the theoretical event loci in the $m_b - M_S$ plane for a "prestress" of 10 bars and while we have not calculated m_b and M_S values for events larger than $L = 20$ km., it is clear that the theoretical curve lies along the slope 2 line in the magnitude range of the observations and that 10 bar stress drop events fit the upper bound to the Eurasian events. Therefore we can fit the range of the observations using events with "prestress" levels varying between 10 and 500 bars and fit the mean of the event population with 100 bar prestress events. Clearly the low stress drop events observed have large rupture dimensions, much larger than the 20 km. maximum we have used in our computations. If we use the scaling laws discussed earlier, in particular that the amplitude scales with the cube of the rupture length, then we would need a 200 km. failure dimension in order to fit the largest M_S^R value observed for Eurasia, assuming that the M_S^R was measured at 20 seconds for these events.

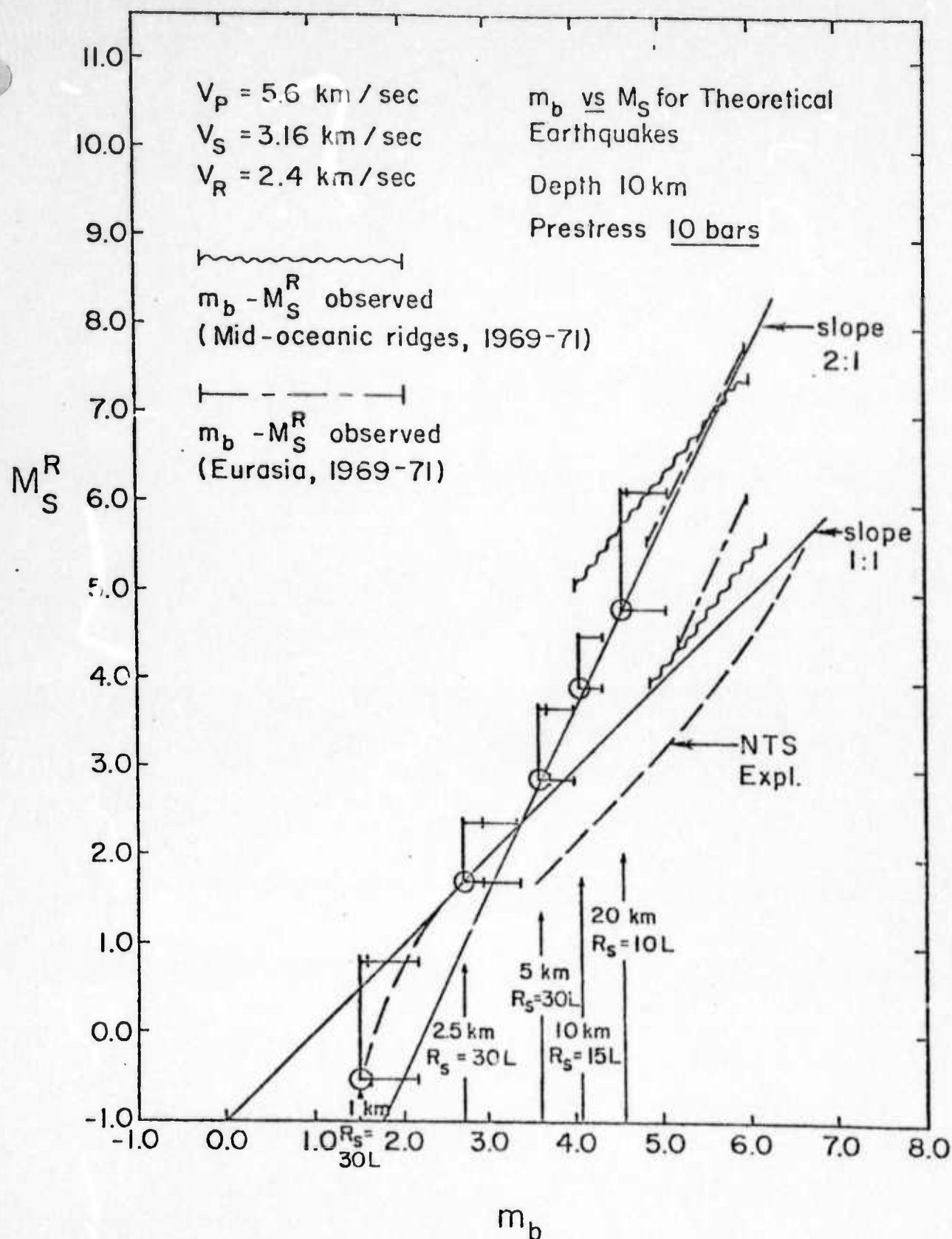


Figure 32. Rayleigh surface wave magnitude as a function of body wave magnitude for low stress drop, "dip slip" earthquakes. The theoretical $m_b - M_s^R$ curve fits the upper M_s^R bound for events in Eurasia. As in Figures 30 and 31, the fault lengths (L) used are indicated at the bottom of the figure along with the R_s value used in the computations. Only the M_s^R for the 1 km. fault is strongly affected by the R_s choice, the R_s values for the other earthquakes are all large compared to the wavelength of the 20 sec.

We observe that the M_S^R value can vary by over one magnitude unit depending on whether the 20 second period signal amplitude is measured or whether the measurement is made at some other point in the signal train at a somewhat different effective period. The large M_S^R range indicated in the Figures 30-32 is due primarily to the large continental Airy phase, for oceanic structure the variation in amplitude with period in the surface wave train is smaller and the possible M_S^R range therefore smaller. However, since many observations are made using stations well within continents, such stations could give the large M_S^R variation, thereby possibly strongly influencing the mean M_S^R measured. Observationally the measurement of the 20 second amplitude is strongly adhered to whenever possible. Thus it is unlikely that a significant number of the large magnitude events have M_S^R values corresponding to measurement of an Airy phase. Hence we expect the M_S^R values for large events to be very close to the 20 second M_S^R . For small events, however, the 20 second level surface wave amplitude may be very low, and it is probably that the signal amplitude is often measured at shorter period and not infrequently that the Airy phase amplitude is used. Thus we would expect a bias in the data such that the measured M_S^R values for small events would be too high relative to the M_S^R values for larger events. In particular, it is possible that some of the mid-oceanic ridge data reflect this and that the low magnitude end of the

upper bound line for this data has M_S^R too large because an Airy phase was measured. Thus we could argue that the ridge data has M_S^R too high at the low m_b end of the upper bound line, and correcting the data would result in rotating the line down, with the high m_b end fixed, conceivably to a position the same as that for the Eurasian data line. At the same time we could invoke the argument that the m_b values for the large ridge events are too large because an sP phase was measured for a significant number of the events, in particular for events defining the high m_b limits of the population. Correcting the data would then result in a new lower boundary line, in effect a rotation of the present line with the low m_b end fixed to a position close to the position of the Eurasian data line. Thus the two corrections, if appropriate, could result in an event population almost identical with the Eurasian population. In this case the theoretical fit to the Eurasian data would also apply to the ridge data. In order to evaluate this possibility, it would be necessary to check the "critical" events having listed M_S^R values near 5 and with very high listed m_b values and also those with very low m_b values.

On the other hand, the data sets for both populations probably contain some deep events, and our theoretical m_b and M_S^R calculations are for shallow events. Hence if most of the large m_b events in the ridge event-population were deep, then their M_S^R values would be less than those for shallow events; and the trend of the

population would have a lower slope in the $m_b - M_S^R$ plane than is the case for shallow events. In this case, of course, our present theoretical calculations do not apply, and we would have to make similar calculations for deep events for comparisons with the data. Detailed checking of the population for event depths would, of course, answer this question.

If we take the data at face value however, assuming that only a very few events within the populations were affected by sP or Airy phase measurements and that most events were fairly shallow, then we can fit the mid-oceanic ridge data by increasing the R_S values used for all the theoretical calculations, as we previously observed. This implies a prestress zone of characteristic dimension near 500 km. for the ridge events, while it is near 200 km. for the Eurasian events. However, the prestress levels for the ridge events would be lower than for the Eurasian events.

There are several features of the theoretical results that are particularly important for the discrimination of underground explosions from earthquakes using $m_b - M_S$ criteria. In all the Figures 30-32, we have indicated the mean $m_b - M_S$ curve for underground explosions at the Nevada Test Site (NTS). This line is outside the earthquake population limits for both populations shown. The mid-oceanic ridge population is of the same character as the worldwide earthquake population, and therefore the NTS line lies

outside all earthquake populations in the magnitude range shown. However, the NTS data and data from explosions at other sites scatter about this mean line, and the band width is such that the upper bound of the total explosion population essentially coincides with the lower bound of the mid-oceanic ridge data. Therefore, there are a few earthquakes that have $m_b - M_S$ values about the same as those for observed explosions with high M_S^R values. We have shown in fact that shallow dip-slip earthquakes with 500 bar prestress (or stress drop) levels and moderately high rupture velocities lie along this boundary line. Further, decreasing the R_S values from those used here and/or increasing the rupture velocities would have the effect of shifting the lower bound of the theoretical earthquake population toward the explosion data. (See figure 9 as a guide to the variation of $m_b - M_S$ lines with parameter changes.) It would appear, however, that in terms of the earthquake model used here at least, the highest prestress levels to be encountered are near 500 bars and that the prestress region and rupture velocity limits for earthquakes are about of the order used in the calculations, at least for events in the magnitude ranges covered by the observations. Thus the 500 bar prestress events of Figure 30 are the most explosion-like earthquakes from Eurasia. Theoretical events with somewhat larger R_S values and lower prestress and/or higher rupture velocities would provide the lower bound to the mid-oceanic ridge data and hence be the most

explosion-like events from this population. The differences between the stress levels, R_S values and rupture velocities would not be large for the two data sets, and the extreme events for Eurasia provide a reasonable indication of the values of the parameters for the most explosion-like earthquakes to be encountered.

Adopting these events as the critical earthquakes to be studied from the point of view of discrimination, we see from Figure 30 that the locus of $m_b - M_S$ values traced out in the $m_b - M_S$ plane, by varying the rupture dimensions of this class of earthquakes, has a slope of 2 for large events. At around $m_b = 5.0$ the event curve assumes a slope close to one. This break in slope is actually gradual and is explained in terms of the slope changes shown in Figure 9. In particular, for events of this type with rupture dimensions less than about 4 km., both the m_b and M_S measurements are made in the low or intermediate frequency range of the events. For events of larger size, the m_b measurement (at 1 Hz) is made in the high frequency range of the event spectrum while the M_S measurement is still made in the low or intermediate frequency range. We note also that Figure 9 predicts a continual increase in the $m_b - M_S$ line slope as the event dimensions increase until the line is vertical. The cutoff m_b value is not reached in the $m_b - M_S$ plots of Figures 30-32 because the measurement is in the time domain, and, as indicated earlier, the effective periods measured for the larger events were

somewhat larger than 1 second. This has the effect of increasing the m_b value over what it would be if measured at 1 second and "postponing" the steeping effect and eventual cutoff on m_b . If the measurement is never made at an effective period larger than say 2 seconds, whatever the size of the event, then eventually the curve would become vertical.

In any case we see that the spectral shape of the earthquake radiation field is reflected in the $m_b - M_S$ data by changes of slope in the $m_b - M_S$ loci for a given class of event. We see that the predicted slope change is important to the discrimination problem at low event magnitudes since if the earthquake curve continued with a slope of 2 to low magnitudes, it would intersect the mean curve for the explosions at about $m_b = 4.5$. In this case the earthquake and explosion populations would begin to overlap at $m_b \approx 5$. and be hopelessly entangled for magnitudes less than $m_b = 4.5$, making discrimination of explosions from earthquakes using $m_b - M_S$ data practically impossible.

However, if the stress zone dimensions remain fixed for all events, then we see from Figure 9 that once the unit slope is attained in the $m_b - M_S$ plane, then all smaller events will remain on this line. For the critical earthquake line defined by the Eurasian data we see that the separation of the NTS line and the line of unit slope through the theoretical events is about one magnitude unit; and if the

R_S value were always reasonably large compared to the wave length of the 20 second Rayleigh wave ($\lambda \sim 50$ km.) and fixed, then we would expect this separation to be maintained for all magnitudes.

However in the calculations we have reduced the value of R_S for the 1 km. event to a value less than the critical 20 second wave length. This strongly reduces the long period spectral level for the event and hence reduces the M_S value without changing the m_b value. The $m_b - M_S$ point for this event therefore falls below the slope 1 line.

This departure from the R_S value indicated by the Eurasian data ($R_S \sim 150-200$ km.) is conceivable on physical grounds since the dimensions of the high stressed zone may be the factor that limits the spatial extent of the failure zone growth, at least in some cases. (The event rupture length may of course be limited by the strength of the material, so that it stops when a particularly strong inhomogeneity is encountered at the rupture front.) If this is the case for some events, then some small events would occur in prestress zones of rather small dimensions, being limited in size by the spatial extent of the stress concentration, and constitute small volume radiators, quite inefficient in the radiation of waves with wavelengths larger than the volume source dimension. Such events would clearly begin to "look" like explosions in terms of their effective size, and as we can see from Figure 30, the 1 km. event would have m_b and M_S values within the explosion population.

The R_S value for the 1 km. event was purposely chosen to be very small, to illustrate the effect of R_S on the discrimination problem at low magnitudes. However, the $m_b - M_S$ data shown include events with apparent dimensions as small as 5 km., and for these small events there appears to be no departure from the large R_S value of from 150 to 200 km. required to fit all the data, so that there is no obvious evidence in the observed data that R_S decreases with decreasing failure zone dimensions (or, more properly, that L values decrease because of decreasing R_S). However the mid-oceanic data appear to require a larger stress zone dimension (among other parameter variations), and so it appears that R_S can vary from one tectonic region to another; and this is hardly surprising. However this does not show that R_S can be very small. The one strong suggestion that the effective prestress concentration dimension can be very small is the spectral data shown in Figure 15. In that case we used an R_S of 14 km. to fit the data. The fit obtained was considered to be good, but the constraint imposed on the R_S value is rather weak because of the low frequency "noise" level--that is the uncertainty associated with the low frequency spectral estimate. As we have seen, the low frequency far field component of the spectrum decreases as f^2 , for $f < (R_S/V_S)^{-1} \ll 1$, and gives the far field spectrum a peaked shape while the near field component of the spectrum behaves like $1/f$ for $f \ll 1$, so that the composite

spectrum will typically have a minimum in the low frequency range followed by a $1/f$ increase at very low frequency. Spectra obtained by Johnson and McEvilly (1974) for numerous earthquakes in the Bear Valley area of California, with the data of Figure 15 being one example, typically show such a long period minimum in the range .1 to .05 Hz., implying that at least some small earthquakes with rupture zone dimensions in the range 1-2 km. have associated small R_S values, of the order of 10 to 20 km.

We note that the R_S value is critical to the determination of the $m_b - M_S$ loci for low magnitude earthquakes, in particular we note from Figures 30-32 that all the slope 1 lines through the theoretical events have the same m_b and M_S intercepts regardless of the prestress levels used for the events. This is because the scaling for changes of prestress in this low magnitude range changes both the m_b and M_S values by the same amounts, and so earthquake $m_b - M_S$ points simply "slide" along the unit slope line for changes in prestress. Further we see from Figure 9 that variations in rupture velocity do not change the loci of low magnitude events in the $m_b - M_S$ very strongly, and at low enough magnitudes, not at all. Thus any spread in earthquake in $m_b - M_S$ data at low magnitudes would be due, almost entirely, to variations in R_S for the events.

III. Conclusions

We draw the following conclusions from the results discussed:

- (1) The representation of an earthquake using relatively rough first order models in a relaxation source theory yields seismic field predictions that are in good agreement with observations and with fairly elaborate numerical models.
- (2) Predictions of $m_b - M_s$ data for earthquakes as a function of source parameters (prestress level and spatial extent, rupture velocity, source dimension, etc.) provides an acceptable explanation for the scatter in observed $m_b - M_s$ data for earthquakes as well as a fit to the mean of the observed earthquake data and hence a basic understanding of this data in terms of source characteristics as represented by the set of source parameters, which includes pre-stress magnitude and its spatial variation or extent. It is evident that these results are important to the problem of earthquake - explosion discrimination.
- (3) Observed $m_b - M_s$ data can be used to obtain confident estimates of stress drop, pre-stress zone dimensions, rupture velocity and failure zone dimensions. Using selections of $m_b - M_s$ data based on earthquake type and seismic zone (defining an event class) it is possible to map ambient stress levels, by determining the pre-stress level required to fit the high m_b bound on the distribution of $m_b - M_s$ values observed for the event class; under the reasonable assumption that the highest m_b valued events of the class (which require the

highest stress levels) involve a total loss of cohesion (vanishing of the effective rigidity within the failure zone), at least in the transient sense described by the current model. The other events of the class can then be interpreted in terms of a partial loss of material cohesion (a finite effective rigidity) under the action of the ambient stress field determined by the highest m_b valued events of the class, and in this fashion an estimate of the rheological properties of the failed material can be obtained.

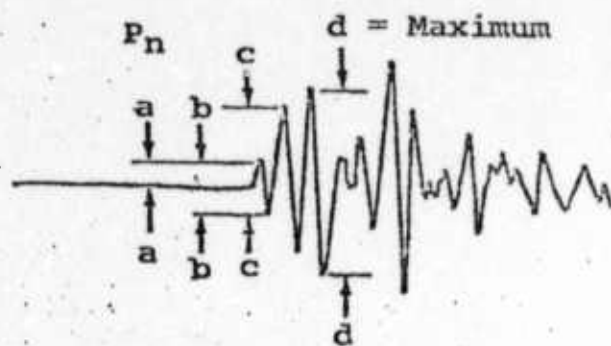
(4) An estimate of the high stress zone characteristic dimension (R_s) can be obtained from the character of the $m_b - M_s$ population distribution for a class of events in a given tectonic zone. This estimate can be improved by using a more general prestress condition than that employed in the present study (uniform prestress) and by dropping the imposed condition that the volume relaxation have a sharp cut-off at a distance R_s from the failure zone. This generalization can be effected in practice through the use of a numerical technique for the calculation of the equilibrium field around an inclusion (the failure zone) in a nonhomogeneously prestressed, layered medium; this calculation being all that is required to establish the initial value field for the dynamical relaxation source calculation which is then accomplished analytically by our current methods.

IV. Acknowledgements

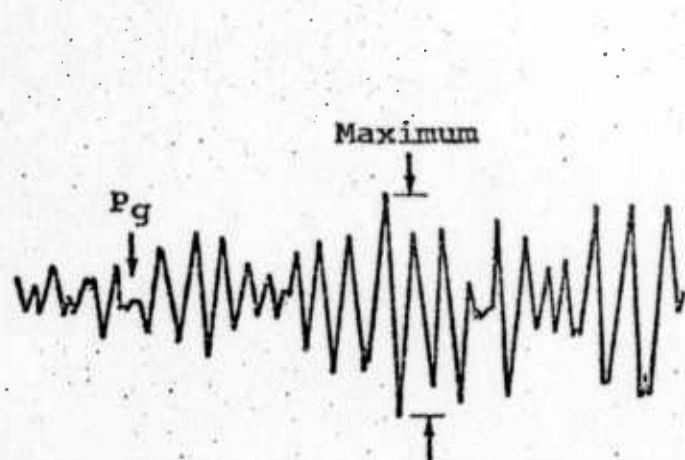
Some of the material in this report was generated from past contract work supported by ARPA and monitored by AFOSR. In particular results from work under contracts F 44620-72-C-0078 and F 44620-72-C-0023 at the California Institute of Technology. This work was done while the author of this report was at Cal. Tech. and, in part, while at Cires. The material is included here in an effort to provide a complete and comprehensive discussion. The detailed study of the m_b - M_s variations for theoretical earthquakes and their comparisons with observed data was, however, largely accomplished under the present contract.

Appendix I
Body Wave Magnitude Definition and Distance Correction Factors

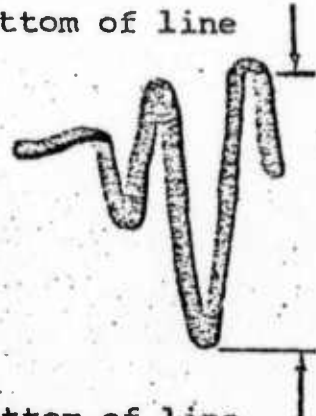
96



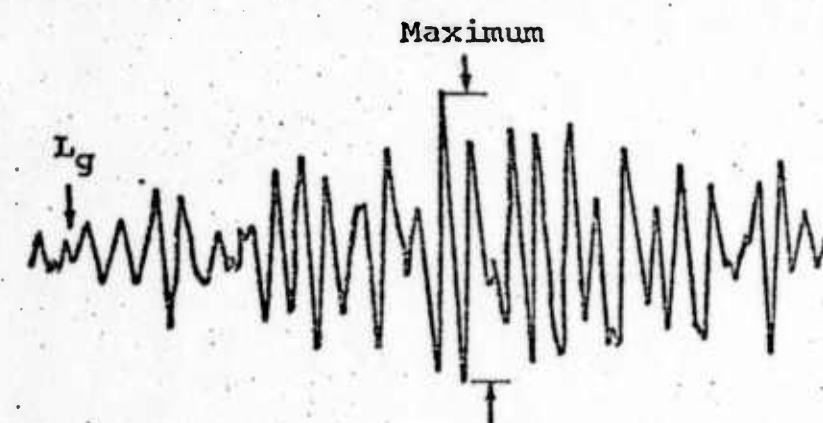
Reproduced from
best available copy.



Bottom of line



Detail Showing Allowance
For Line Width



Pick time of Pn at beginning of "a" half cycle.

Pick amplitude of Pn as maximum " $d/2$ " within 2 or 3 cycles of "c".

Pick amplitudes of Pg and Lg at maximum of corresponding motion.

Unified Magnitude: $m = \log_{10} (A/T) + B$

where

$A = \text{zero to peak ground motion in millimicrons}$
 $= \frac{\text{mm}}{1000}$

K

T = signal period in seconds

B = distance factor (see Table below)

mm = record amplitude in millimeters zero to peak

K = magnification in thousands at signal frequency

Table of Distance Factors (B) for Zero Depth

Dist (deg)	B	Dist (deg)	B	Dist (deg)	B	Dist (deg)	B
0°	-	27°	3.5	54°	3.8	80°	3.7
1	-	28	3.6	55	3.8	81	3.8
2	2.2	29	3.6	56	3.8	82	3.9
3	2.7	30	3.6	57	3.8	83	4.0
4	3.1	31	3.7	58	3.8	84	4.0
5	3.4	32	3.7	59	3.8	85	4.0
6	3.6	33	3.7	60	3.8	86	3.9
7	3.8	34	3.7	61	3.9	87	4.0
8	4.0	35	3.7	62	4.0	88	4.1
9	4.2	36	3.6	63	3.9	89	4.0
10	4.3	37	3.5	64	4.0	90	4.0
11	4.2	38	3.5	65	4.0	91	4.1
12	4.1	39	3.4	66	4.0	92	4.1
13	4.0	40	3.4	67	4.0	93	4.2
14	3.6	41	3.5	68	4.0	94	4.1
15	3.3	42	3.5	69	4.0	95	4.2
16	2.9	43	3.5	70	3.9	96	4.3
17	2.9	44	3.5	71	3.9	97	4.4
18	2.9	45	3.7	72	3.9	98	4.5
19	3.0	46	3.8	73	3.9	99	4.5
20	3.0	47	3.9	74	3.8	100	4.4
21	3.1	48	3.9	75	3.8	101	4.3
22	3.2	49	3.8	76	3.9	102	4.4
23	3.3	50	3.7	77	3.9	103	4.5
24	3.3	51	3.7	78	3.9	104	4.6
25	3.5	52	3.7	79	3.8	105	4.7
26	3.4	53	3.7				

REFERENCES

- Archambeau, C.B. and J.B. Minster, *Elastodynamic representation theorems in prestressed elastic media with moving phase boundaries*, To be submitted to Geophysical J. Roy. Astr. Soc., 1974.
- Archambeau, C.B., *The theory of stress wave radiation from explosions in prestressed media*, Geophysical J. Roy. Astr. Soc., Vol. 29, 329-366, 1972.
- Cherry, J.T., T.C. Bache, C.B. Archambeau, and D.G. Harkrider, *A Deterministic Approach to the Prediction of Teleseismic Ground Motion from Nuclear Explosions*, Systems, Science and Software Report SSS-R-74-2034, Contract No. DNA 001-73-C-0167, January 1974.
- Cherry, J.T., C.B. Archambeau, G.A. Frazier, A.J. Good, K.G. Hamilton and D.G. Harkrider, *The Teleseismic Radiation Field from Explosions: Dependence of Seismic Amplitudes Upon Properties of Materials in the Source Region*, System, Science and Software Report SSS-R-72-1193, Contract No. DASA 01-71-C-0156, July 1972.
- Minster, J.B. and C.B. Archambeau, *Spectral and temporal characteristics of seismic wave radiation from tectonic sources*, To be submitted to Journal of Geophysical Research, 1974.
- Minster, J.B., *Elastodynamics of Failure in a Continuum*, Thesis, California Institute of Technology, December 1973.
- Anderson, D.L. and C.B. Archambeau, *The Anelasticity of the Earth*, Journal of Geophys. Research, Vol. 69, No. 10, 2071-2084, 1964.
- Archambeau, C.B., *General theory of elastodynamic source fields*, Rev. Geophys., Vol. 16, 241-288, 1968.
- Archambeau, C.B. and C. Sammis, *Seismic radiation from explosions in prestressed media and the measurement of tectonic stress in the earth*, Rev. Geophys., Vol. 8, 473-499, 1970.

REFERENCES (CONT'D)

- Archambeau, C.B., E.A. Flinn and D.G. Lambert, *Fine structure of the upper mantle*, J. Geophys. Res., Vol. 74, No. 25, 5825-5865, 1969.
- Archambeau, C.B. and E.A. Flinn, *Automated analysis of seismic radiation for source characteristics*, Proc. IEEE, Vol. 53, 1876-1884, 1965.
- Evernden, J.F., *Source Models for Earthquakes and Explosions with Associated Implications for Verification Network and Procedures*, ACDA Internal Report, 1973.
- Lambert, D.G., E.A. Flinn and C.B. Archambeau, *A comparative study of the elastic wave radiation from earthquakes and underground explosions*, Geophys. J. R. Astr. Soc., Vol. 29, 403-432, 1972.
- Tsai, Yi-Ben, *Utility of Tsai's Method for Seismic Discrimination*, Texas Instruments Incorporated, Semi-Annual Technical Report No. 2, Contract No. F44620-71-C-0112 AFOSR, July 1972.
- Hannon, W.J., *An examination of Rayleigh waves produced by shear and compressional line sources*, Lawrence Livermore Report, Prepared for U.S. Atmoic Energy Commission under contract No. W-7405-Eng-48, June 2, 1972.
- Futterman, W.I., *Dispersive body waves*, J. Geophys. Res., 67, pp. 5279-5291, 1962.
- Strick, E., *A predicted pedestal effect for pulse propagation in constant Q solids*, Geophysics, 35, pp. 387-403, 1970.
- Blake, F.G., *Spherical wave propagation in solid media*, J. Acoust. Soc. Amer., 24, 2, 1952.
- Helmburger, D.V. and D.G. Horkrider, *Seismic source descriptions of underground explosions and a depth discriminant*, Geophys. J.R. Astr. Soc., 31, pp. 45-66, 1972.